

AD-A064 776

NORTH CAROLINA STATE UNIV RALEIGH ENGINEERING DESIGN--ETC F/6 21/5
AN EXPERIMENTAL STUDY OF THE RESPONSE OF A TURBO-MACHINE ROTOR --ETC(U)
DEC 78 L HARDIN F44620-76-C-0055

UNCLASSIFIED

NCSU/EDC-78-6

AFOSR-TR-79-0073

NL

1 of 2
AD
A084778



AFOSR-TR. 79-0078

EDC-78-6

4
SR

LEVEL II

ENGINEERING
DESIGN
CENTER

ADA 064776

AN EXPERIMENTAL STUDY OF THE RESPONSE OF A
TURBOMACHINE ROTOR TO A LOW FREQUENCY INLET
DISTORTION

by

Larry Hardin

DDC
APPROVED
FEB 22 1979
RESOLVED
A

DDC FILE COPY

SCHOOL OF
ENGINEERING
NORTH CAROLINA
STATE UNIVERSITY
RALEIGH
NORTH CAROLINA

Report on AFOSR Contract F44620-76-C-0055
for a cooperative program between
United Technologies Research Center
and
North Carolina State University

AIR FORCE OFFICE OF SCIENTIFIC RESEARCH (AFSC)
NOTICE OF TRANSMITTAL TO DDC
This technical report has been reviewed and is
approved for public release IAW AFR 190-12 (7b).
Distribution is unlimited.
A. D. BLOSE
Technical Information Officer

Approved for public release;
distribution unlimited.

79 02 16 028

19 REPORT DOCUMENTATION PAGE		READ INSTRUCTIONS BEFORE COMPLETING FORM
1. REPORT NUMBER 18 AFOSR/TR-79-0073	2. GOVT ACCESSION NO.	3. RECIPIENT'S CATALOG NUMBER
4. TITLE (and Subtitle) AN EXPERIMENTAL STUDY OF THE RESPONSE OF A TURBO-MACHINE ROTOR TO A LOW FREQUENCY INLET DISTORTION	5. TYPE OF REPORT & PERIOD COVERED INTERIM Jan 76 - Dec 78	6. PERFORMING ORG. REPORT NUMBER 14 NCSU/EDC-78-61
7. AUTHOR(s) 10 LARRY HARDIN	8. CONTRACT OR GRANT NUMBER(s) 15 F44620-76-C-0055 AFOSR-75-2802	9. PROGRAM ELEMENT, PROJECT, TASK AREA & WORK UNIT NUMBERS 16 2307A4 17A4 61102F
9. PERFORMING ORGANIZATION NAME AND ADDRESS NORTH CAROLINA STATE UNIVERSITY SCHOOL OF ENGINEERING, ENGINEERING DESIGN CENTER RALEIGH, NORTH CAROLINA 27650	11. CONTROLLING OFFICE NAME AND ADDRESS AIR FORCE OFFICE OF SCIENTIFIC RESEARCH/NA BLDG 410 BOLLING AIR FORCE BASE, D C 20332	12. REPORT DATE 14 Dec 78
14. MONITORING AGENCY NAME & ADDRESS (if different from Controlling Office)	13. NUMBER OF PAGES 161 12 164p.	15. SECURITY CLASS. (of this report) UNCLASSIFIED
16. DISTRIBUTION STATEMENT (of this Report) Approved for public release; distribution unlimited. A		
17. DISTRIBUTION STATEMENT (of the abstract entered in Block 20, if different from Report)		
18. SUPPLEMENTARY NOTES		
19. KEY WORDS (Continue on reverse side if necessary and identify by block number) DYNAMIC STALL DISTORTED FLOW UNSTEADY FLOW UNSTEADY BOUNDARY LAYER TURBOCOMPRESSOR		
20. ABSTRACT (Continue on reverse side if necessary and identify by block number) As part of a joint technical effort involving North Carolina State University and United Technologies Research Center, an experiment was conducted to measure the response of an isolated turbomachine rotor to a distortion in inlet axial velocity. A once-per-revolution sinusoidal variation in axial velocity with an amplitude of approximately twenty percent of the average axial velocity was generated by an upstream screen. The response of the rotor was studied using pressure transducers and skin friction gages mounted on one of the rotor blades and a velocity probe at the rotor exit plane as well as with standard stationary frame pneumatic		

Instrumentation. The rotor was operated in undistorted flow to establish the quasi-steady behavior of the compression system. When the air inlet angle was reduced past a certain limit, the rotor began to experience rotating stall. When the rotor was operated in distorted flow, the pressures on the surface of the instrumented blade were observed to vary as a function of the instantaneous inlet angle. These variations were greatest at the leading edge of the airfoil and became smaller toward the trailing edge. This concentration of activity in the leading edge region is more pronounced than has been observed for isolated airfoils. As the instrumented blade traversed the distortion, it was observed to operate transiently at inlet angles below the quasi-steady stall point in an apparently unstalled condition. At these lower inlet angles, a separation bubble was found to exist on the leading edge of the blade. Velocity measurements made at the rotor exit plane in undistorted flow at moderate incidence angles indicated that the flow was essentially two-dimensional with no radial flow being measured except in the blade wake regions. This was not the case for similar incidence angles in distorted flow in which case significant radial flow components existed. The circumferential exit angle in distorted flow was found to lag the steady state exit angle. However, the variation of exit angle as a function of inlet angle in distorted flow did not have the same character as for undistorted flow. The observed differences are attributed partly to the three-dimensionality of the distorted flow field and partly to some measurement errors associated with the geometry of the probe. The peak pressure rise generated by the rotor was lower for distorted flow than for uniform inlet flow as should be expected. However, at high blade loading the pressure rise was less than the peak value for both undistorted and distorted flow, but was greater for distorted flow than for undistorted flow. It is believed that the ability of the blade to operate transiently beyond the steady state stall point is responsible for this behavior.

UNCLASSIFIED

AN EXPERIMENTAL STUDY OF THE RESPONSE OF A TURBOMACHINE
ROTOR TO A LOW FREQUENCY INLET DISTORTION

By

Larry Hardin

Report on AFOSR Contract F44620-76-C-0055 for a
cooperative program

between

United Technologies Research Center
East Hartford, Conn.

and

North Carolina State University
Raleigh, North Carolina

Engineering Design Center
School of Engineering
North Carolina State University
Raleigh, N. C. 27650

December, 1978

79 02 16 028

ACKNOWLEDGMENT

This work was supported in part by the Air Force Office of Scientific Research. Initial funding was under AFOSR Grant No. 75-2802 and subsequent funding was under Contract No. F44620-76-C-0055.

REVISION #		
DATE	BY	
REV	REV	
DESCRIPTION		
JUSTIFICATION		
BY _____		
CONTROLLER/AVAILABILITY CODE		
FORM	AVAIL. CODE	SERIAL
A		

ABSTRACT

As part of a joint technical effort involving North Carolina State University and United Technologies Research Center, an experiment was conducted to measure the response of an isolated turbomachine rotor to a distortion in inlet axial velocity. A once-per-revolution sinusoidal variation in axial velocity with an amplitude of approximately twenty percent of the average axial velocity was generated by an upstream screen. The response of the rotor was studied using pressure transducers and skin friction gages mounted on one of the rotor blades and a velocity probe at the rotor exit plane as well as with standard stationary frame pneumatic instrumentation.

The rotor was operated in undistorted flow to establish the quasi-steady behavior of the compression system. When the air inlet angle was reduced past a certain limit, the rotor began to experience rotating stall. When the rotor was operated in distorted flow, the pressures on the surface of the instrumented blade were observed to vary as a function of the instantaneous inlet angle. These variations were greatest at the leading edge of the airfoil and became smaller toward the trailing edge. This concentration of activity in the leading edge region is more pronounced than has been observed for isolated airfoils. As the instrumented blade traversed the distortion, it was observed to operate transiently at inlet angles below the quasi-steady stall point in an apparently unstalled condition. At these lower inlet angles, a separation bubble was found to exist on the leading edge of the blade.

Velocity measurements made at the rotor exit plane in undistorted flow at moderate incidence angles indicated that the flow was essentially two-dimensional with no radial flow being measured except in the blade wake regions. This was not the case for similar incidence angles in distorted flow in which case significant radial flow components existed. The circumferential exit angle in distorted flow was found to lag the steady state exit angle. However, the variation of exit angle as a function of inlet angle in distorted flow did not have the same character as for undistorted flow. The observed differences are attributed partly to the three-dimensionality of the distorted flow field and partly to some measurement errors associated with the geometry of the probe.

The peak pressure rise generated by the rotor was lower for distorted flow than for uniform inlet flow as should be expected. However, at high blade loading the pressure rise was less than the peak value for both undistorted and distorted flow, but was greater for distorted flow than for undistorted flow. It is believed that the ability of the blade to operate transiently beyond the steady state stall point is responsible for this behavior.

TABLE OF CONTENTS

	<u>Page</u>
LIST OF TABLES	v
LIST OF FIGURES	vii
LIST OF SYMBOLS	xi
INTRODUCTION	1
EXPERIMENTAL FACILITY	12
Large Scale Rotating Rig	12
Distortion Screens	16
Instrumentation System	18
Pneumatic Instrumentation	20
Unsteady Instrumentation	20
Power Supplies	24
Surface Pressure Measuring Systems	25
Skin Friction Gages	29
Rotating Frame Wake Probe	31
Data System	33
SCOPE OF EXPERIMENT	34
EXPERIMENTAL PROCEDURE	38
Data Acquisition	38
Overall Performance Parameters	40
Unsteady Blade Pressures	44
Transient Surface Flow Phenomena	48
Velocity Measurements at the Rotor Exit Plane	50
RESULTS	54
Overall Performance	54
Analysis of Unsteady Data	60
Blade Pressures	63
Normal Force and Pitching Moment Coefficients	79
Comparison to Cascade Data	84
Transient Surface Flow Phenomena	85
Unsteady Rotor Pressure Rise	92
Velocities and Flow Angles at the Rotor Exit Plane	95

TABLE OF CONTENTS (Cont'd)

	<u>Page</u>
CONCLUSIONS	105
APPENDICES	110
Appendix I. Power Supplies	110
Appendix II. Pressure Transducer Amplifiers	113
Appendix III. Constant Temperature Anemometers	116
Appendix IV. Instrumentation Used and Flow Conditions Run	120
Appendix V. Calculation of Exit Angle Using Momentum Theory	124
Appendix VI. Triaxial Probe Calibration	128
Appendix VII. Correction of Leading Edge Pressures	138
Appendix VIII. Computer Codes Used with Triaxial Hot-Film Probe	141
REFERENCES	146

LIST OF TABLES

	<u>Page</u>
I. Gaussian Positions and Weighting Factors	23
II. Harmonic Content of Differential Pressure, Normal Force and Pitching Moment Coefficients	66
III. First Harmonic Phase Angles of the Differential Pressures, Normal Force, and Pitching Moment	74
IV. Harmonic Content of Unsteady Rotor Pressure Rise Coefficient	94
V. Instrumentation Configuration for LSRR	121
VI. Summary of Flow Conditions Used in LSRR Inlet Distortion Experiment	123

LIST OF FIGURES

	<u>Page</u>
1. Possible Modes of Instability on Stall Line	3
2. Unsteady Rotor Response to 180° Square Wave Distortion	6
3. Typical Compressor Characteristic	9
4. UTRC Large Scale Rotating Rig	13
5. Modifications to LSRR to Permit Installation of Distortion Screens	15
6. Blade Geometry and Rotating Frame Nomenclature	17
7. Resistance Coefficient Distribution of Distortion Screen	19
8. Configuration of LSRR for Inlet Distortion Experiment	21
9. Pneumatic Blade Instrumentation	22
10. Rotating Instrumentation Configuration	26
11. Installation of Pressure Transducer in Blade	27
12. Typical Circuitry for Pressure Transducer Channels	28
13. Typical Circuitry for Skin Friction Gage Channels	30
14. Wake Probe Used in LSRR	31
15. Kulite Total Pressure Probe	32
16. Flow Regimes for Compressor Operation	34
17. Typical Pressure Transducer Data After each Stage of Processing	46
18. Sign Conventions for Normal Force and Pitching Moment Coefficients	47

LIST OF FIGURES (Cont'd)

	<u>Page</u>
19. Rotor Pressure Rise as a Function of Inlet Angle	55
20. Steady-State Loss Coefficient as a Function of Inlet Angle	57
21. Exit Angle as a Function of Inlet Angle	59
22. Generation of a Loop and the Possible Effects of Unsteadiness	61
23. Inlet Angles for Which Distorted Flow Data Are Presented	65
24. Pressure Coefficient as a Function of Inlet Angle	69
25. Pressure, Force, and Moment Phase Angle as a Function of Inlet Angle	75
26. Pressure Coefficient Distributions for Point 7.4	77
27. Pressure Coefficient Distributions for Point 7.9.	78
28. Pressure Coefficient Distributions for Point 7.15	80
29. Normal Force Coefficient as a Function of Inlet Angle	81
30. Pitching Moment Coefficient as a Function of Inlet Angle	83
31. Pressure and Skin Friction Time Histories for Point 7.4	87
32. Pressure and Skin Friction Time Histories for Point 7.9	90
33. Pressure and Skin Friction Time Histories for Point 7.15	91
34. Unsteady Rotor Pressure Rise as a Function of Inlet Angle	93

LIST OF FIGURES (Cont'd)

	<u>Page</u>
35. Velocity at Rotor Exit Plane as a Function of Gapwise Position in Undistorted Flow	96
36. Circumferential Flow Angle at Exit Plane as a Function of Gapwise Position in Undistorted Flow	98
37. Radial Flow Angle at Exit Plane as a Function of Gapwise Position in Undistorted Flow.	99
38. Velocity at Rotor Exit Plane as a Function of Gapwise Position in Distorted Flow	100
39. Circumferential Flow Angle at Rotor Exit Plane as a Function of Gapwise Position in Distorted Flow . .	101
40. Gap Averaged Circumferential Exit Angle as a Function of Inlet Angle	103
41. Radial Flow Angle at Rotor Exit Plane as a Function of Gapwise Position in Distorted Flow	104
42. Unregulated D.C. Power Supply	110
43. Schematic Diagram of \pm 15 Volt Regulator	111
44. Schematic Diagram of -10 Volt Regulator	112
45. Schematic Diagram of Pressure Transducer Amplifier . .	114
46. Schematic Diagram of Constant Temperature Anemometer	117
47. Control Volume for Momentum Theory Calculations	125
48. Axis Systems Used in Wake Probe Calibration	128
49. Sign Conventions for Pitch and Yaw Angles	130
50. Typical Results of Normal Velocity Calibration.	133
51. Pressure Coefficient Loops from Leading Edge Station Before Correction	139

LIST OF SYMBOLS

Each symbol is defined when it first appears in the text. Only those symbols which are used repeatedly are included in this list.

C_f	skin friction coefficient
C_m	pitching moment coefficient
C_N	normal force coefficient
C_P	blade pressure coefficient
C_{P_r}	rotor pressure rise coefficient (see Eq. (16))
C_x	axial velocity
C_{θ_1}	swirl velocity upstream of rotor in stationary frame
C_{θ_2}	swirl velocity downstream of rotor in stationary frame
E	anemometer bride voltage
E_0	anemometer calibration constant
k	anemometer calibration constant
N_{act}	actual rotational speed of rotor
P'_{O_1}	total pressure upstream of rotor in rotating reference frame
P'_{O_2}	total pressure downstream of rotor in rotating reference frame
P_{S_1}	static pressure upstream of rotor
P_{S_2}	static pressure downstream of rotor
q	effective cooling velocity
T_{O_1}	total temperature upstream of rotor
T_s	sensor temperature

LIST OF SYMBOLS (Cont'd)

T_{∞}	free stream static temperature
U	tangential wheel speed
u	velocity in sensor co-ordinates for triaxial probe calibration
V	fluid velocity
v	velocity in rotor co-ordinates for triaxial probe calibration
W_1	relative velocity upstream of rotor (see Fig. 6)
W_2	relative velocity downstream of rotor (see Fig. 6)
x/c	chordwise position on blade expressed as a fraction of the chord
y/g	gapwise position in rotor wake expressed as a fraction of the blade gap
α_{mc1}	incidence angle (see Fig. 6)
β_1	inlet angle (see Fig. 6)
β_1^*	stagger angle (see Fig. 6)
β_2	exit angle (see Fig. 6)
ΔC_p	differential pressure coefficient (see Eq. 32)
ρ	fluid density
ψ	radial flow angle
τ_w	wall shearing stress
X_{ss}	steady-state total pressure loss coefficient

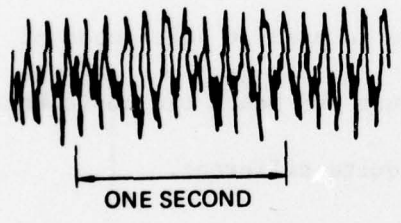
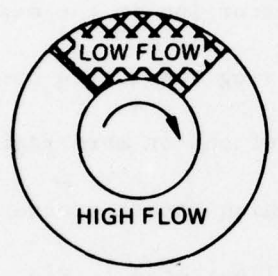
INTRODUCTION

An aircraft propulsion system must be capable of operating smoothly and efficiently in all parts of the aircraft's flight envelope. This means that at some point every engine will be forced to operate with non-uniform inlet flow. For example, military aircraft which are sometimes required to execute violent maneuvers may experience inlet distortion generated by the aircraft attitude. Weapon firing is another source of distortion peculiar to military aircraft. One source of distortion which is common to all aircraft is ground operation or takeoff in a crosswind or in gusts. The result of operation with non-uniform inlet flow may be a simple loss of performance or, in extreme cases, the triggering of compressor stall. Since any loss of thrust under the previously described circumstances may have serious consequences, the engine designer is faced with the task of creating a compression system which is insensitive to inlet distortions. That is, the loss in pressure rise associated with distortion must be small and the tendency of the compressor to stall under the influence of distortion must be minimized. Furthermore, the operating conditions at which some type of compressor stall might be expected to occur must be known so that they may be avoided. Finally, in the event that the compressor does become stalled, it must be possible to recover from stall with a minimum of effort and as quickly as possible.

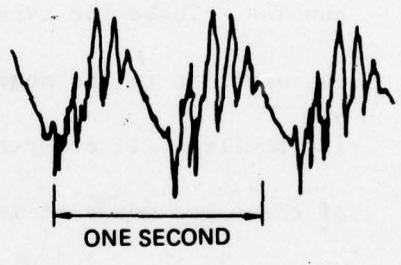
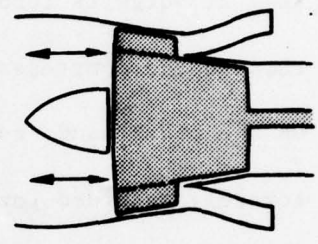
In order to better understand the inlet distortion problem, a more detailed discussion of compressor stall is in order. Compressor instabilities appear in two distinct forms known as surge and rotating stall (Ref. 1). These two phenomena are described in detail in Ref. 2. The description of surge and rotating stall as presented in the subsequent paragraphs is essentially a summary of that presented in Ref. 2. Surge is fundamentally a timewise excursion in the mass flow through the compressor simultaneously involving the entire compressor. On the other hand, rotating stall consists of one or more regions of severely retarded (or even reversed) flow which rotate around the annulus. These two types of behavior are illustrated in Fig. 1. It is important to the designer to be able to predict which mode of instability will occur because the nature and hence the consequences of these two modes of instability are quite different.

It has been stated that surge is a timewise excursion in the mean mass flow through a compressor. As such, it is a relatively low frequency phenomenon (frequencies of one or two cycles per second are typical) which involves large excursions in the annulus-averaged mass flow. In fact, the conditions may be such that rotating stall occurs during part of each surge cycle. Surge can lead to excessive inlet overpressures resulting in damage to engine components. Since the excursions in mass flow during surge are large, it is very possible that the compressor will operate in conditions normally associated

ROTATING STALL
CIRCUMFERENTIALLY NONUNIFORM FLOW



SURGE
AXIALLY OSCILLATING FLOW



INLET HOT WIRE OUTPUT

FIG. 1 POSSIBLE MODES OF INSTABILITY ON STALL LINE

with unstalled flow over part of the surge cycle. Recovery from surge might be possible by changing the throttle setting or opening internal bleeds.

In contrast, the unsteadiness associated with rotating stall is more localized. Once a rotating stall system becomes stable, the annulus-averaged mass flow is constant with time. One or more regions of severely retarded flow develop and rotate around the annulus. They may extend over the entire span of the blading or cover only part of the blades (for example, only the hub region might be involved). The circumferential extent also varies from a few blade gaps to perhaps half of the annulus. The frequency of the rotating stall phenomenon is typically an order of magnitude greater than that for surge. A rotational speed of approximately half the rotor speed is common. The variations in instantaneous inlet angle (and hence blade loading) as the stall cell or cells propagate around the rotor can be quite severe. Prolonged operation in rotating stall may thus lead to fatigue failure in the compressor blading. Recovery from rotating stall can be much more difficult than recovery from surge because the compressor does not operate in conditions normally associated with unstalled flow at any time during the occurrence of rotating stall.

As a background for the present experimental effort, the performance of a rotor in distorted, but unstalled, flow will first be

considered. In particular, a circumferential distortion in the inlet axial velocity will be discussed, because this type of distortion has been found to have more pronounced effects on rotor performance. This topic has been extensively investigated both experimentally and analytically by a number of authors. A good sampling of various approaches that have been used may be found in Ref. 3. References 4 and 5 provide a further bibliography of background material. The analytical investigation of the performance of a rotor undergoing distortion must account for the fact that, although the distortion field is steady, the blades themselves are subjected to an unsteady flow as they traverse this distortion. Their behavior may therefore depart considerably from their undistorted performance characteristics, especially when the blades are heavily loaded. As an example of this phenomenon, the unsteady total pressure loss of a compressor operating in distorted flow is shown in Fig. 2 (taken from Ref. 6). This curve also points out another important aspect of the unsteady flow field in that the rotor is seen to operate transiently in an apparently unstalled condition at inlet angles which would normally result in stall for undistorted inlet flow.

Many methods have been used to model the blade rows of a turbomachine and to include unsteady effects. Adamczyk (Ref. 7) modelled the blade row as an actuator disk for which the exit flow angle and the total pressure loss across the row were given as functions of the inlet

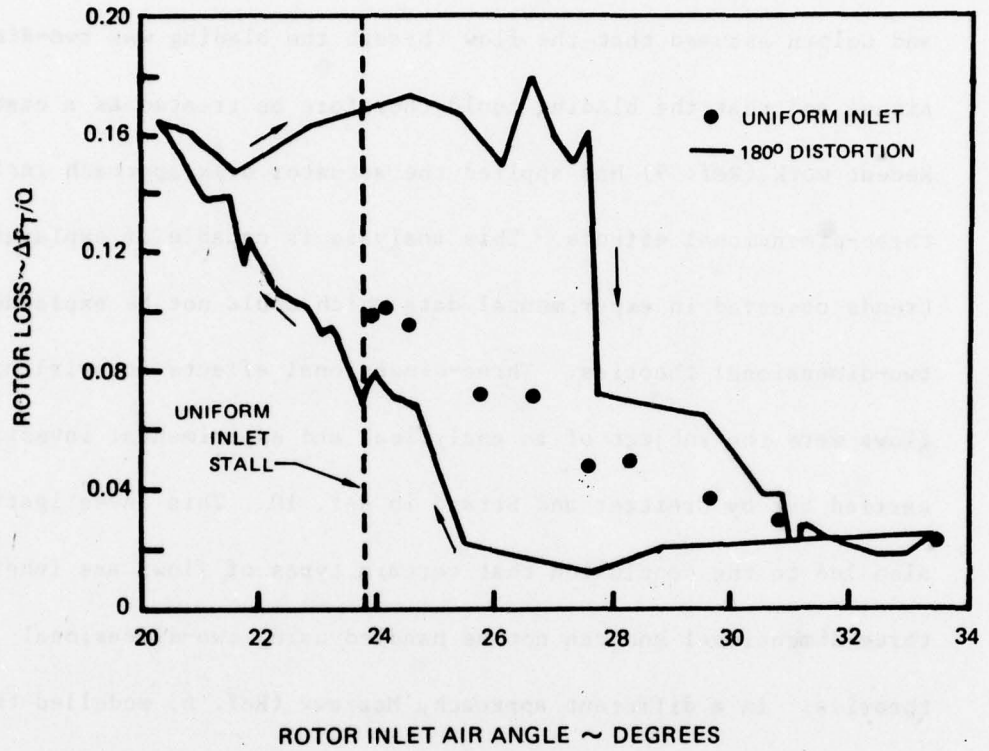


FIG. 2 UNSTEADY ROTOR RESPONSE TO 180° SQUARE WAVE DISTORTION

angle for steady flow. The unsteady effects were modelled as simple time lags applied to the steady characteristics. Colpin (Ref. 8) extends this type of analysis to compressible flow. Both Adamczyk and Colpin assumed that the flow through the blading was two-dimensional and that the blading could therefore be treated as a cascade. Recent work (Ref. 9) has applied the actuator disk approach including three-dimensional effects. This analysis is capable of explaining trends observed in experimental data which could not be explained by two-dimensional theories. Three-dimensional effects in swirling flows were the subject of an analytical and experimental investigation carried out by Greitzer and Strand in Ref. 10. This investigation also led to the conclusion that certain types of flows are inherently three-dimensional and can not be handled using two-dimensional theories. In a different approach, Mazzawy (Ref. 6) modelled the compressor undergoing distortion as several compressors in parallel with different inlet conditions but a common outlet condition. These few papers are fairly representative of the analytical work being done in this field. To check the validity of the analyses and, in some cases, to provide input data, it is necessary to have a body of experimental data representative of the conditions being modelled.

Some authors have conducted purely experimental studies of the response of turbomachine blading to inlet distortion. Bruce and Henderson (Ref. 11) have used a force balance to measure the unsteady

lift and moment on a blade in an isolated rotor for sinusoidal distortions in inlet axial velocity. The unsteady pressures on the surface of a blade were measured by Peacock (Ref. 12) using an array of miniature pressure transducers. These measurements were carried out in a low hub-to-tip ratio compressor with square-wave and some sine wave type distortions. A different approach was taken by Molkelke (Ref. 13) who attempted to derive the unsteady blade lift from measurements of absolute flow quantities. He investigated the response of the blading to square wave distortions and to forward and backward ramp type distortions. The results for the ramp distortions were found to differ depending on which way the total pressure defect was penetrated. The unsteady pressure response of cascaded blades to gusts was examined by Satyanarayana (Ref. 14) in a tunnel where the blades remained stationary while the tunnel's ceiling and floor were moved. The resulting gusts were primarily non-convecting whereas the inlet distortion problem is essentially a convected gust problem. The experimental apparatus also restricted the investigation to very low reduced frequencies. Kool, De Ruyck, and Hirsch (Ref. 15) have made measurements of the wake profiles downstream of a compressor rotor in undistorted flow and Colpin and Kool (Ref. 16) have made similar measurements under the effects of a triangular distortion pattern. It was noted that the wake shapes and the exit flow angles were strongly influenced by the presence of the distortion.

Some of the work which has been done on compressor instabilities will now be considered. As was previously mentioned, these instabilities might appear as surge or rotating stall. The first quantitative measure of when a given mode will occur was presented by Greitzer (Ref. 2). The theoretical derivation which leads to this prediction, however, requires the compressor performance curve (Fig. 3) as an

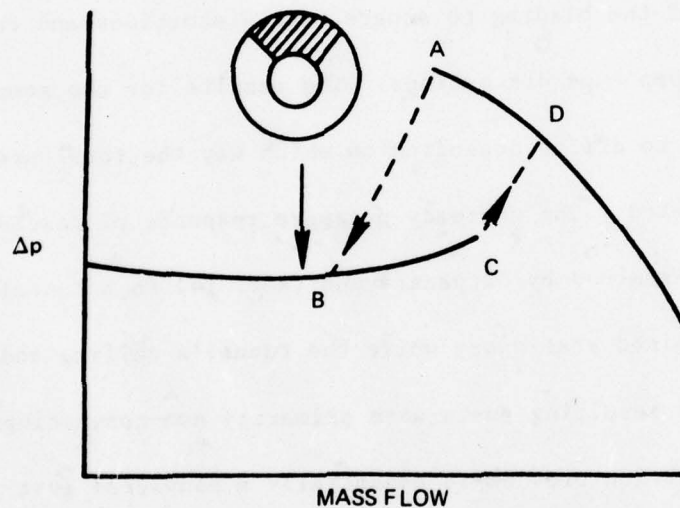


FIG. 3 TYPICAL COMPRESSOR CHARACTERISTIC

input. Note that there are basically two branches in the typical curve shown. These correspond to unstalled and stalled operation, respectively. There is a range of inlet conditions where either stalled or unstalled operation is possible with a large hysteresis

loop apparent between stall onset (point A to point B) and stall recovery (point C to point D). Since both surge and rotating stall are strongly dependent on the shape of the curve in the vicinity of this hysteresis loop, it is important to know the overall features of the performance curve for both stalled and unstalled flow including the hysteresis aspect. A method which is able to predict the basic features of these hysteresis loops based on the compressor design parameters is described in Ref. 17. At present, the method involves a great deal of empiricism. There is still much additional work to be done.

The rotating stall problem has also been the subject of some study. The flow in a compressor undergoing rotating stall is unsteady even in the stationary reference frame. Thus, the pneumatic instrumentation commonly used to measure the time-averaged pressures in steady flows is not generally applicable. As pointed out by Bennett (Ref. 18), the use of these averaged pressures may lead to significant errors in velocity and flow angle measurements if there are large variations in the pressures and velocities in question. The difficulties involved are greatest in dealing with on-blade measurements made in a non-uniform flow field. Without unsteady instrumentation, one can only obtain average pressures (and hence normal force and pitching moment) at an average inlet angle. This type of data does not adequately describe the aerodynamic response of the blade to the

distortion. Pneumatic instrumentation can be used to measure performance parameters in the stationary reference frame and can be quite useful when used in conjunction with high response instrumentation (c.f. the experimental work reported in Ref. 2). Sexton, O'Brien and Moses (Ref. 19) have developed a telemetry system and have used it in conjunction with miniature pressure transducers to make on-rotor studies of rotating stall. This system is necessarily channel limited and has a restricted bandwidth.

It is obvious that further extension of the analytical efforts previously described requires the availability of good experimental data both as an input to the theories and as a check on their accuracy. Therefore, North Carolina State University (NCSU) and United Technologies Research Center (UTRC) have embarked on a joint project under the sponsorship of the Air Force Office of Scientific Research (AFOSR) to study analytically and experimentally the response of a compressor stage to an inlet distortion. The work reported herein is the first of several planned experimental investigations of this phenomenon using UTRC's Large Scale Rotating Rig (LSRR).

EXPERIMENTAL FACILITY

Large Scale Rotating Rig

This experiment was conducted in the Large Scale Rotating Rig (LSRR) located at United Technologies Research Center (UTRC) in East Hartford, Connecticut. The LSRR was originally designed to provide a facility which would be of sufficient size to permit resolution of endwall flows, possess a high degree of flexibility in regard to the configurations which can be tested, and enable measurements to be made directly in the rotating reference frame.

Overall arrangement of the facility is shown in Fig. 4. Flow enters the rig through a twelve foot diameter inlet. A six inch thick section of honeycomb material is mounted at the inlet face to remove any crossflow effects. The inlet contracts smoothly down to a cross section five feet in diameter with the flow then passing through a series of fine mesh screens. Immediately downstream of the screens is a telescoping section which slides axially to permit access to the test section. The test section is five feet in diameter with large segments of the outer casing constructed of Plexiglas to facilitate flow visualization, holography, or laser-velocimeter studies. Axial length of the test section (excluding the hub spinner length) is three feet. The rotor is mounted to a shaft cantilevered from two downstream bearings thus providing a clean flow path to the most upstream blade row. A hydraulic motor capable of turning the

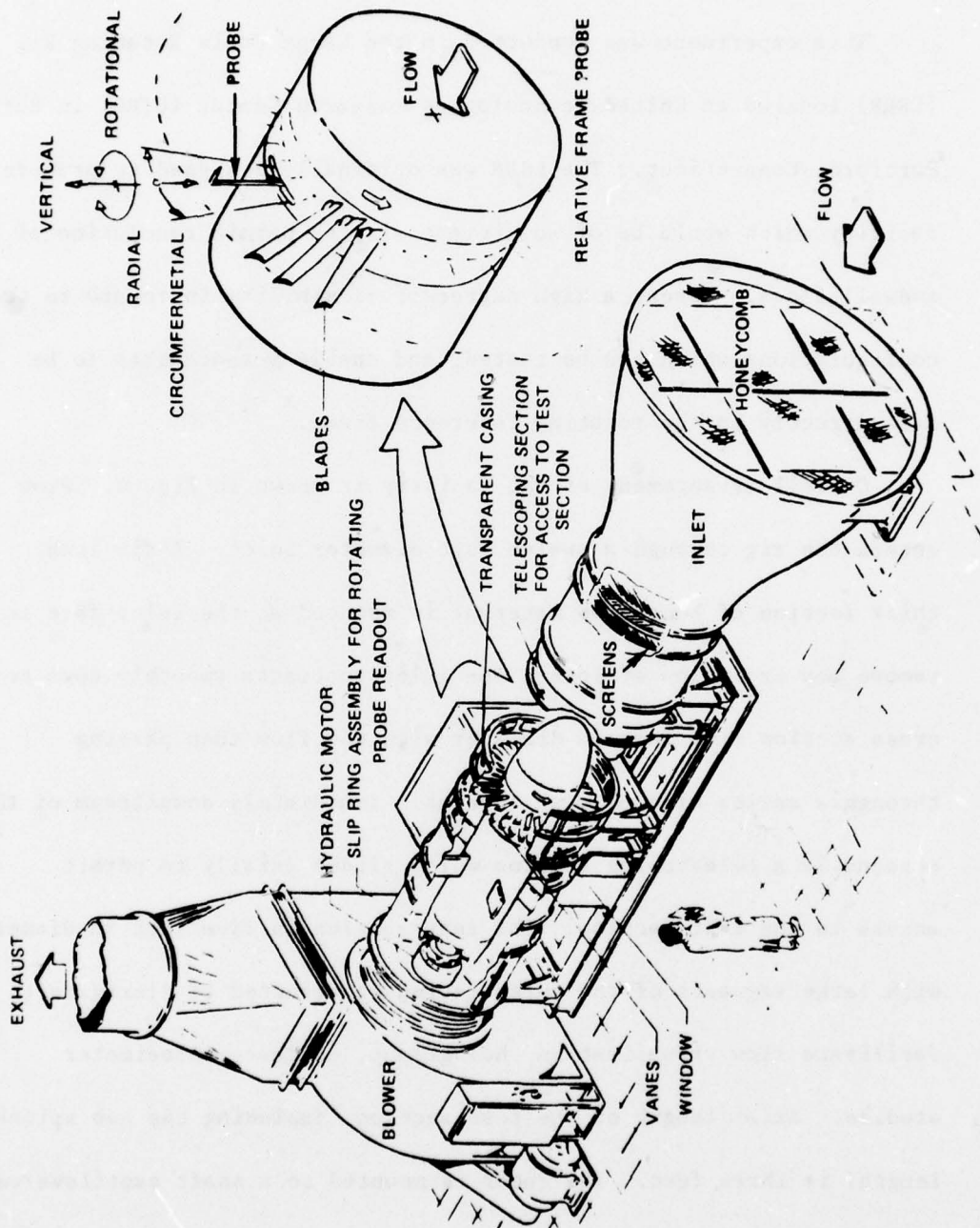


FIG. 4 UTRC LARGE SCALE ROTATING RIG

shaft at 800 rpm drives the rotor. Downstream of the test section, flow passes through an annular diffuser into a centrifugal fan and is subsequently exhausted from the rig. A vortex valve mounted at the fan inlet controls the flow rate.

The configuration tested in this experiment was an isolated rotor with a hub-to-tip ratio of 0.8. The rig had previously been used only with models which involved a stationary set of inlet guide vanes upstream of the rotor and these vanes had been used to support the hub spinner which was also stationary. Furthermore, no provision existed for mounting a distortion generating screen. The modifications to the rig necessary to support the hub spinner without the inlet guide vanes and to provide a place for mounting the distortion screen are shown in Fig. 5. A large bearing was added on the front of the rotor shaft to support the rear of the hub spinner. A spacer ring was installed between two segments of the hub spinner so the forward junction coincided with the joint in the outer casing between the test section and the telescoping section upstream. The distortion screen was installed at this location to support the front of the spinner and restrain it from rotating. When the rig was run without distortion, a screen frame (without any wire screening installed) was used in place of the distortion screen to perform this support function.

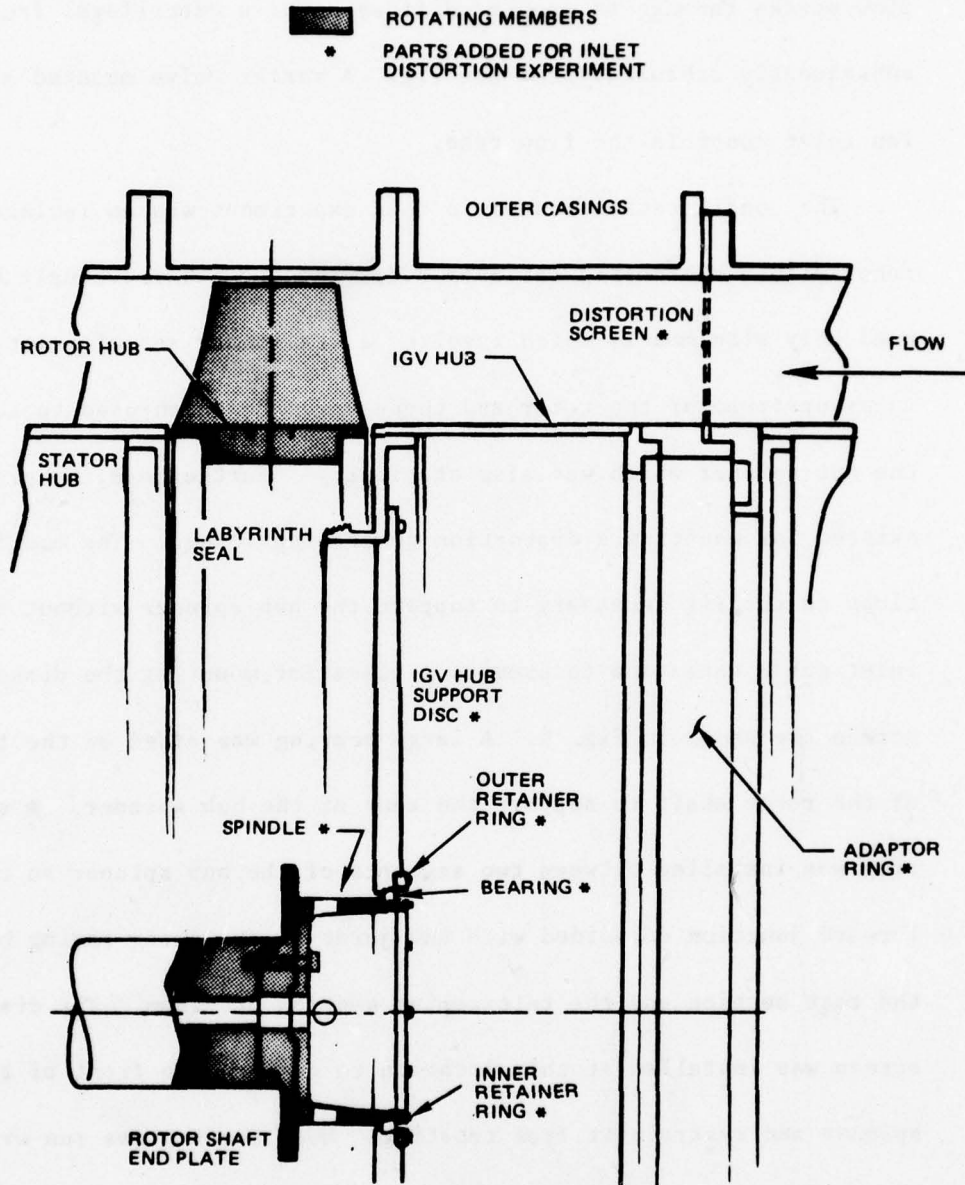


FIG. 5 MODIFICATIONS TO LSRR TO PERMIT INSTALLATION OF DISTORTION SCREENS

The rotor had 28 blades with a span and chord of 0.5 feet. Each blade consisted of an eight percent NACA 65-series thickness distribution superimposed on a 50-degree circular-arc mean camber line. The blades were installed with a midspan stagger angle, β_1^* , of 30 degrees. The gap-to-chord ratio at midspan was 1.01. The blade cross section at midspan and the relative frame velocity and flow angle nomenclature are shown in Fig. 6.

The LSRR was operated at a constant corrected wheel speed of 600 rpm throughout the experiment. The mean inlet angle was varied by changing the flow rate with the downstream vortex valve. The circumferentially averaged axial velocity in the test section was varied between 75 ft/sec and 170 ft/sec, resulting in a blade Reynolds number of approximately 0.5×10^6 . This value is comparable to that found in an actual turbomachine. Therefore, although the flow is admittedly incompressible, both the blade geometry and the Reynolds number are representative of the blading in the high compressors of current engines.

Distortion Screens

The inlet distortion imposed on the rotor in this experiment was a nominal 20-percent, once-per-revolution, sinusoidal variation in the inlet axial velocity. This distortion was generated by a screen consisting of segments of wire screening of various meshes attached to a support frame. The design of the distortion screen follows the

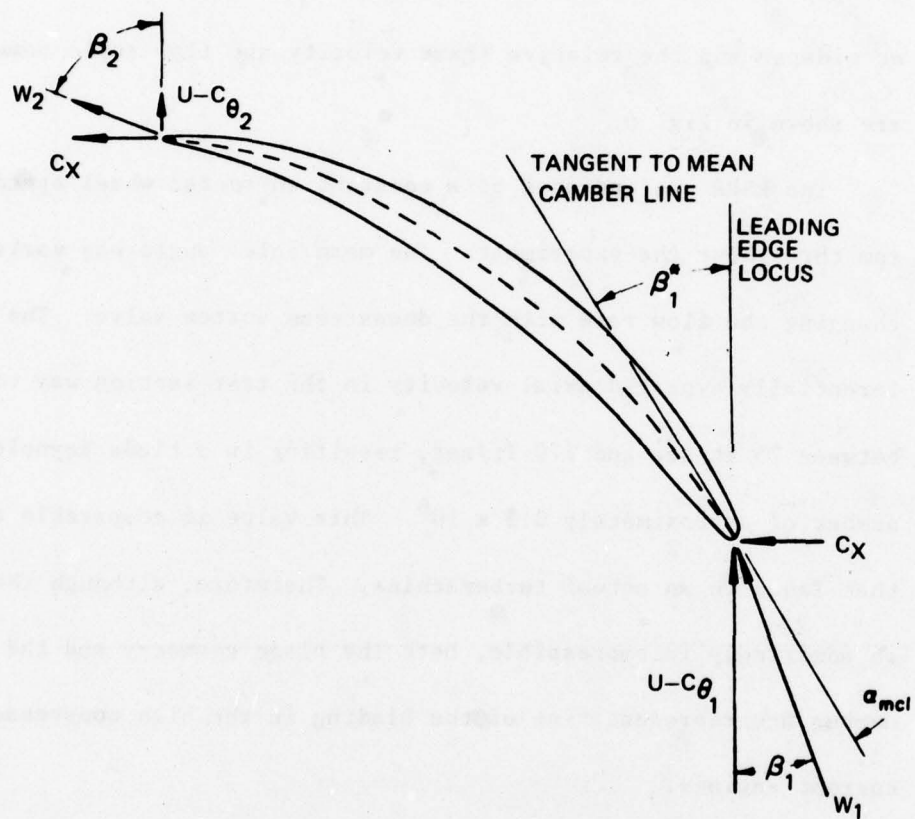


FIG. 6 BLADE GEOMETRY AND ROTATING FRAME NOMECLATURE.

work of Bruce (Ref. 20). Using the equations presented in Ref. 20, a resistance coefficient distribution for the screen was calculated which would give the desired distortion. Various meshes of wire screening were chosen so that twelve different values of resistance coefficient could be obtained using one or more of the meshes. The desired distribution and that actually obtained are shown in Fig. 7.

Instrumentation System

One of the most important aspects of any experimental program is the instrumentation system. It must provide accurate measurements with a minimum of attention. Part of the instrumentation used in this experiment was mounted inside the rotor hub of the LSRR and rotated with the rotor, thus imposing additional constraints on size and durability. Furthermore, the limited number of slip rings available to interface the rotating equipment with the stationary equipment was a key factor in many of the decisions made during the design phase. The system described below was the result of considerable experimentation. While no single component was totally new, the manner in which the various pieces of equipment were combined was unique and effective. Some of the techniques originally developed for the inlet distortion experiment have found application in other experimental programs at UTRC.

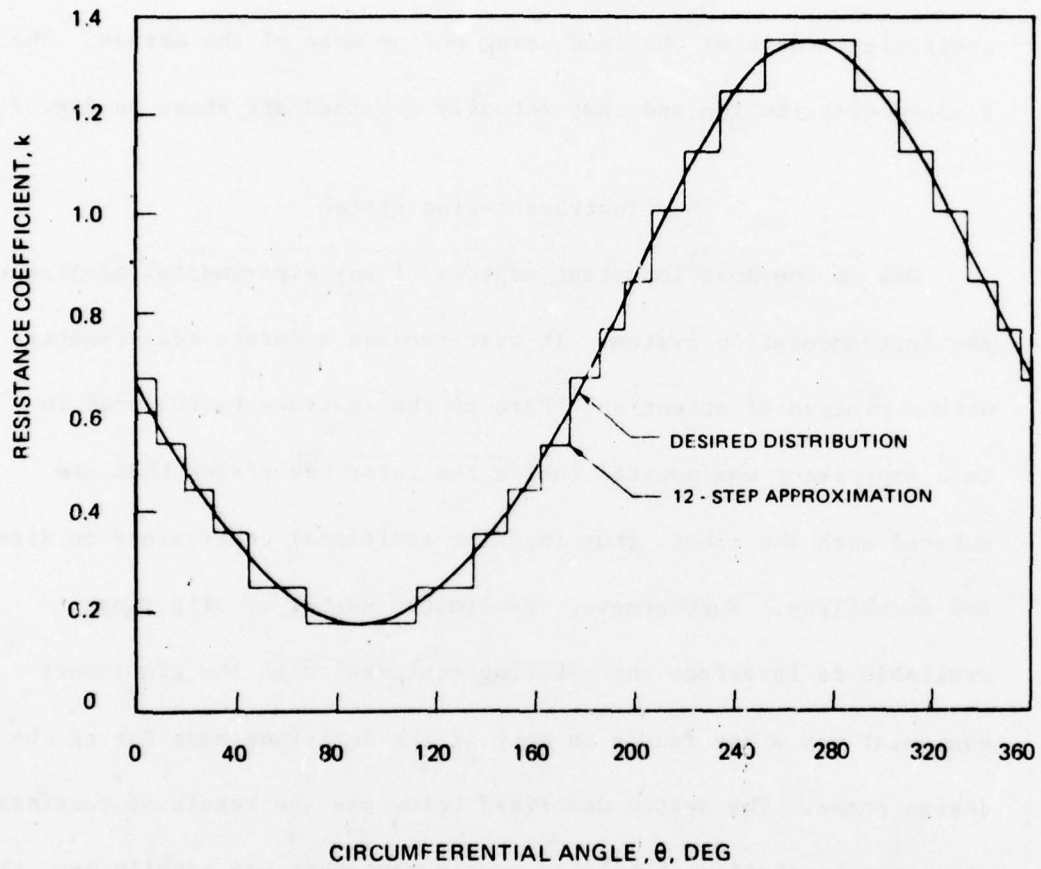
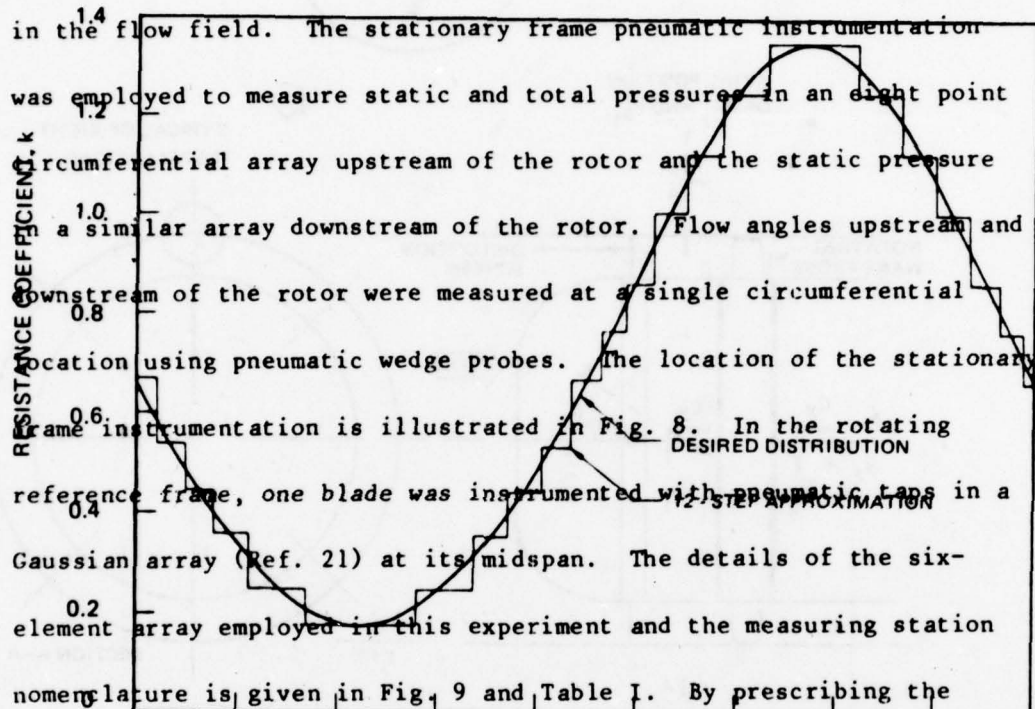


FIG. 7 RESISTANCE COEFFICIENT DISTRIBUTION OF DISTORTION SCREEN

Pneumatic Instrumentation

Normal instrumentation for the LSRR consists of stationary and rotating reference frame pneumatic probes and taps connected to scani-valves to measure the time averaged pressures at various points in the flow field. The stationary frame pneumatic instrumentation



was employed to measure static and total pressures in an eight point circumferential array upstream of the rotor and the static pressure at a similar array downstream of the rotor. Flow angles upstream and downstream of the rotor were measured at a single circumferential location using pneumatic wedge probes. The location of the stationary frame instrumentation is illustrated in Fig. 8. In the rotating reference frame, one blade was instrumented with pneumatic taps in a Gaussian array (Ref. 21) at its midspan. The details of the six-element array employed in this experiment and the measuring station nomenclature is given in Fig. 9 and Table I. By prescribing the

FIG. 8. RESISTANCE COEFFICIENT DISTRIBUTION OF DISTORTION SCREEN

Unsteady Instrumentation

To measure the fluid dynamic response of the rotor to the inlet distortion, it was necessary to provide high response instrumentation

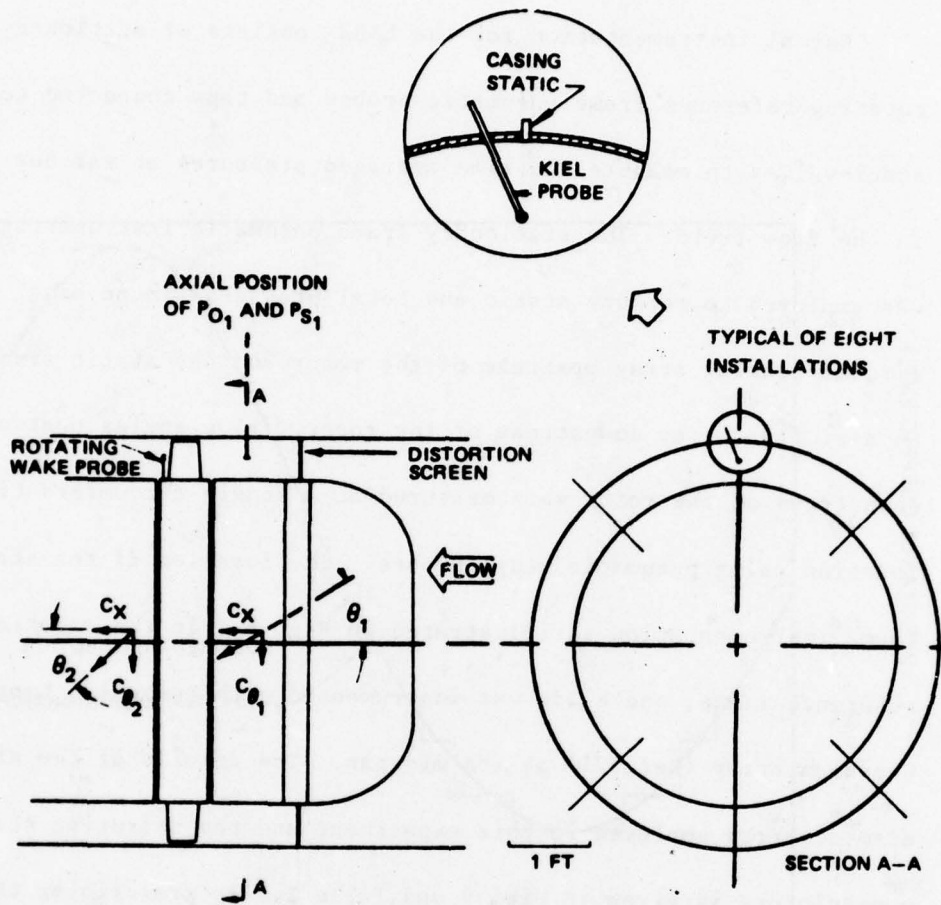


FIG. 8 CONFIGURATION OF LSRR FOR INLET DISTORTION EXPERIMENT

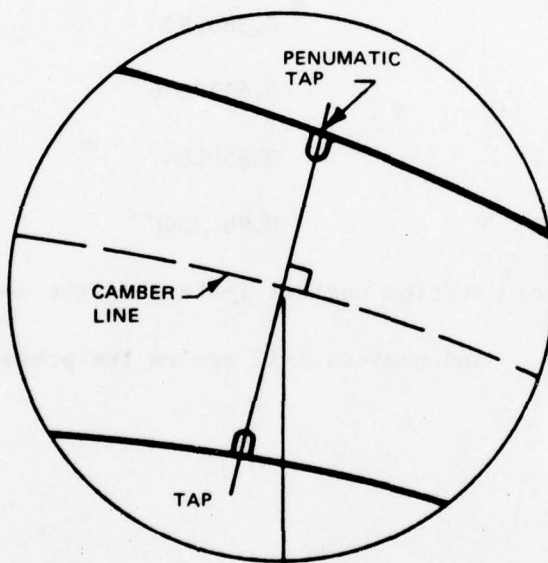
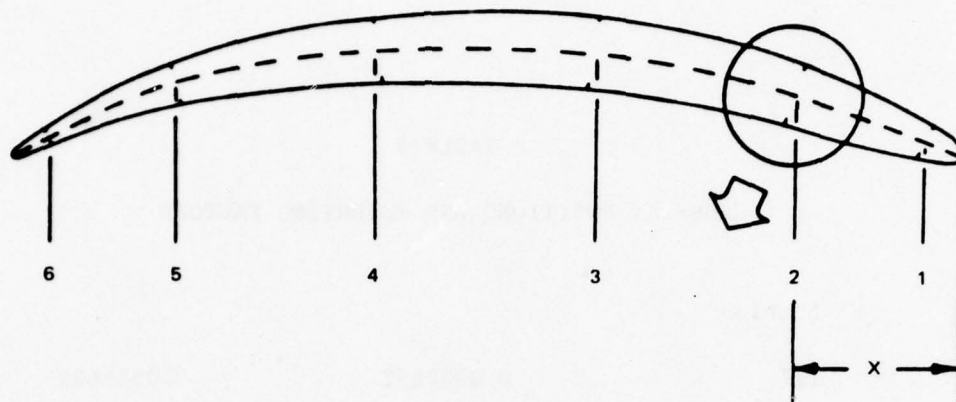


FIG. 9 PNEUMATIC BLADE INSTRUMENTATION

TABLE I
GAUSSIAN POSITIONS AND WEIGHTING FACTORS

Station		
1,7	0.0337652	0.0856622
2,8	0.1693953	0.1803808
3,9	0.3806904	0.2339570
4,10	0.6193096	0.2339570
5,11	0.8306047	0.1803808
6,12	0.9662348	0.0856622

Note: Station numbers 1-6 are on the suction surface
and numbers 7-12 are on the pressure surface.

in the rotating reference frame. Since no such instrumentation existed, it was necessary to design a package which could make the desired measurements. Parameters of interest were:

1. Rotor blade surface pressures
2. Rotor blade transient surface flow phenomena
3. Pressures and velocities in the near wake of the rotor.

The rotating frame instrumentation in the LSRR was interfaced to the stationary frame through a slip ring package. A system was evolved which maximized the number of channels of information which could be obtained with the limited number of slip rings available and simultaneously minimized the noise contamination problems commonly experienced with slip rings. The basic idea was to place all the signal conditioning and amplifying equipment necessary to produce a high level, single ended signal inside the rotor hub. After a limited number of slip rings were dedicated to supplying power and a common output reference, only one slip ring was needed to transmit each channel of data. Furthermore, by keeping the current through the slip rings which transmit the data to a minimum, it was possible to virtually eliminate the electrical noise normally generated by the varying contact resistance which is inherent in the slip rings.

Power Supplies

An unregulated direct current power supply located in the stationary frame produced positive and negative outputs of twenty

volts with respect to a common ground with a current capability of three amperes. The power was brought onto the rotating frame through the slip rings where it was regulated to produce the necessary voltages for driving the various pieces of equipment. As shown in Fig. 10, three regulators which produce plus and minus fifteen volts were used to power the constant temperature anemometers and pressure transducer amplifiers. A separate ten volt regulator provided excitation to the pressure transducers themselves. Schematics for the regulators are presented in Appendix I.

Surface Pressure Measuring Systems

Unsteady pressures on the surface of one of the rotor blades were measured using miniature pressure transducers. The units used in this experiment were Kulite LQ-64-125 \pm 5D transducers which have an exceptionally high sensitivity at the expense of a slightly higher than normal drift rate. The installation of a typical transducer is shown in Fig. 11. The transducers which measure the pressures on the suction surface of the blade were inserted from the pressure surface, and vice versa. The transducers were installed with Duco cement and pressure sealed with model airplane dope. The depressions in which the transducers rest were filled with a mixture of model airplane dope and talcum powder almost to the surface of the airfoil. When this compound had cured sufficiently, a layer of epoxy putty was applied and sanded to the airfoil contour. This process resulted in

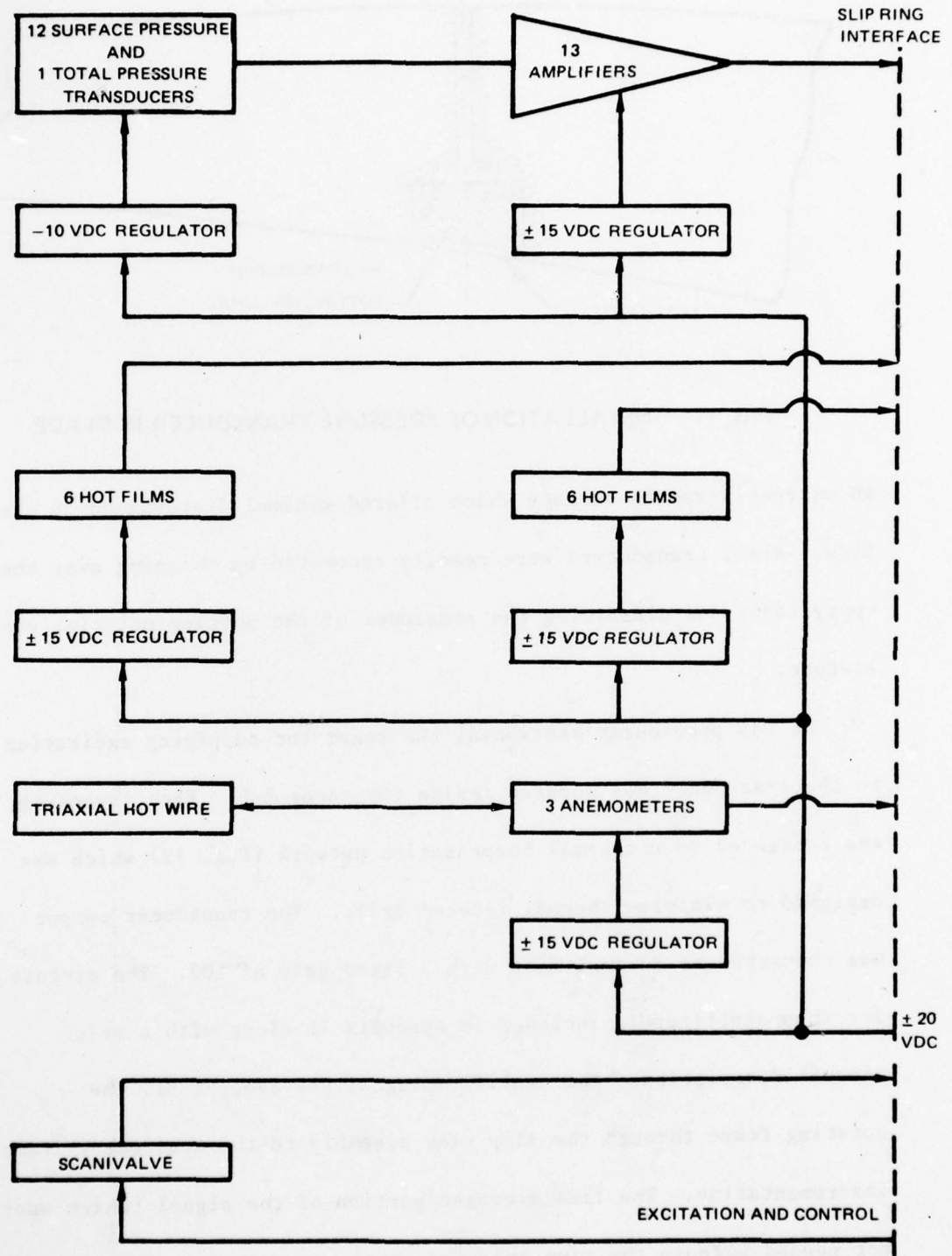


FIG. 10 ROTATING INSTRUMENTATION CONFIGURATION

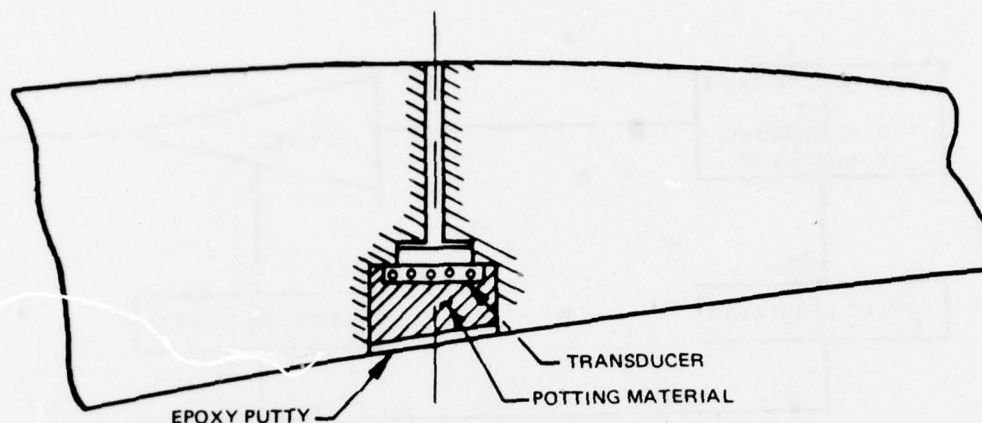


FIG. 11 INSTALLATION OF PRESSURE TRANSDUCER IN BLADE

an extremely smooth surface which offered minimal disturbance to the flow. Also, transducers were readily recovered by chipping away the epoxy layer and dissolving the remainder of the potting material with acetone.

As was previously mentioned, the regulator supplying excitation to the transducer was mounted inside the rotor hub. Each transducer was connected to a thermal compensation network (Fig. 12) which was designed to minimize thermal induced drift. The transducer output was connected to an amplifier with a fixed gain of 100. The circuit for this amplifier is included in Appendix II along with a brief circuit description. The amplified signal was brought off the rotating frame through the slip ring assembly to the stationary frame instrumentation. The time averaged portion of the signal (which was not needed because the time averaged pressures were measured with pneumatic instrumentation) were removed by passing the signal through

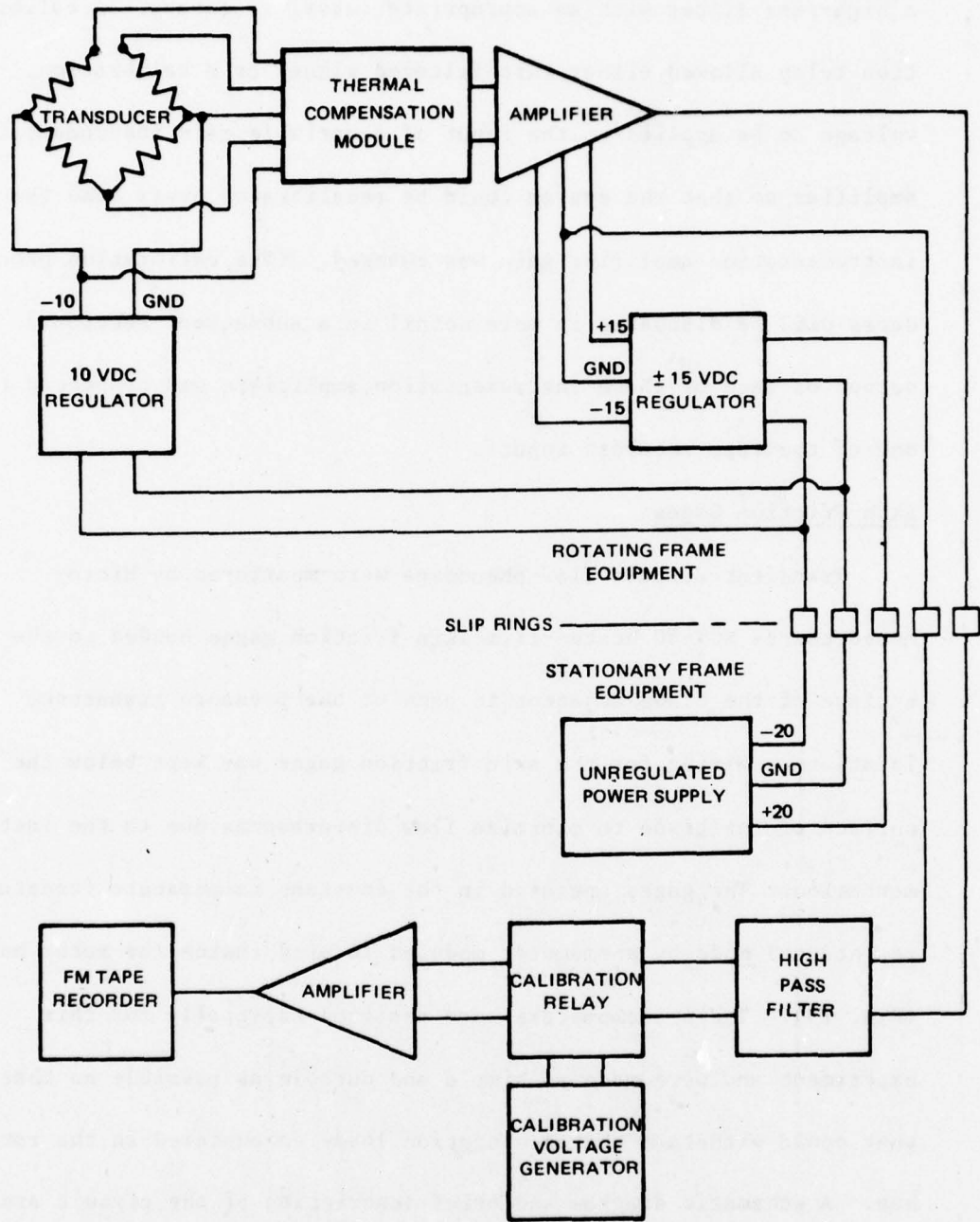


FIG. 12 TYPICAL CIRCUITRY FOR PRESSURE TRANSDUCER CHANNELS

a high-pass filter with an appropriate cutoff frequency. A calibration relay allowed either this filtered signal or a calibration voltage to be applied to the input of a variable gain instrumentation amplifier so that the system could be recalibrated every time the instrumentation amplifier gain was changed. (The calibration procedures will be discussed in more detail in a subsequent section.) The output of each of these instrumentation amplifiers was connected to one of the tape recorder inputs.

Skin Friction Gages

Transient surface flow phenomena were monitored by Micro-Measurements EGT-50 heated-film skin friction gages bonded to the surface of the blade adjacent to each of the pressure transducer locations. Wiring for the skin friction gages was kept below the surface of the blade to minimize flow disturbances due to the instrumentation. The gages operated in the constant temperature (constant resistance) mode by anemometer modules located inside the rotor hub (Fig. 13). These anemometers were designed especially for this experiment and were made as simple and durable as possible so that they could withstand the acceleration loads encountered in the rotor hub. A schematic diagram and brief description of the circuit are included in Appendix III. The output of an anemometer module was relatively high in amplitude and needed no further amplification. After the signal had passed through the slip rings, the time averaged

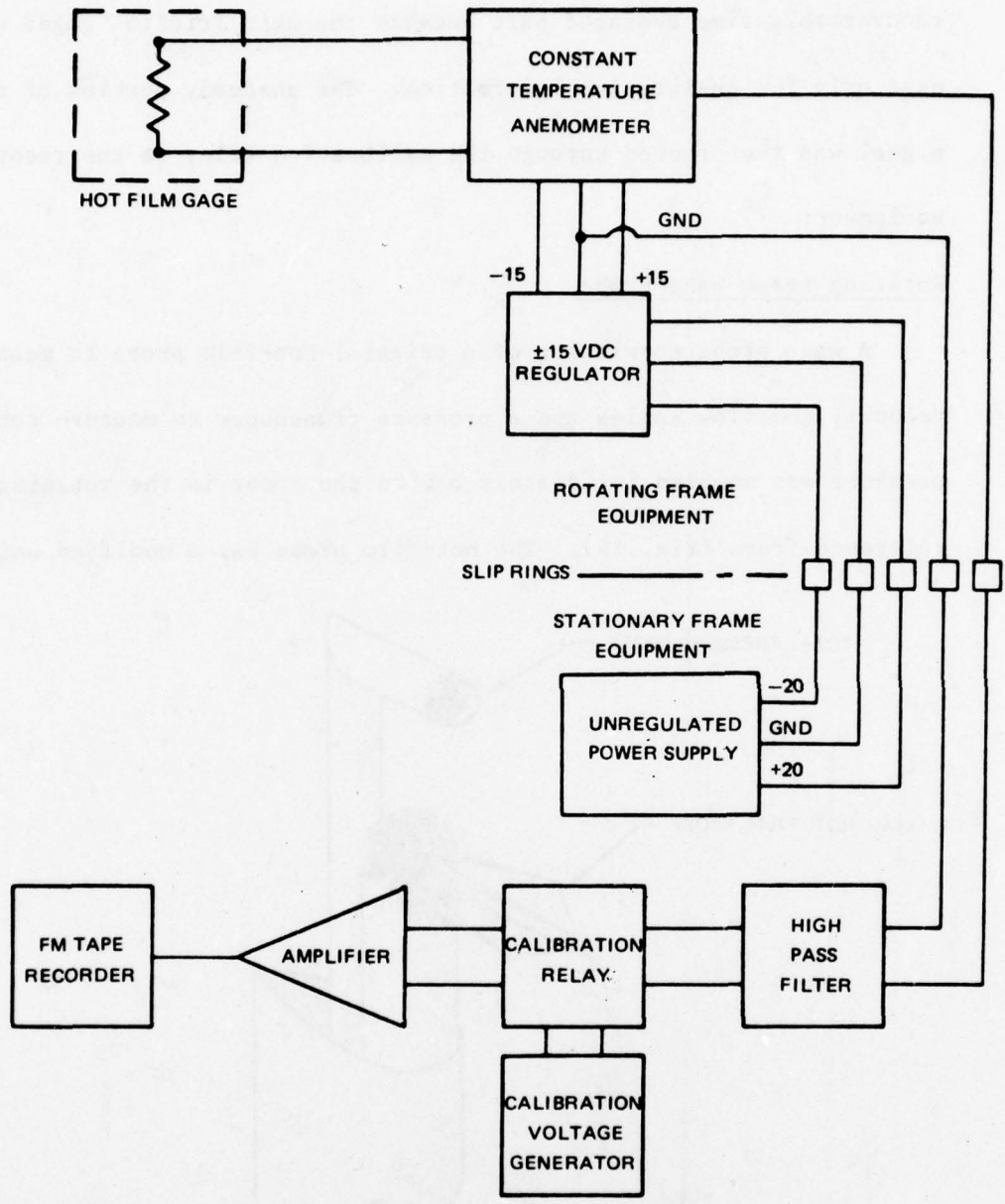


FIG. 13 TYPICAL CIRCUITRY FOR SKIN FRICTION GAGE CHANNELS

component was removed by a low pass filter. No attempt was made to recover this time averaged part because the skin friction gages were used only for qualitative information. The unsteady portion of the signal was then routed through the calibration relay to the recording equipment.

Rotating Frame Wake Probe

A wake probe consisting of a triaxial hot-film probe to measure velocity and flow angles and a pressure transducer to measure total pressure was mounted immediately behind the rotor in the rotating reference frame (Fig. 14). The hot-film probe was a modified unit

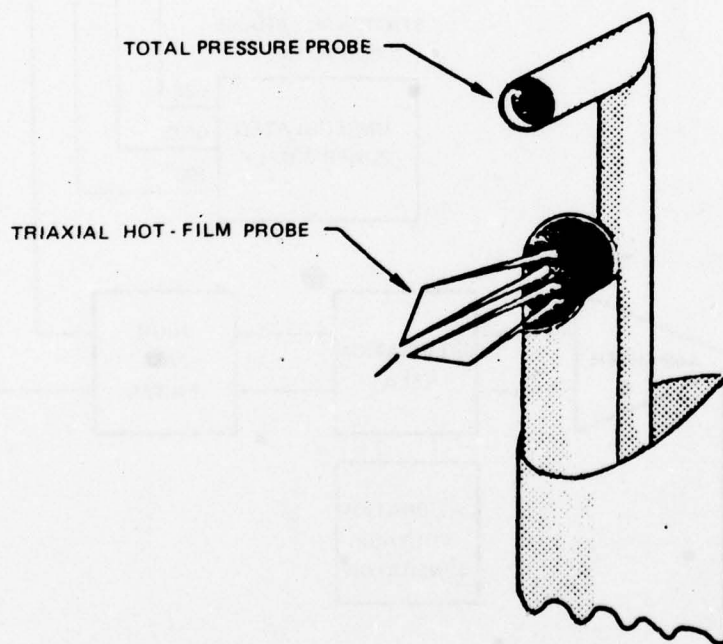


FIG. 14 WAKE PROBE USED IN LSRR

manufactured by Thermo Systems, Inc. and designated TSI 1296 M. Its sensors were operated in the constant temperature mode by anemometers

of the same type as those used with the skin friction gages (Appendix III). These anemometers were packaged differently because they were mounted in a different area of the hub than the others. As in the case of the skin friction gages, the anemometer output needed no further amplification and was routed through the slip rings to the stationary frame instrumentation. The time averaged portions of the signals were read from a digital voltmeter and manually recorded. Thus, even though the time-averaged portions were not recorded on tape, they were available so that the complete signals could be subsequently reconstructed. The remainder of the circuitry was identical to that used for the skin friction gages.

The total pressure in the wake was measured by a Kulite XCQL-093-25A pressure transducer mounted in a sharp edged tube (Fig. 15). The

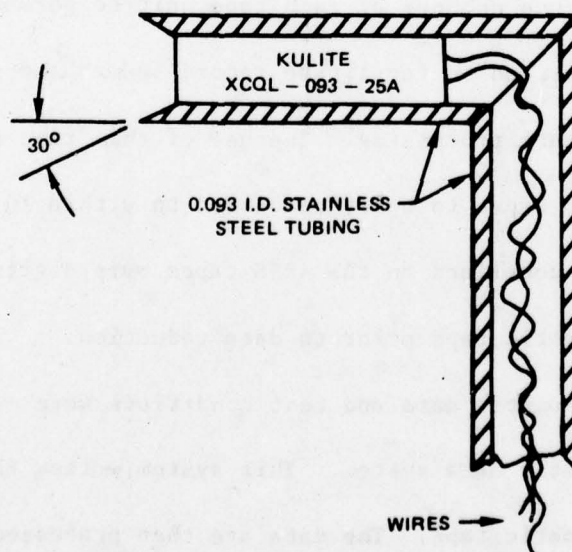


FIG. 15 KULITE TOTAL PRESSURE PROBE

circuitry used with this transducer was identical to that employed with the blade pressure transducers. In this particular instance, it was desired to obtain the steady as well as the unsteady portion of the total pressure from the transducer; consequently, the high-pass filter should have been switched out of the circuit. However, it was accidentally left in the circuit and only the unsteady part of the signal was recorded.

Data System

Unsteady data were recorded on the UTRC Analog Recording System (ARES), consisting of two fourteen-channel FM tape recording units and their associated amplifying and control equipment. (The calibration relays, instrumentation amplifiers, and tape units indicated in Figs. 12 and 13 were actually part of ARES.) A modified IKIG B time code was recorded on one channel of each tape unit to permit time correlation of the two tapes and to facilitate record search and playback during subsequent data processing. The use of this time code allows the data from the two tapes to be synchronized to within 10^{-4} seconds. The analog data contained on the ARES tapes were digitized and recorded on digital magnetic tape prior to data reduction.

The pneumatic data and test conditions were measured by the Test Stand 42 static data system. This system writes the data directly onto digital magnetic tape. The data are then processed using built-in calibration functions to provide the various parameters in physical units.

SCOPE OF EXPERIMENT

To place the present experiment in its proper perspective, it is useful to examine the possible modes in which a compressor may operate using Fig. 16. There are four main regimes in which operation is possible:

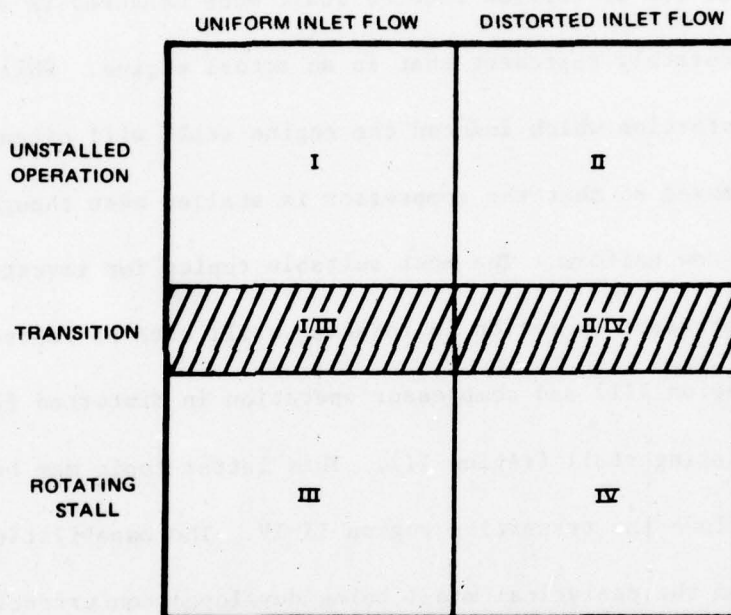


FIG. 16 FLOW REGIMES FOR COMPRESSOR OPERATION

- I) undistorted flow with no rotating stall
- II) distorted flow with no rotating stall
- III) undistorted flow with rotating stall occurring
- IV) distorted flow with rotating stall occurring

There are also two transition regions (I-II and II-IV) in which the compressor may move in and out of rotating stall. Region I is the

design operating condition of the compressor. The previously discussed problems may be seen to fall in regions II, III, IV and the transition region II-IV. Of these regions, IV is the one in which measurements are least meaningful, extremely difficult, and subject to a variety of errors. Even if measurements are made accurately, it is doubtful that the distortion-induced stall mode measured in a test rig will accurately represent that in an actual engine. This is because the distortion which induced the engine stall will often be subsequently removed so that the compressor is stalled even though the inlet flow is now uniform. The most suitable topics for investigation are thus compressor operation in rotating stall with no imposed distortion (region III) and compressor operation in distorted flow but without rotating stall (region II). This latter topic may be extended to include the transition region II-IV. The capabilities of the LSRR (and the analytical model being developed concurrently at NCSU (unpublished)) are best suited for investigation of both of these regions (II and II-IV). During this first experimental phase, measurements were made in all of the regions in order that the operating limitations of the LSRR and the capability of the available instrumentation to make meaningful measurements could be evaluated. However, following the reasoning outlined above, measurements were concentrated in region I to provide a baseline case and in region II to obtain unsteady data.

It is well known that an airfoil in a subsonic stream influences the upstream flow as well as the downstream flow. Extending this concept to a compressor, it is clear that the interaction between the rotor and the incoming distorted flow field establishes a velocity distribution at the compressor face that determines the inlet flow to which individual compressor blades respond. From a gap-averaged point of view, the unsteady response of a rotor blade row is dependent on the imposed inlet angle variations. Thus, a rotating blade in a multi-stage machine may be thought of as being affected by its neighboring blade rows primarily through the imposed or induced upstream flow angle distribution. The measurement and understanding of the variations in the performance of a single blade row with inlet angle is therefore a necessary prelude to the understanding of the complex interactions in a multistage machine. The performance of a blade row may be quantified in terms of the variations in flow exit angle and total pressure loss with changing inlet angle. This inlet angle distribution may be simply the result of an imposed distortion or it may arise from the interactions of the rotor with other components such as downstream stators, diffusers, struts, etc. Of course, the blade row performance may be more easily and more completely understood if the inlet angle variation is simple. In the past, various investigators have studied sinusoidal distortions, square-wave distortions and ramp or triangle-wave distortions. The present

experimental program was aimed at measuring the response of an isolated rotor to a sinusoidal variation in inlet axial velocity. This choice was made for a number of reasons. First, the sinusoidal distortion is relatively easy to produce (Ref. 20). Second, the square- and triangular-wave distortions may be represented in terms of the sine-wave by means of a Fourier Series. The study of sinusoidal distortion patterns of various reduced frequencies will thus yield information pertinent to other types of distortions. Finally, the square- and triangular-wave distortions may be thought of as having higher order harmonics which may make the understanding of the rotor response more difficult. Conversely, the sine-wave distortion contains only one harmonic. The reduced frequency may be readily controlled by varying the number of cycles of the distortion pattern the screen produces. In the present experiment, a one-cycle-per-revolution screen (and the attendant low reduced frequency) was chosen to produce some unsteady effects without causing a significant departure from the steady state behavior.

EXPERIMENTAL PROCEDURE

Data Acquisition

During this experiment, the LSRR was operated at a constant corrected wheel speed of 600 rpm. For a given upstream total temperature, T_{o1} , the actual rotational speed required to achieve the corrected wheel speed of 600 rpm is given by Eq. (1).

$$N_{act} = 600 \frac{T_{o1}}{518.7^{\circ}R} \quad (1)$$

The rotor rpm was measured by a digital tachometer and was found to be stable once it had been set. The axial velocity in the case of undistorted flow was varied so that the blade incidence angle (referred to the mean camber line) ranged from a high negative value ($\alpha_{mcl} = -18^{\circ}$) up to the point of rotating stall inception ($\alpha_{mcl} = 1.5^{\circ}$). In distorted flow, the mean incidence angle was varied over approximately the same range. Due to the 20 percent distortion in inlet axial velocity, the instantaneous inlet angle varied on the order of $\pm 6^{\circ}$ about the mean angle. In all cases tested, the stall mode was observed to be a multiple-cell, partial-span rotating stall near the rotor hub. To set the desired axial velocity, a U-tube manometer was connected between a wall static tap and a total pressure probe located in the center of the annulus. The axial position of both the static tap and the total pressure probe was midway between the rotor and the distortion screen. The measuring station was located at the

90° point in the distortion pattern where the local axial velocity would be equal to the average axial velocity if there were no preswirl. A more accurate measurement of the circumferential distribution of axial velocity was made using a circumferential array of measuring stations. This axial velocity distribution was used in reducing the data, but the visual reading obtained from the single U-tube manometer proved adequate for setting the operating point.

The number of channels which could be simultaneously transmitted from the rotating frame was limited to 17 by the slip ring assembly. It was thus necessary to run two instrumentation configurations to obtain the desired data. The first configuration obtained data from the complete set of pressure transducers plus selected skin-friction gages. The pressures were integrated to obtain blade normal force and pitching moment coefficients. The second instrumentation configuration included all the suction surface pressure transducers and skin friction gages as well as the wake probe. For a given flow condition, the wake probe was traversed across about 1.5 blade gaps giving particular emphasis to the blade wake regions. Due to the time involved in making this traverse and the mass of data which would be obtained, only a few flow conditions were run in this configuration.

The instrumentation available in each of the two configurations is presented in Appendix IV which also includes a chronological

listing of the test points run. Notes are included to point out problems encountered during the tests which may influence the accuracy of the results.

Once a desired operating condition had been reached and the flow had stabilized, the gain of each channel of the unsteady data system was set as high as possible without overloading the tape recording equipment. An oscilloscope was used to monitor the tape inputs to insure that the signal was within the required limits. Calibration records were then acquired for both the static and unsteady data systems and the data were recorded immediately thereafter. If a wake traverse were being made with the rotating frame wake probe, static data would be taken only at the first point for each flow condition.

The data from the static system was subsequently converted to pressures and temperatures by a computerized process making use of the calibration records. The unsteady data were digitized by the process of Ref. 23. After completion of the digitizing process, the calibration records were used to convert the data to appropriate physical units.

Overall Performance Parameters

The wall static and mid-span total pressures were obtained at eight circumferential stations 45° apart approximately 1.5 chord lengths upstream of the rotor. Using the Bernoulli equation, the velocity at each of these was calculated. The velocity was assumed

to be purely axial at these locations. Limited flow angle measurements in undistorted flow did verify this assumption. These velocities were then fitted to the form given below in Eq. (2) by a least squares technique.

$$C_x(\theta) = \bar{C}_x + A \cos(\theta + \phi) \quad (2)$$

The angle θ is the circumferential position in the distortion pattern and increases in the direction of rotation of the rotor. The quantity \bar{C}_x is the average value of the axial velocity and the constants A and ϕ are the amplitude and phase angle of the velocity variation, respectively. The static pressure upstream of the rotor was fitted to the form given by Eq. (3).

$$P_{s_1}(\theta) = \bar{P}_{s_1} + B \cos(\theta + \psi) \quad , \quad (3)$$

where \bar{P}_{s_1} is the average value of the static pressure and B and ψ are the amplitude and phase angle of the pressure variation. The Bernoulli equation was applied once again to obtain a smoothed total pressure profile around the distortion which is consistent with the velocity and static pressure profiles obtained from the curve fits. A small pressure and velocity distortion was found to exist even with the distortion screen removed. The velocity distortion without the screen varied between two and four percent. With the screen in place, this pre-existing distortion was found to interact with that of the screen to produce a net distortion of lower amplitude than had been anticipated. For all of the results presented, the measured

upstream conditions as smoothed by the previously discussed techniques are used. The inlet flow angle, β_1 , is based on the axial velocity at the upstream measuring station and does not include any swirl that may have occurred between that axial position and the rotor inlet face. The inlet angle is given by

$$\beta_1 = \tan^{-1} \frac{C_x}{U} . \quad (4)$$

For distorted inlet flow, the inlet angle will vary with position in the distortion pattern; however, an average inlet angle, $\bar{\beta}_1$, may be calculated by inserting the average axial velocity, \bar{C}_x , into Eq. (4).

The exit angle, β_2 , is an important measure of the performance of the rotor. For undisturbed flow, this angle was computed from the measured stationary frame flow angle downstream of the rotor, θ_2 .

The computation was iterative and began by assuming that the axial velocity downstream of the rotor was identical to that upstream. The exit angle is given by

$$\beta_2 = \tan^{-1} \frac{C_{x2}}{U - C_{x2} \tan\theta_2} , \quad (5)$$

where C_{x2} is the downstream axial velocity at midspan. Note that the spanwise averaged axial velocities upstream and downstream of the rotor must be identical to satisfy conservation of mass. However, due to the thickening of the wall boundary layers at the root and tip of the blading, the midspan axial velocity downstream of the rotor will, in general, be greater than that upstream of the rotor. The

importance of this phenomenon was not fully realized at the outset of the experiment and no provision was made for measuring the axial velocity downstream of the rotor. Instead, it was assumed to be the same as that upstream of the rotor. When the magnitude of the error thus introduced was realized, it became necessary to devise a method of estimating the downstream axial velocity. Horlock (Ref. 24) presents a correlation between the axial velocity ratio across a cascade and the flow turning due to Rhoden (Ref. 25). Using this correlation, one may iterate to obtain the correct exit angle. As a check on the validity of this correction, the exit angle was also calculated using a simple momentum theory (see Appendix V).

Another important performance parameter is the rotor pressure rise coefficient which is defined as

$$C_{p_r} = \frac{P_{s_2} - P_{s_1}}{1/2\rho U^2} \quad (6)$$

where P_{s_2} is the downstream static pressure, ρ is the fluid density, and U is the tangential wheel speed. To be consistent, this coefficient must be defined at the blade midspan. Therefore, the downstream static pressure must be corrected (from a wall value) using the radial equilibrium equation.

$$\frac{\partial P}{\partial r} = \rho \frac{C_\theta^2}{r} \quad (7)$$

Integrating, we obtain

$$P_{\text{tip}} - P_1 = \int_{r_1}^{r_{\text{tip}}} \rho C_\theta^2 \frac{dr}{r}, \quad (8)$$

where P_{tip} is the pressure at the blade tip (outer casing) and P_1 is the pressure at the radial station in question. The radii, r_1 and r_{tip} , are those of the station in question and the tip, respectively. This equation may be greatly simplified by assuming ρ and C_θ to be constants

$$P_{\text{tip}} - P_1 = \rho C_\theta^2 \ln\left(\frac{r_{\text{tip}}}{r_1}\right) \quad (9)$$

and the result may be used to calculate the static pressure at the blade midspan from measured pressures on the outer casing.

A final important parameter used to measure the performance of a compressor stage is the loss coefficient. For undistorted flow, the steady-state loss coefficient is given by

$$X_{SS} = \frac{P'_{o1} - P'_{o2}}{\frac{1}{2}\rho W_1^2} \quad (10)$$

where P'_{o1} and P'_{o2} are the total pressures upstream and downstream of the rotor, respectively, in the rotating reference frame and W_1 is the relative velocity upstream of the blading (see Fig. 6).

Unsteady Blade Pressures

Reduction of the unsteady data requires that the pressures measured on the surface of the blade be converted to an appropriate

nondimensional form. The most relevant parameter to use is the pressure coefficient defined by

$$C_P = \frac{P - P_{s1}}{\frac{1}{2}\rho W_1^2} \quad (11)$$

where P_{s1} is the static pressure upstream of the blade leading edge. With distorted inflow, this parameter varies as the blade traverses the distortion. The relative velocity, W_1 , is used to nondimensionalize the pressure coefficients. It should be noted that W_1 is not constant but varies around the distortion. The computed coefficients are phase-lock averaged over five cycles (Ref. 26) to minimize the effects of any random fluctuations in the pressure data. A Fourier series representation of the average pressure coefficient variation at each chordwise station was computed using the formula

$$C_P(\theta) = a_0 + \sum_{n=1}^N [a_n \cos n \theta + b_n \sin n \theta] \quad (12)$$

and the coefficients of this series were then filtered with a cosine-square, low-pass filter (Ref. 27). The cutoff frequency of the filter was chosen to retain the response of the blade pressures to the distortion but to remove the response of these pressures to screen irregularities (e.g., screen support spokes). Figure 17 shows typical data from the pressure transducer nearest the leading edge on the suction surface after each stage of processing. The top curve is the raw data over one cycle after scaling to proper coefficient form.

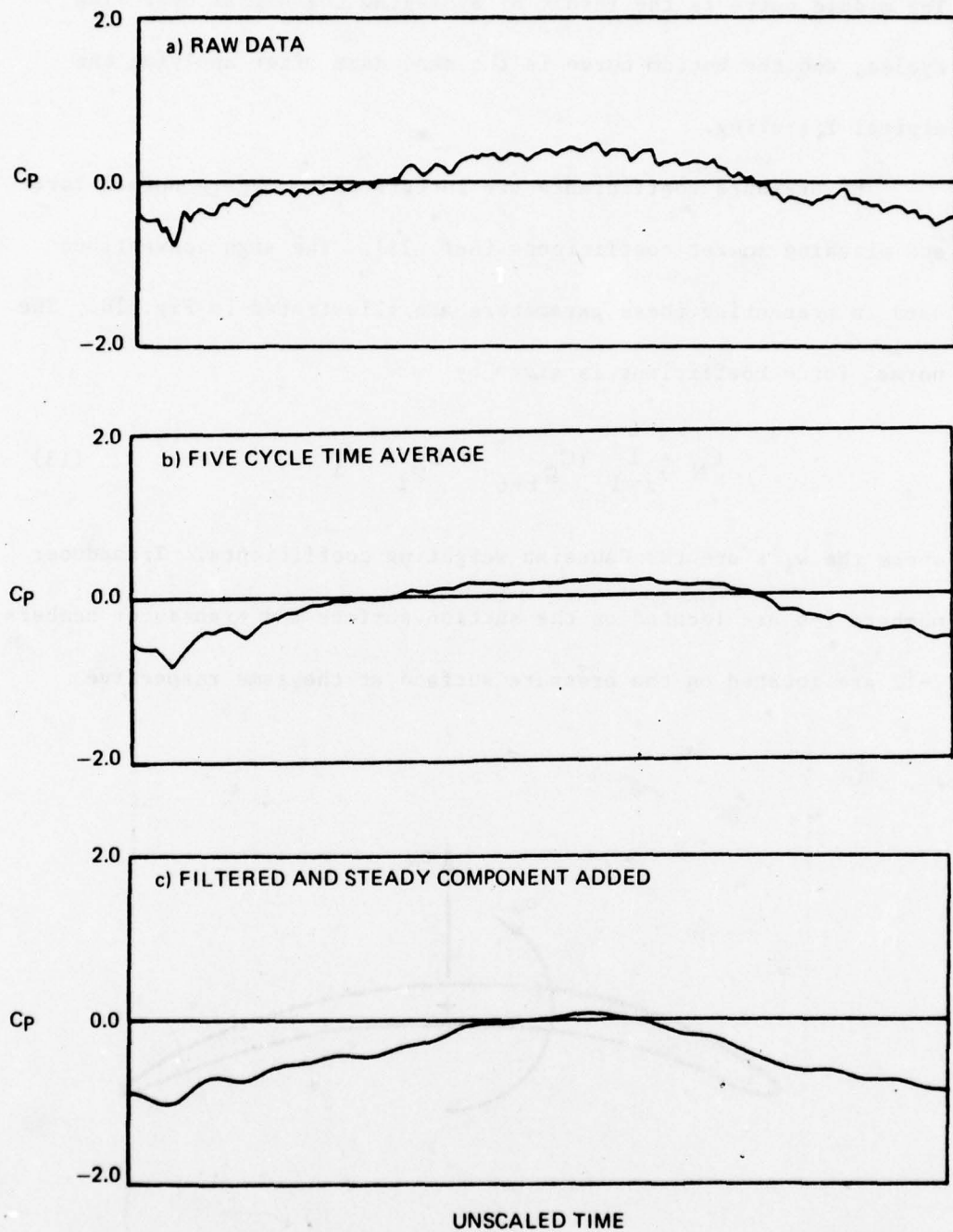


FIG. 17 TYPICAL PRESSURE TRANSDUCER DATA AFTER EACH STAGE OF PROCESSING

The middle curve is the result of averaging the signal over five cycles, and the bottom curve is the same data after applying the digital filtering.

The pressure coefficients are integrated to obtain normal force and pitching moment coefficients (Ref. 21). The sign conventions used in presenting these parameters are illustrated in Fig. 18. The normal force coefficient is given by

$$C_N = \sum_{i=1}^6 (C_{P_{i+6}} - C_{P_i}) w_i \quad (13)$$

where the w_i 's are the Gaussian weighting coefficients. Transducer numbers 1-6 are located on the suction surface and transducer numbers 7-12 are located on the pressure surface at the same respective

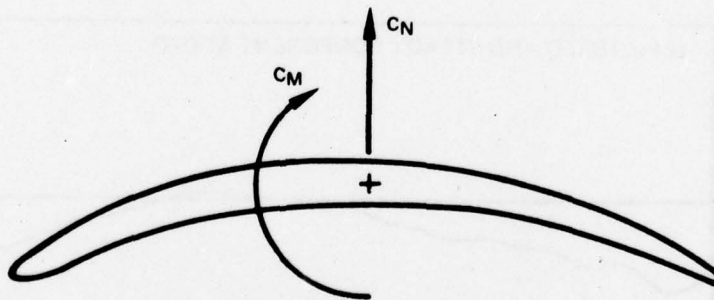


FIG. 18 SIGN CONVENTIONS FOR NORMAL FORCE AND PITCHING MOMENT COEFFICIENTS

chordwise positions. The pitching moment coefficient about the midchord is given by

$$C_M = \sum_{i=1}^6 (C_{p_{i+6}}) w_i (x_i - 0.5) \quad , \quad (14)$$

where the x_i 's are the chordwise positions of the measuring stations expressed as fractions of the chord. The Gaussian positions and weighting factors used in these equations are presented in Table I. Even with only six chordwise stations, the Gaussian integration technique may be expected to yield normal force and pitching moment coefficients accurate to within three percent (Ref. 22).

Transient Surface Flow Phenomena

Hot film skin friction gages were positioned adjacent to each pressure transducer in an attempt to correlate the pressure fluctuations with surface flow phenomena. The hot film gage is a resistance element which is heated by passing electrical current through it. A constant-temperature anemometer circuit is employed to keep its resistance and hence its thermometer constant. By monitoring the power necessary to accomplish this, it is possible to obtain a qualitative measure of the heat transfer to the fluid. McCroskey (Ref. 28) gives this relation as

$$I^2 R \propto A + Q \quad , \quad (15)$$

where I is the current through the gage and R is its resistance. The heat transfer is composed of two parts; the nonflow heat losses, A ,

and a nondimensional forced convection loss, Q . Normally, the current through the gage is not measured directly. Instead, the anemometer output voltage is measured; however, the relationship between the gage current and output voltage is such that

$$E^2 \propto A + Q \quad (16)$$

This voltage is composed of a steady part, \bar{E} , and a time-varying part, e , which is much less than \bar{E} . For the present study, only qualitative data are desired from the skin friction gages; hence, only the time varying part of the heat transfer need be retained. Neglecting higher order terms in the time-varying voltage yields

$$e \propto \tilde{Q} \quad (17)$$

where \tilde{Q} is the time varying portion of the forced convection. From Ref. 29

$$Q \propto \tau_w^{\frac{1}{2}} \quad (18)$$

where τ_w is the shearing stress at the wall. The skin friction coefficient is defined as (Ref. 29)

$$C_f = \frac{\tau_w}{\frac{1}{2}\rho W^2} \quad (19)$$

Considering only the time-varying part of the skin friction coefficient, we may write

$$\tilde{C}_f \propto e \left(\frac{W_1}{W_1}\right)^{\frac{1}{2}} \quad (20)$$

Although the quantity on the right of Eq. (20) has the units of volts, it has been corrected for local velocity variations and will be used as an indicator of the variations in the skin friction coefficient. It is not valid to compare the amplitudes of this parameter at different flow conditions because the constant of proportionality need not be the same in the two cases. Furthermore, only the varying part of the skin friction is being considered; thus, when the quantity $e(\frac{\bar{w}_1}{w_1})^{2/3}$ becomes zero, this does not mean that the total skin friction coefficient, C_f , is zero. In presenting this data, no averaging or filtering techniques are employed because the high frequency fluctuations in the parameter defined by Eq. (20) are needed to judge whether transition or separation has occurred.

Velocity Measurements at the Rotor Exit Plane

A complete description of the calibration procedure developed for the triaxial hot-film probe used in this experiment appears in Appendix V. It was determined that the response of each of the sensors to a purely normal velocity obeyed the relation

$$E^2 - E_0^2 = k\sqrt{\rho V} (T_s - T_\infty) \quad (21)$$

if one postulated that the empirical constants E_0 and k might have one value at high velocities and another at low velocities. Here, E is the bridge output voltage and ρ and V are the fluid density and velocity (assumed to be normal to the sensor). The temperatures T_s and T_∞ are those of the sensor and free stream, respectively. The

constants E_0 and k were determined in the calibration procedure (Appendix V). The equation may be rewritten to give an effective normal velocity as a function of these calibration constants, the fluid properties, and the anemometer output voltage.

$$q = \left[\frac{E^2 - E_0^2}{k\sqrt{\rho} (T_s - T_\infty)} \right]^2 \quad (22)$$

It was found that the best relation between the sensed normal velocity, q , and the actual normal velocity, U_n , was given by

$$q^2 = u_n^2 f(\theta, \phi). \quad (23)$$

The function $f(\theta, \phi)$ is dependent on the pitch and yaw angles of the flow relative to the probe (θ and ϕ , respectively) and is evaluated using the calibration data. This function is different for each sensor. Given values of θ and ϕ , one may evaluate the function for each wire. Making use of the fact that the three sensors are mutually orthogonal, one may write Eq. (23) for each sensor.

$$\frac{q_1^2}{f_1} = u_2^2 + u_3^2 \quad (24)$$

$$\frac{q_2^2}{f_2} = u_1^2 + u_3^2 \quad (25)$$

$$\frac{q_3^2}{f_3} = u_1^2 + u_2^2 \quad (26)$$

In these equations, f_i is the value of the function $f(\theta, \phi)$ for the i^{th} sensor evaluated at the assumed angles θ and ϕ and u_i is the velocity parallel to the i^{th} sensor. These equations may be solved easily for the squared velocity components u_i^2 . Since there is no way to evaluate the algebraic sign of u_i from this process, it must be known from some other source. In the present experiment, the orientation of the probe was such that the velocity components may be assumed to have the positive sign. Using these velocities, the assumed angles were updated and the process repeated until convergence was obtained. A more complete description of the iteration process and the equations involved may be found in Appendix V. The final result is expressed in terms of the relative velocity at the exit plane, W_2 , the flow angle in the axial-circumferential plane, β_1 , and the flow angle in the axial-radial plane, ψ . If one defines the velocities v_1, v_2, v_3 to be the radial, circumferential, and axial velocity components, respectively, then relative velocity and flow angles are given by:

$$W_2 = \sqrt{v_1^2 + v_2^2 + v_3^2} \quad (27)$$

$$\beta_2 = \tan^{-1} (v_2/v_3) \quad (28)$$

$$\psi = \tan^{-1} (v_1/v_3) \quad (29)$$

The relative velocity and the two flow angles were computed for five revolutions with roughly 200 data points per cycle. These data were represented by Fourier Series in terms of the circumferential position in the flow field so that the parameters of interest could later be reconstructed at any desired rotor position.

RESULTS

The notation used herein is that employed in turbomachine work by UTRC. In particular, the variable against which most of the data are plotted is the rotor inlet angle, β_1 . This angle has previously been defined in Eq. 4 (see Fig. 6). It should be noted that increasing β_1 corresponds to decreasing angle of attack. Further, the mechanism by which the inlet angle is changed is to vary the axial velocity at constant rotational speed. Consequently, the effects of the varying inlet angle (or angle of attack) cannot be totally separated from the effects of the varying velocity. Proper nondimensionalization of the various measured quantities can eliminate the velocity effects in the case of quasi-steady flow. However, unsteady effects of the varying velocity are still present. The method employed to illustrate the effects of unsteadiness in the flow is to plot the unsteady response of the rotor undergoing inlet distortion superimposed on its steady-state behavior. This steady-state behavior was determined by running the rotor at different inlet angles in undistorted flow.

Overall Performance

The annulus averaged pressure rise coefficient across the rotor (defined by Eq. (5)) is shown in Fig. 19 for both undistorted and distorted flow. For distorted flow, the pressure rise is circumferentially

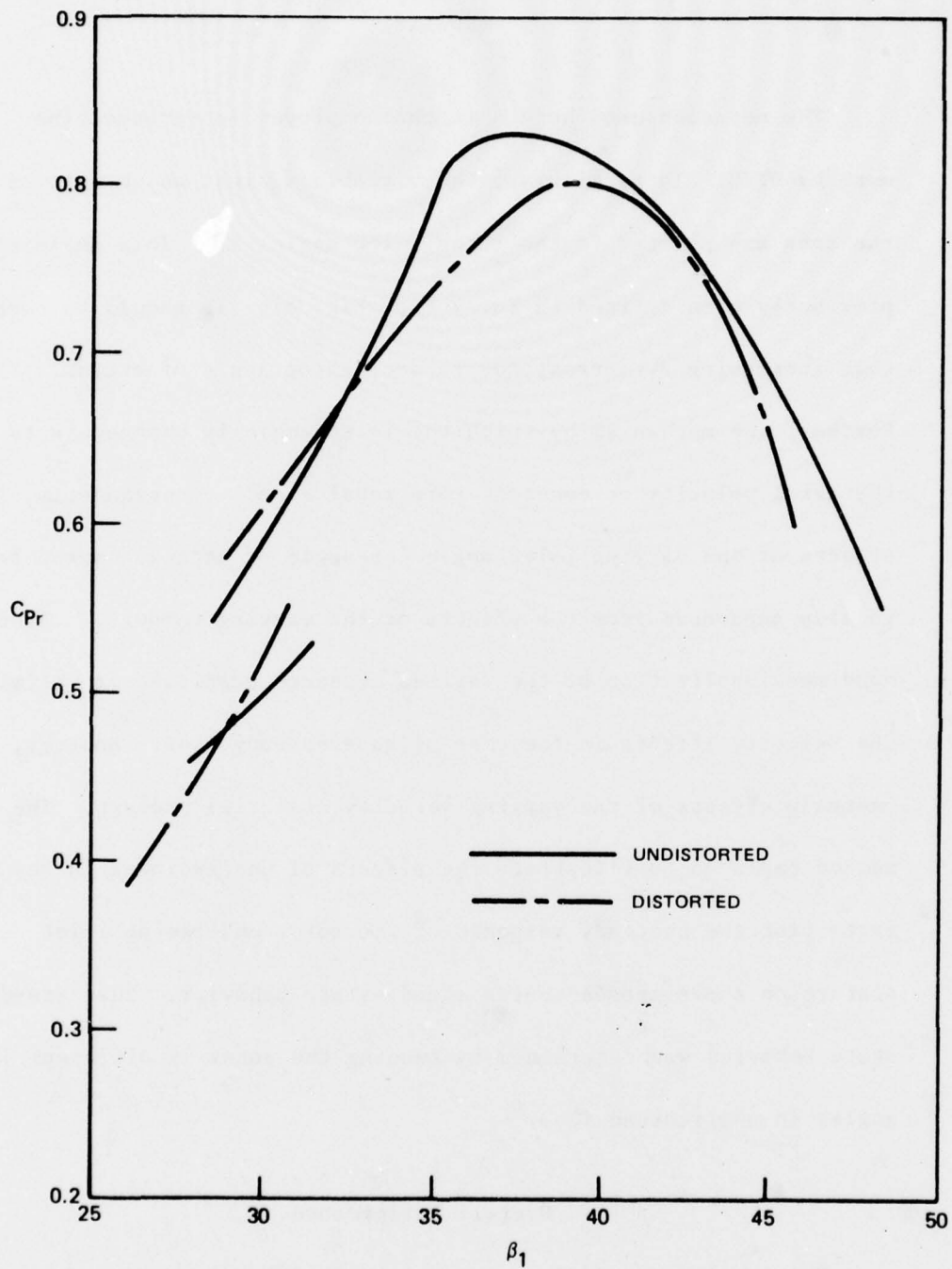


FIG. 19 ROTOR PRESSURE RISE AS A FUNCTION OF INLET ANGLE

averaged and plotted as a function of the average inlet angle. The upper branch of each curve represents unstalled flow and the lower branch represents stalled operation. (Refer back to Fig. 3 and the associated text for a more complete discussion of the discontinuous behavior of the curves.) The undistorted curve shows a significantly greater peak pressure rise and is slightly higher than the distorted curve over the higher inlet angles. However, at the lower inlet angles, where the blade loading is higher, the unsteady effects cause the distorted flow condition to give slightly higher pressure rise. Note that the incidence angle (relative to the mean camber line) at which stall occurs is very low, only 1.5° for undistorted flow. (The incidence angle is the difference between the stagger angle, β_1^* , which is 30° in this case and the inlet angle.) This is possible because the blade profile is highly cambered and can produce large turning angles (and consequent high normal forces) at low incidence angles. The low incidence angle at stall is common to highly cambered blades.

The loss coefficient of Eq. (6) is plotted as a function of inlet angle in Fig. 20 for undistorted flow only. Suitable equipment for measuring the unsteady loss was not available when this experiment was run.

To complete the presentation of the overall performance parameters, we will consider the variation of the exit flow angle as a function of the inlet angle (again, for undistorted flow only) as

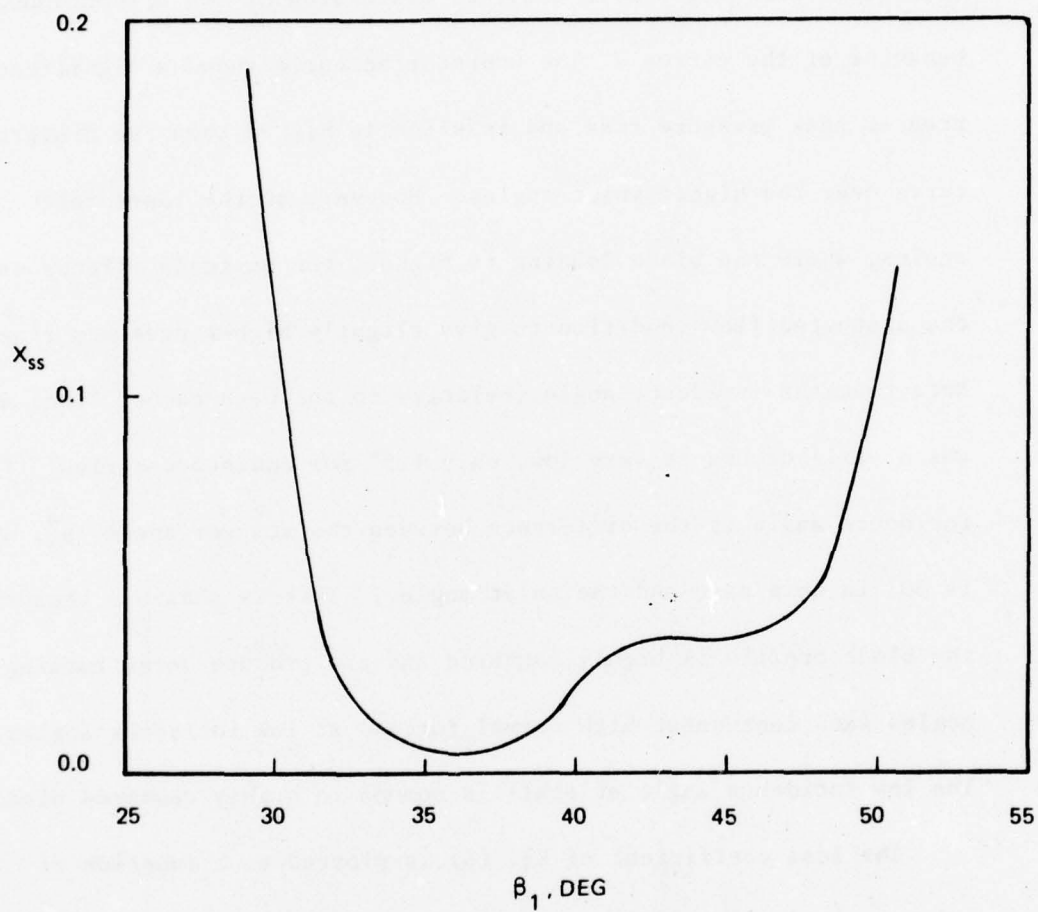


FIG. 20 STEADY-STATE LOSS COEFFICIENT AS A FUNCTION OF INLET ANGLE

shown in Fig. 21. Curves are presented for the basic wedge probe measurements, for a momentum theory calculation (see Appendix V), and for cascade data taken from Ref. 24 for a similar profile having the same stagger angle and gap-to-chord ratio. The three curves show reasonable agreement for only a narrow range of inlet angles ($39^\circ < \beta_1 < 45^\circ$) with large differences at the lower values of inlet angle (high blade loading). Several factors may account for these differences and most of them are in some way associated with the three-dimensionality of the flow. First, the correction for axial velocity variation across the rotor is empirical and may not be accurate at high blade loadings. This would introduce errors into the exit angle as calculated from the wedge probe measurements. Second, the radial velocity may not be zero as was assumed. The midspan behavior would not be representative of the average blade performance; hence, the wedge probe measurements could not be expected to agree with the two-dimensional cascade data. Furthermore, the radial equilibrium correction to the rotor pressure rise would be in error thus introducing error into the momentum theory calculations. Finally, the blade wakes may introduce enough unsteadiness into the flow so that the flow angles measured by the wedge probes are in error (c.f., Ref. 18). At the higher inlet angles, the exit angle as calculated from the wedge probe measurements is in good agreement with the cascade data but that from momentum theory appears to be diverging. Since

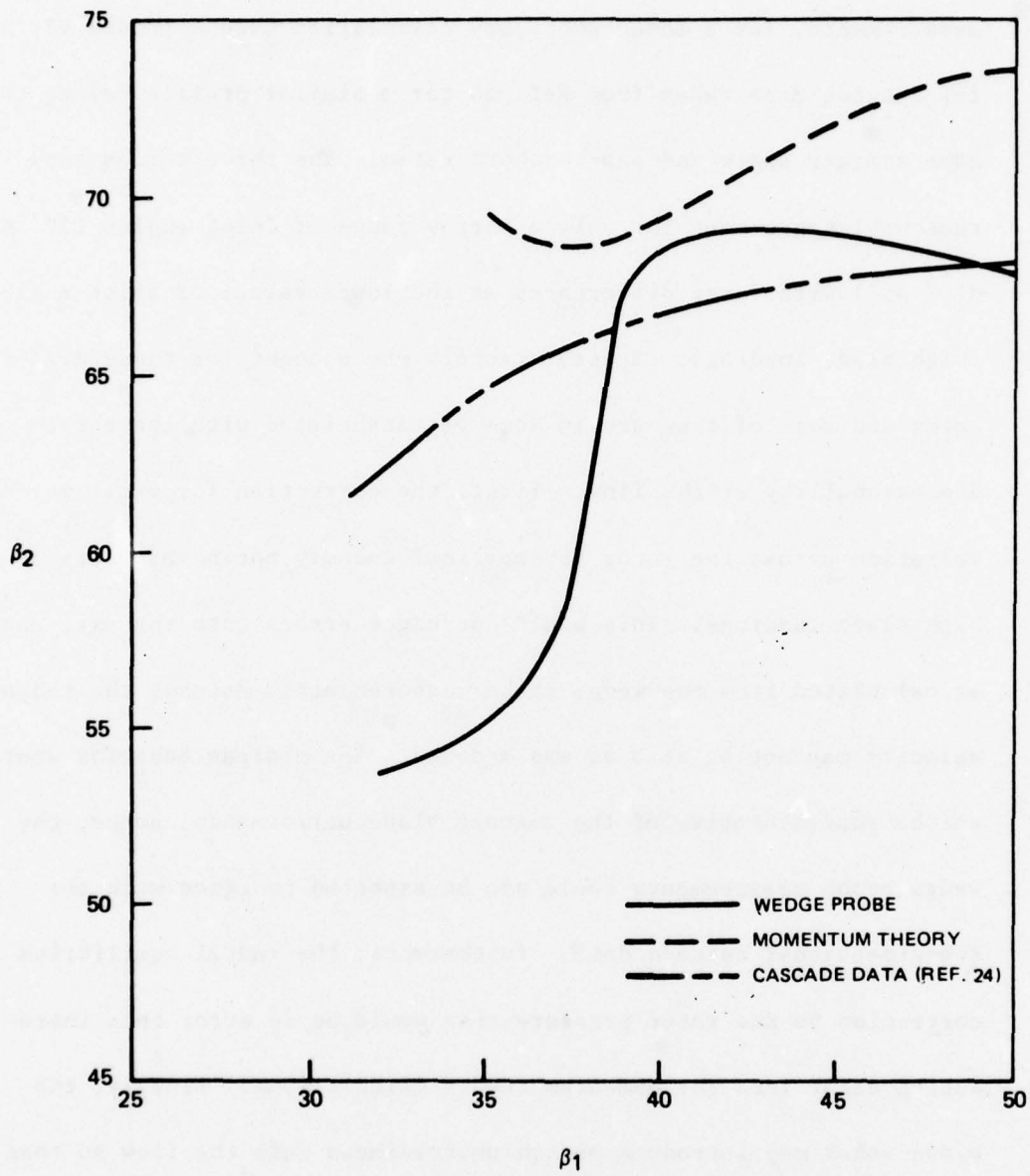


FIG. 21 EXIT ANGLE AS A FUNCTION OF INLET ANGLE

the momentum theory calculations is subject to the greatest number of errors, the observed differences are not considered excessive. It must be surmised that the placing of a single wedge probe at the midspan location is not an adequate means of measuring the exit angle. A more prudent method would be to use a spanwise array of high response (hot-wire or hot-film) probes.

Analysis of Unsteady Data

It has been stated that the method used to determine the effects of the unsteadiness generated by the distortion will be to plot the various parameters as a function of the inlet angle. This process normally results in a loop which will generally be superimposed on the quasi-steady characteristic. Before discussing the experimental data, several simple examples will be given to illustrate how these loops are derived and how their character may be related to changes in the amplitude and phase angle of the response. Consider the two variables x and y which are sinusoidal functions of time.

$$x = A \sin \omega t \quad (30)$$

$$y = B \sin (\omega + \phi) \quad (31)$$

Suppose x is a displacement and y is a response due to the displacement. The amplitude of the displacement is A , that of the response is B , and ϕ is the phase angle by which the response leads the displacement. Some ways in which x and y may vary are shown in Fig. 22

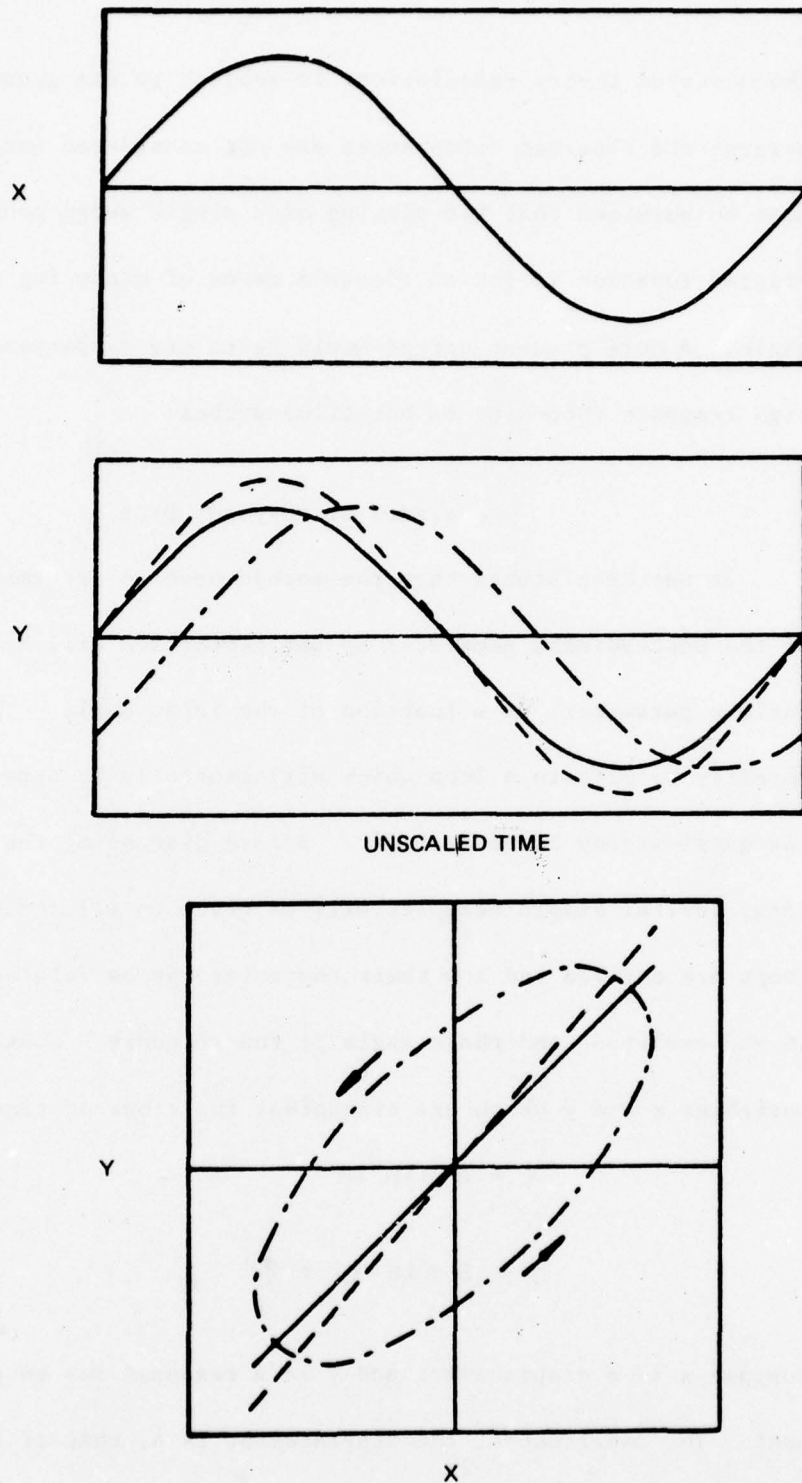


FIG. 22 GENERATION OF A LOOP AND THE POSSIBLE EFFECTS OF UNSTEADINESS

together with the loops which result from plotting y as a function of x . If the two variables are in phase, y is a linear function of x and the slope is indicative of the relative amplitudes of x and y (e.g., solid and dashed lines in Fig. 22). If the two variables are not in phase plotting y as a function of x produces an ellipse (dash-dot lines in Fig. 22). The small arrows indicate the direction in which the loop is traversed. When the slope of the major axis of the loop is positive, the counterclockwise sense shown in Fig. 22 indicates that the response lags the displacement. If the slope of the loop is negative, a clockwise sense indicates a lagging response and a counterclockwise sense indicates a leading response.

In the case of a compressor rotor, the inlet angle may be considered to be the displacement mentioned above and the blade pressures, etc. are the responses. Actually, none of these are pure sinusoids and the generated loops will not be simple ellipses. However, certain basic similarities do exist between this illustrative example and the actual measured data. Therefore, comparing the unsteady responses (obtained while operating under the influence of the inlet distortion) to their steady counterparts (obtained with undistorted flow) will reveal the nature and extent of unsteady effects. First, the slope of the loop relative to the steady state curve will indicate whether unsteadiness has changed the amplitude of the response. Second, the openness of the loop will show phase shift

and, if the loop has a definite positive or negative slope, the direction in which the loop is traversed will indicate whether the response leads or lags the inlet angle. A loop which is horizontal indicates a phase angle near 90° (or 270°). It should be noted that in the inlet distortion problem the leading and lagging phase angles do not imply stability or instability as is the case with an oscillating airfoil (or a cascade of airfoils); rather, the phase angle is simply an indication of unsteadiness.

Blade Pressures

The most instructive form for presenting the blade pressures is the difference between the pressure coefficient on the pressure surface and that on the suction surface. This differential pressure coefficient is given by

$$\Delta C_{p_i} = \left[C_{p_{\text{press}}} - C_{p_{\text{suct}}} \right]_i \quad (32)$$

where the subscript i refers to the chordwise station in question. Since the individual coefficients were already represented as Fourier Series (of the form given by Eq. (12)), it is a simple matter to obtain the series representations of the differential pressure coefficients. These were converted to an amplitude/phase angle format

$$\Delta C_{p_i} = a_0 + \sum a_n \cos(n\theta + \phi_n) \quad (33)$$

where a_0 is the steady component and a_n and ϕ_n are the

amplitude and phase angle of the n th harmonic, respectively. The upper limit of the summation, N , is a function of the cutoff frequency of the digital filter and θ is the angular position in the distortion field with the point of maximum axial velocity being $\theta = 0$.

Three flow conditions were chosen as representative of those for which data were available. The mean inlet angles associated with these flow conditions are indicated by tic marks on the undistorted rotor pressure rise curve (Fig. 23). These angles represent low (7.15), medium (7.9), and high (7.4) blade loading. It is instructive to compare the amplitudes and phase angles of the first few harmonics of the differential pressure coefficients and the integrated normal force and pitching moment coefficients (Table II). One concludes that the first harmonic is dominant (as much as an order of magnitude greater than the higher harmonics). The response at the leading edge stations is significantly greater than that at stations farther aft on the blade. This peaking of the response at the leading edge seems to be more pronounced at higher blade loading. The lack of activity near the trailing edge is also noteworthy.

The differential pressure coefficient loops for each of the six chordwise measuring stations are presented in Fig. 24. At the leading edge ($x/c = 0.034$), one observes that the amplitude of the response has been increased and that the response consistently lags the inlet angle. Horlock, Greitzer, and Henderson (Ref. 30) have

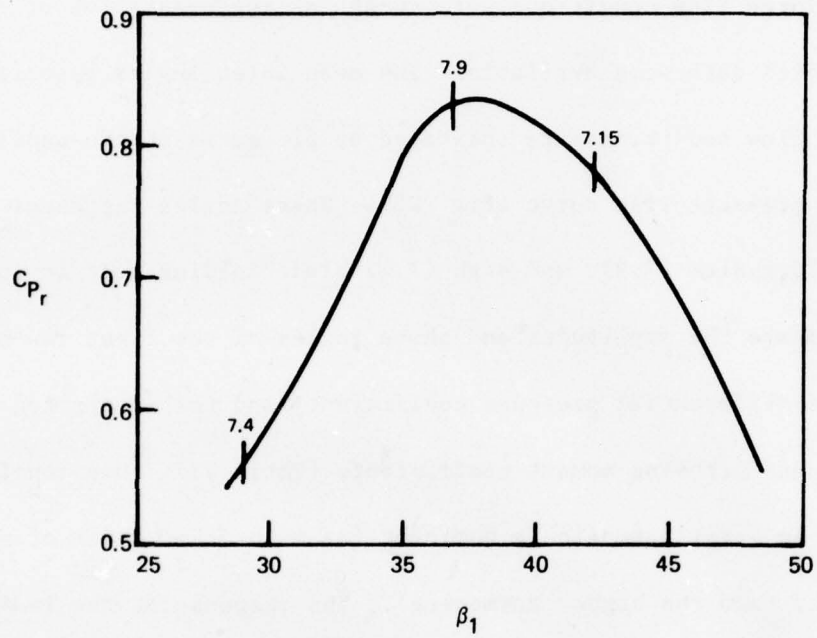


FIG. 23 INLET ANGLES FOR WHICH DISTORTED FLOW DATA ARE PRESENTED

HARMONIC CONTENT OF DIFFERENTIAL PRESSURE,
NORMAL FORCE AND PITCHING MOMENT COEFFICIENTS.

(a) Point 7.4 $\beta_1 = 28.9 + .061 \cos \theta$

	a_1	ϕ_1	a_2	ϕ_2
$x/c = 0.034$	1.201	172.0°	0.131	182.8°
$x/c = 0.169$	0.158	196.9°	0.025	273.6°
$x/c = 0.381$	0.181	285.1°	0.034	199.4°
$x/c = 0.619$	0.058	262.1°	0.013	81.1°
$x/c = 0.831$	0.035	163.9°	0.027	249.4°
$x/c = 0.966$	0.047	221.5°	0.028	258.4°
C_N	0.138	200.9°	0.023	209.8°
C_M	0.052	178.5°	0.005	177.5°
	a_3	ϕ_3	a_4	ϕ_4
$x/c = 0.034$	0.129	289.1°	0.042	283.0°
$x/c = 0.169$	0.007	214.8°	0.002	52.8°
$x/c = 0.381$	0.018	65.2°	0.007	22.1°
$x/c = 0.619$	0.019	251.3°	0.006	58.2°
$x/c = 0.831$	0.006	91.1°	0.007	309.8°
$x/c = 0.966$	0.007	331.7°	0.006	309.2°
C_N	0.011	288.1°	0.005	328.7°
C_M	0.005	288.9°	0.001	276.4°

TABLE II (Cont'd)

HARMONIC CONTENT OF DIFFERENTIAL PRESSURE,
NORMAL FORCE AND PITCHING MOMENT COEFFICIENTS.

(b) Point.7.9 $\beta_1 = 36.9 + .068 \cos \theta$

	a_1	ϕ_1	a_2	ϕ_2
$x/c = 0.034$	0.757	173.9°	0.009	296.3°
$x/c = 0.169$	0.244	181.2°	0.027	204.3°
$x/c = 0.381$	0.074	252.0°	0.029	271.7°
$x/c = 0.619$	0.206	317.4°	0.039	288.5°
$x/c = 0.831$	0.030	271.9°	0.036	131.6°
$x/c = 0.966$	0.133	173.7°	0.023	109.8°
C_N	0.101	207.8°	0.013	242.4°
C_M	0.045	172.2°	0.003	271.0°
	a_3	ϕ_3	a_4	ϕ_4
$x/c = 0.034$	0.063	166.0°	0.039	114.9°
$x/c = 0.169$	0.037	136.6°	0.008	109.8°
$x/c = 0.381$	0.002	305.2°	0.004	75.6°
$x/c = 0.619$	0.020	19.6°	0.017	33.2°
$x/c = 0.831$	0.012	53.9°	0.004	115.7°
$x/c = 0.966$	0.016	115.3°	0.011	190.7°
C_N	0.011	115.0°	0.008	86.7°
C_M	0.005	171.1°	0.002	112.8°

HARMONIC CONTENT OF DIFFERENTIAL PRESSURE,
NORMAL FORCE AND PITCHING MOMENT COEFFICIENTS.

(c) Point.7.15 $\beta_1 = 42.4 + .064 \cos \theta$

	a_1	ϕ_1	a_2	ϕ_2
$x/c = 0.034$	0.858	173.0°	0.053	265.0°
$x/c = 0.169$	0.312	172.4°	0.028	285.8°
$x/c = 0.381$	0.092	188.1°	0.013	248.5°
$x/c = 0.619$		312.8°		
$x/c = 0.831$	0.064	321.0°	0.006	222.7°
$x/c = 0.966$	0.102	206.6°	0.019	117.4°
C_N	0.136	185.3°	0.015	272.9°
C_M	0.057	167.7°	0.004	276.4°
	a_3	ϕ_3	a_4	ϕ_4
$x/c = 0.034$	0.140	150.3°	0.013	125.1°
$x/c = 0.169$	0.021	158.4°	0.008	357.4°
$x/c = 0.381$	0.008	190.0°	0.007	213.1°
$x/c = 0.619$				
$x/c = 0.831$	0.007	250.9°	0.007	216.7°
$x/c = 0.966$	0.011	187.3°	0.009	60.2°
C_N	0.017	183.2°	0.004	248.0°
C_M	0.007	151.7°	0.001	71.5°

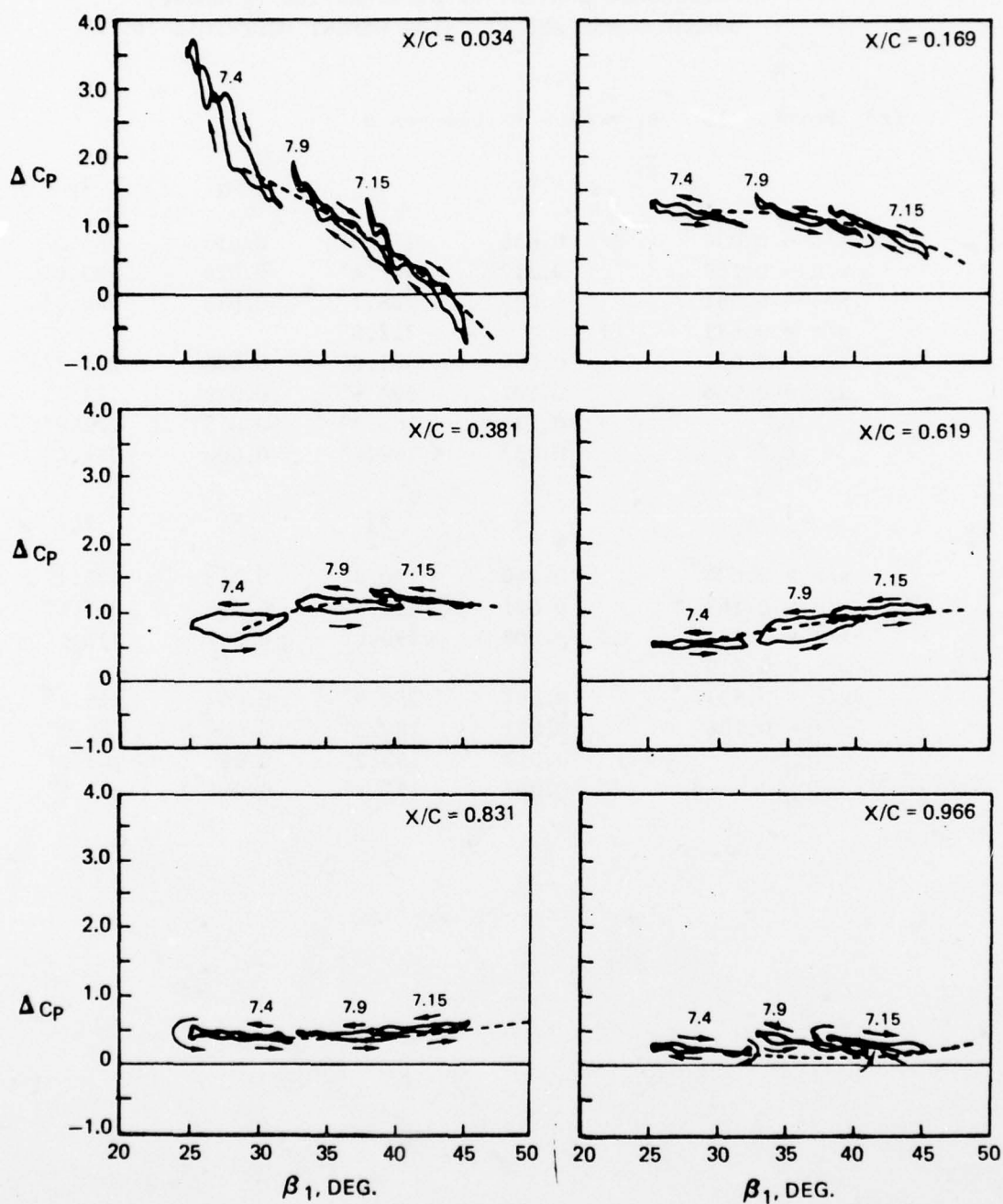


FIG. 24 PRESSURE COEFFICIENT AS A FUNCTION OF INLET ANGLE

studied the response of a cascade to low frequency inlet distortions analytically. Their results show that the magnitude of the unsteady lift coefficient increases with increasing reduced frequency and that the amplification effect exists even at the low reduced frequencies ($k \cong 0.1$) encountered in the present experimental program. Although Horlock, et al., do not calculate the behavior of the surface pressures explicitly, it is reasonable to infer that their variations would also be amplified. Thus, the increased amplitude in the leading edge pressure coefficients is not totally unprecedented. The blade penetrates considerably beyond the steady-state stall point, the left end of the dashed line, resulting in a pressure differential far in excess of that possible in undistorted flow. The phenomenon of stall delay on an isolated airfoil oscillating in pitch is widely recognized (Refs. 31-33). This delay is a strong function of reduced frequency and is normally not so pronounced at the low reduced frequencies encountered in this experiment. Further, this delay is commonly attributed to a decrease in the amplitude of the normal force variation as reduced frequency increases (Refs. 32, 34, and 35). The fact that the amplitude of the response is increased in the present experiment and in the theoretical analysis of Ref. 30 must be attributed to multiblade effects. One manner in which multiblade effects may manifest themselves is in the existence of an interblade phase angle. In the present experiment, the interblade phase angle, σ , was -12.9° .

(This is obtained from a stationary 360° wave divided over 28 blades so that it appears to be a backward-travelling wave.) An experimental investigation in a cascade of airfoils oscillating in pitch (Ref. 36) has shown that the interblade phase angle has a strong influence on the amplitudes and phase angles of the normal force and pitching moment coefficients. It is thus reasonable to suppose that the interblade phase angle present in the inlet distortion experiment is at least partially responsible for the marked departure from the steady state behavior as evidenced by the change in the amplitude of the response and the pronounced stall delay.

The pressure loops exhibit fluctuations which are greater at the lower values of β_1 for each loop. These fluctuations occur at exactly half the screen-segment passing frequency. The screen which produces the distortion is constructed of segments of wire mesh of different porosities. Therefore, the axial velocity variation is not perfectly smooth. This may be thought of as a higher order velocity variation superimposed on the once-per-revolution variation. It thus appears that this higher frequency disturbance is inducing a (relatively) larger response. During the experiment, an overload occurred in the static data system requiring that the average pressure measurements for $x/c = 0.034$ be corrected as described in Appendix VII. No other stations were affected.

At $x/c = 0.169$ the response is much less than at $x/c = 0.034$, although it is still slightly amplified over the undistorted curve. For the high blade loading of point 7.4, the response leads the input. For point 7.9, the response leads at the higher instantaneous inlet angles and lags at the lower angles. For the lowest blade loading, point 7.15, the response lags the inlet angle over most of the cycle. The phase angle of the pressure response relative to the inlet angle thus decreases as the inlet angle increases.

At $x/c = 0.381$ the loop representing point 7.4 is more open than the other two. This is because the first harmonic amplitude is greater for this point and the phase angle is quite near 270° . (Phase angles of 90 or 270 degrees will produce the most open loops.) As with $x/c = 0.169$, the phase angle consistently decreases as the average inlet angle increases. The loops have all become considerably smoother, perhaps indicating that the fluctuations appearing at the leading edge have been damped out by the presence of the neighboring blades.

All the loops for $x/c = 0.619$ are counterclock-wise, with the loop for point 7.9 being more open. The phase angle of the pressure response does not decrease with increasing inlet angle as was previously observed; instead, it remains relatively constant. The pressure fluctuations first observed at the leading edge have been further reduced in amplitude. The loops for $x/c = 0.831$ and $x/c = 0.966$ show

very little activity. The undistorted characteristic is very nearly horizontal in both cases indicating that the pressure coefficients at these stations are essentially independent of inlet angle. The pressure coefficient difference appears to be approaching zero at the trailing edge.

The variations in the amplitude of these responses were well illustrated by Fig. 24; however, the phase angle variations are not so obvious. The phase angle is a strong indicator of unsteadiness, perhaps more so than is amplitude. (See, for example, Ref. 34 or Ref. 35.) The phase angle of the differential pressure coefficients and the integrated normal force and pitching moment coefficients are presented in Table III. The phase angles for the two forward measuring stations and for the normal force and pitching moment are shown as a function of the mean inlet angle in Fig. 25. Because the reference is to the inlet angle, β_1 , rather than to an incidence angle, quasi-steady behavior would be indicated by a phase angle of 180° rather than 0° as is normally the case. The phase angle is seen to vary smoothly with the mean inlet angle indicating that the unsteadiness of the response is a strong function of blade loading.

To complete the discussion of blade pressures, we will now consider the pressure distribution across the chord of the blades. This is simply another method of presenting the pressure data to emphasize the way in which the pressures at different positions on

TABLE III

FIRST HARMONIC PHASE ANGLES OF THE
DIFFERENTIAL PRESSURES, NORMAL FORCE, AND PITCHING MOMENT

Chordwise Station	β_1					
	28.9	33.5	36.9	40.4	42.2	45.2
0.034	172°	177°	174°	175°	173°	172°
0.169	197°	188°	181°	178°	172°	169°
0.381	285°	282°	252°	219°	188°	173°
0.619	262°	319°	317°	316°	313°	319°
0.831	164°	162°	272°	306°	321°	330°
0.966	222°	172°	174°	191°	207°	220°
C_N	201°	199°	208°	204°	185°	168°
C_M	179°	185°	172°	169°	168°	166°

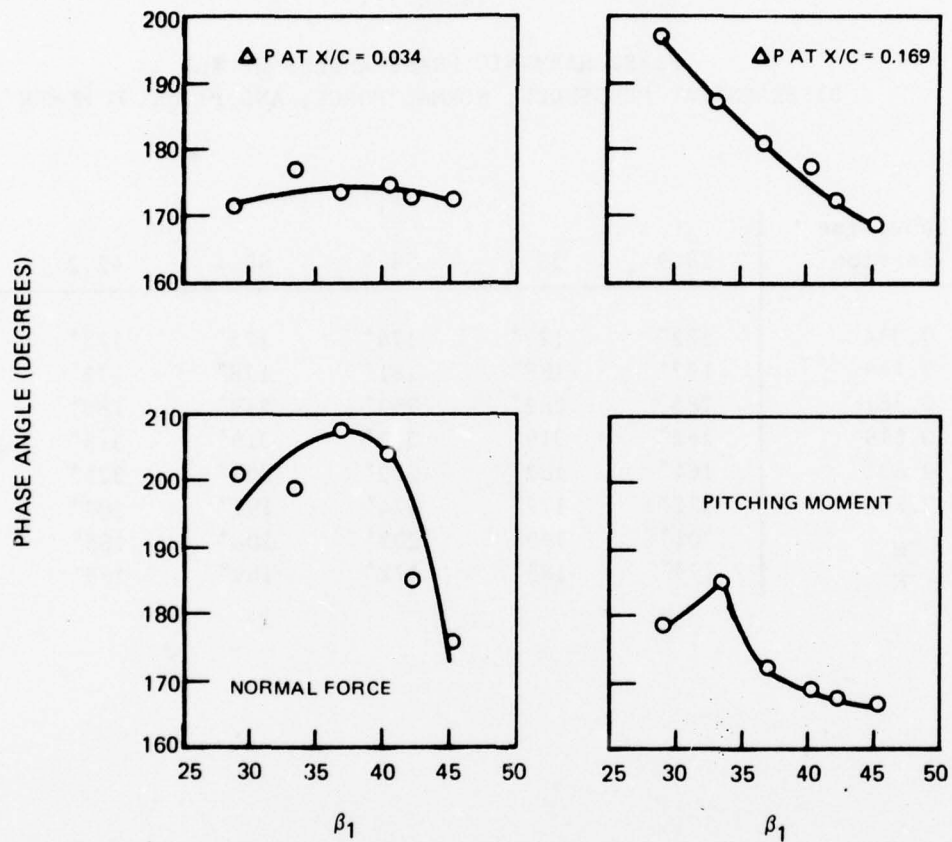


FIG. 25 PRESSURE, FORCE, AND MOMENT PHASE ANGLE AS A FUNCTION OF AVERAGE INLET ANGLE

the blade relate to one another at a given inlet angle. Four inlet angles will be considered for each flow condition. These will be the minimum inlet angle ($\theta = 180^\circ$), the mean inlet angle with the inlet angle increasing ($\theta = 270^\circ$), the maximum inlet angle ($\theta = 0^\circ$), and the mean inlet angle with the inlet angle decreasing. The pressure coefficient distributions for the suction surface (denoted by an S) and the pressure surface (denoted by a P) are presented for the three representative flow conditions in Figs. 26 through 28, respectively. Although the distribution of measuring stations gives adequate accuracy in the integration to obtain normal force and pitching moment coefficients, it is not sufficiently dense near the leading edge to define the shape of the pressure profile at the leading edge. In particular, it is not possible to resolve the location or magnitude of the leading edge suction peak under high load.

It must be remembered that decreasing inlet angle corresponds to increasing blade incidence. Figure 26 for point 7.4 shows a relatively sharp peaking of the leading edge suction (although the exact value of the peak and its precise location cannot be determined) which is most pronounced at the minimum instantaneous inlet angle (maximum incidence). The peak is in evidence, although not as strong, for all inlet angles at this flow condition. As the mean inlet angle is increased to the flow condition of point 7.9 (Fig. 27), this peaking is lessened. In fact, the peak at the extreme

(P DENOTES PRESSURE SURFACE, S DENOTES SUCTION SURFACE)

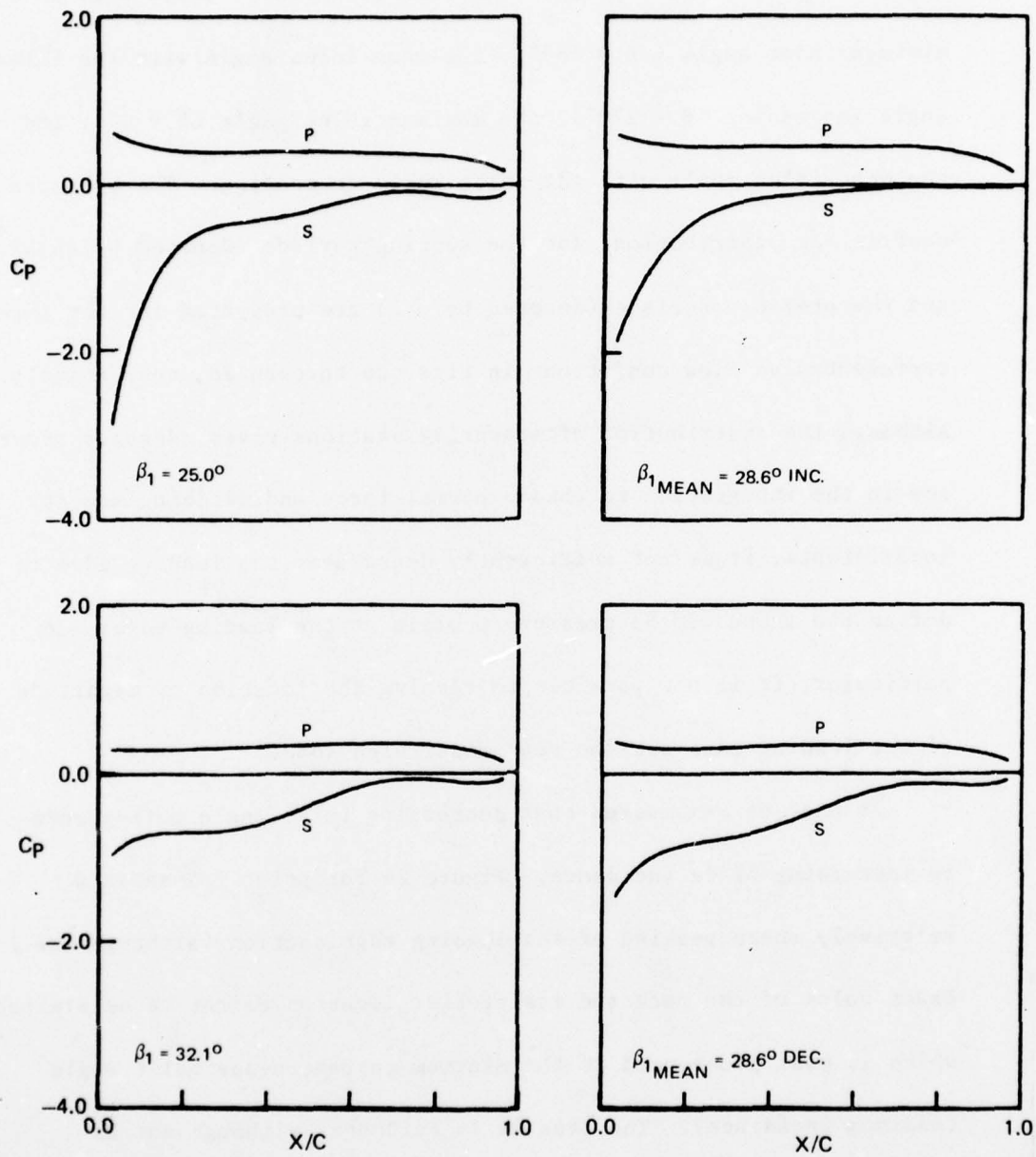


FIG. 26 PRESSURE COEFFICIENT DISTRIBUTIONS FOR POINT 7.4

(P DENOTES PRESSURE SURFACE, S DENOTES SUCTION SURFACE)

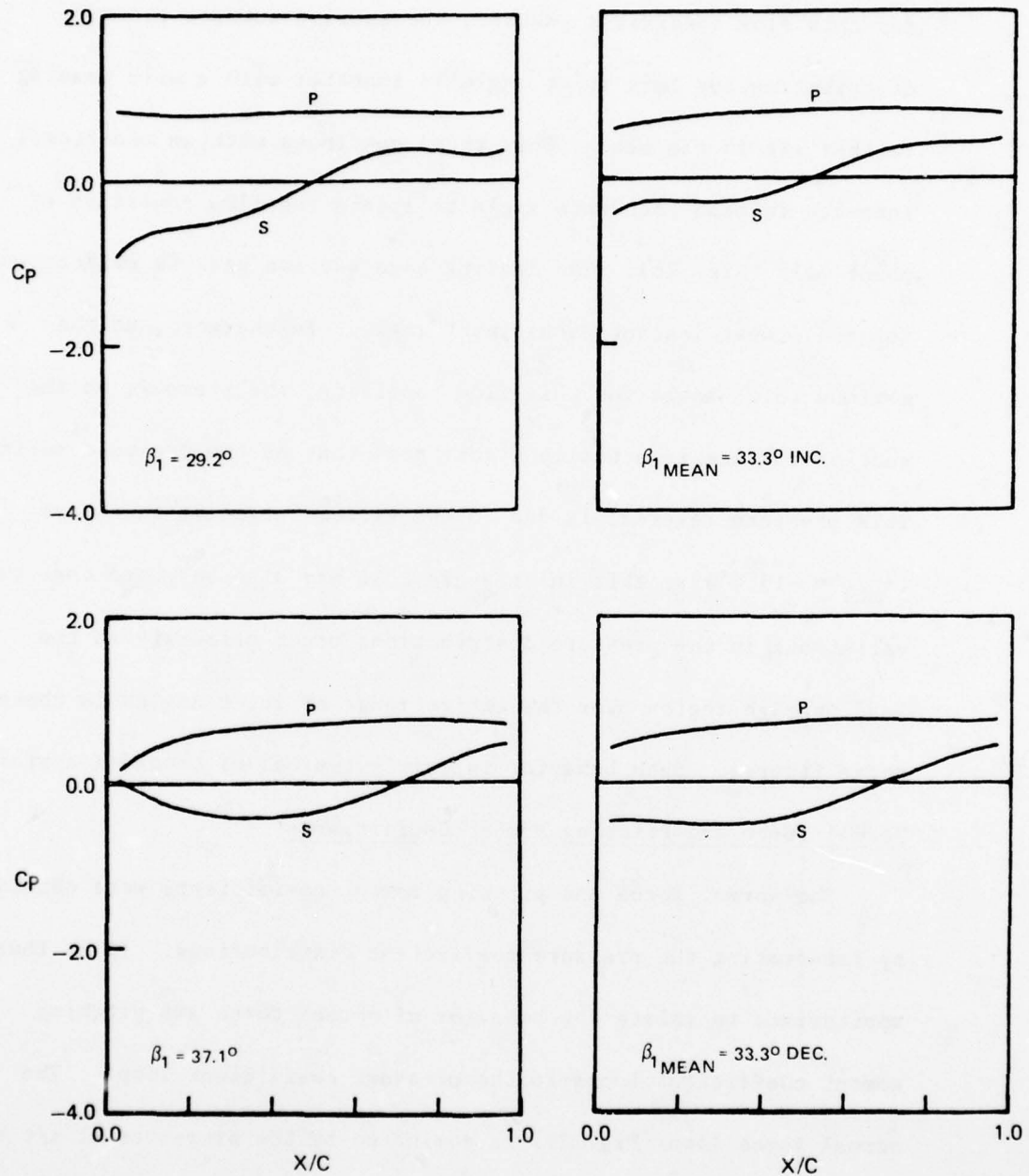


FIG. 27 PRESSURE COEFFICIENT DISTRIBUTIONS FOR POINT 7.9

leading edge is not present at the maximum instantaneous inlet angle for this flow condition. Rather, the suction surface pressure distribution for this inlet angle is smoother with a mild peaking farther aft on the blade. This trend continues with an additional increase in mean incidence angle to attain the flow condition of point 7.15 (Fig. 28). The leading edge suction peak is evident only for the lowest instantaneous inlet angle. Furthermore, at the maximum inlet angle for this flow condition, the pressure on the suction surface is actually higher than that on the pressure surface. This pressure reversal is due to the extreme negative incidence ($\alpha_{mcl} = -15.4^\circ$) at this inlet angle. It may also be noted that the variations in the pressure distributions occur primarily in the leading edge region over the entire range of inlet angles in these three figures. Such behavior is fairly typical of cascaded airfoils.

Normal Force and Pitching Moment Coefficients

The normal force and pitching moment coefficients were obtained by integrating the pressure coefficient distributions. It is thus appropriate to relate the behavior of normal force and pitching moment coefficient loops to the pressure coefficient loops. The normal force loop (Fig. 29) is dominated by the pressures at $x/c = 0.381$ and $x/c = 0.619$ because these two stations have the highest weighting coefficients in the Gaussian integration scheme. (See Eq. 9 and Table I). Since all three pressure loops at both of these

(P DENOTES PRESSURE SURFACE, S DENOTES SUCTION SURFACE)

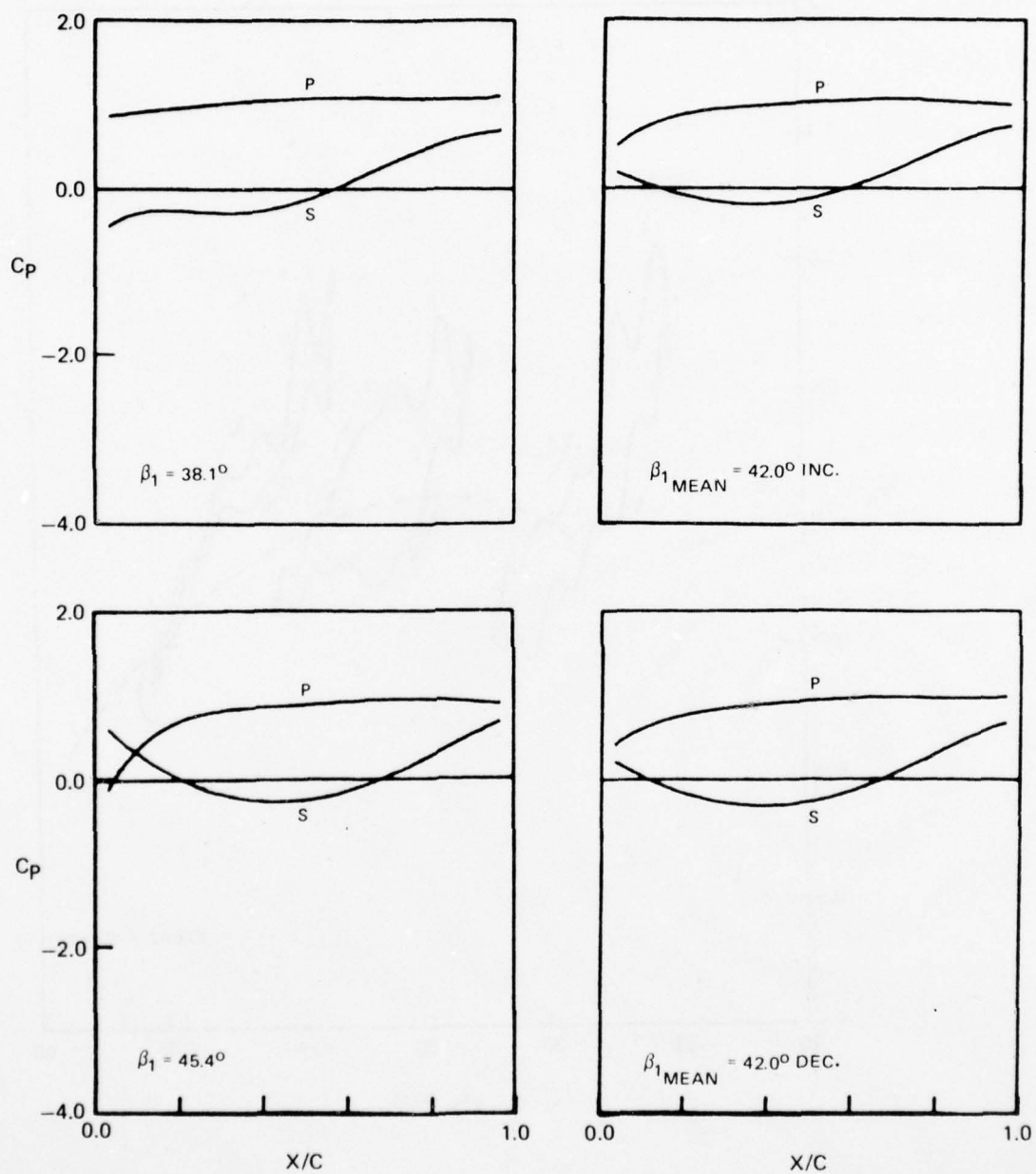


FIG. 28 PRESSURE COEFFICIENT DISTRIBUTIONS FOR POINT 7.15

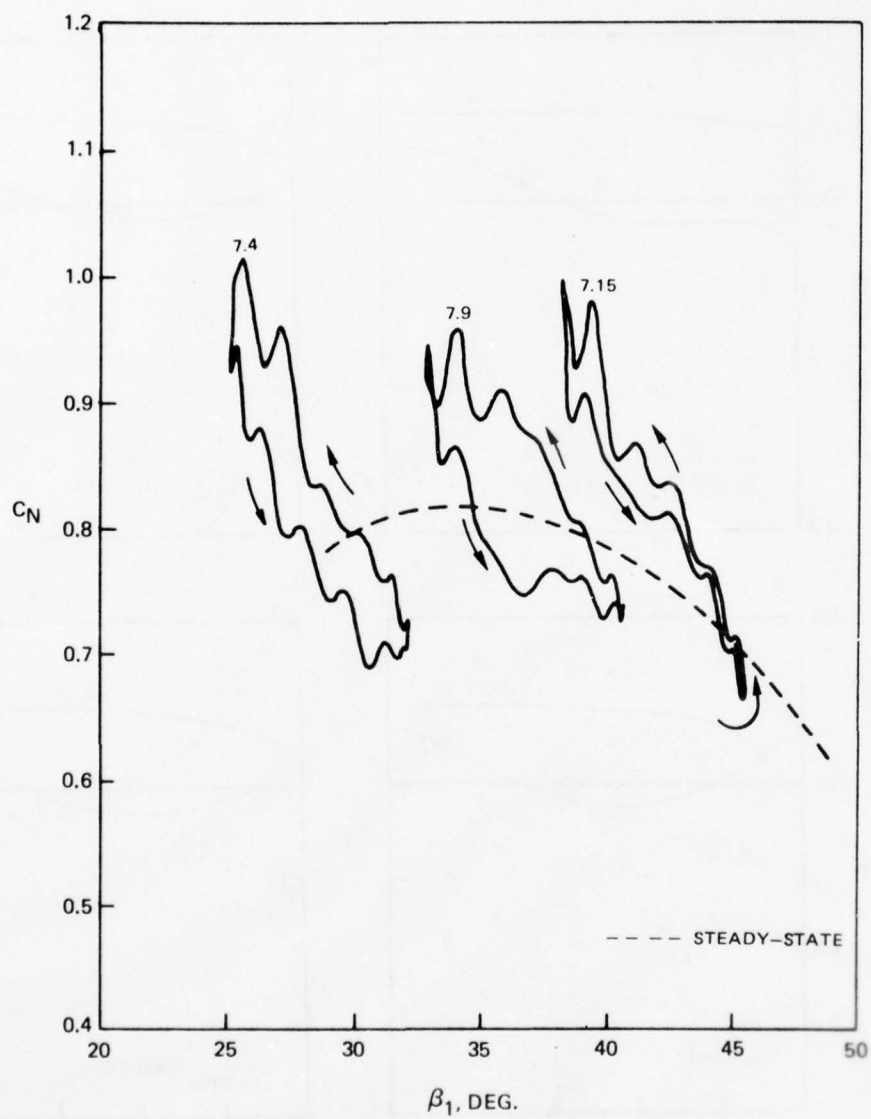


FIG. 29 NORMAL FORCE COEFFICIENT AS A FUNCTION OF INLET ANGLE

AD-A064 776

NORTH CAROLINA STATE UNIV RALEIGH ENGINEERING DESIGN--ETC F/6 21/5
AN EXPERIMENTAL STUDY OF THE RESPONSE OF A TURBO-MACHINE ROTOR --ETC(U)
DEC 78 L HARDIN F44620-76-C-0055

UNCLASSIFIED

NCSU/EDC-78-6

AFOSR-TR-79-0073

NL

2 of 2
AD
A064776



END
DATE
FILMED
4-79
DDC

stations are counterclockwise (see Fig. 24), it is not surprising that the normal force loops are also counterclockwise. Even the fact that the loop for point 7.5 is almost completely collapsed on itself can be traced directly to these pressure loops. At first, it appears that the normal force loops lie further above the quasi-steady curve than would be expected from the pressure loops. This illusion is due to the expanded scale used to plot the normal force loops. The large fluctuations observed in the pressure loops for the leading edge stations are present and have also been magnified by the scale change. Perhaps the most interesting point is that the maximum normal force coefficient in the distorted flow is roughly 25% greater than the maximum quasi-steady value and is due in part to the excursion past the steady-state stall point. Of course, the variation in actual load is not nearly so great since this high normal force coefficient occurs in the low velocity region of the distortion.

The pitching moment loop (Fig. 30) is virtually identical to the pressure loop at $x/c = 0.034$. Although the stations at $x/c = 0.0381$ and $x/c = 0.619$ have the highest weighting coefficients, they are located symmetrically about the moment center (mid-chord) and effectively cancel each other. (See Eq. 10 and Table I.) The pitching moment is thus dominated by the strong leading edge response. The loops are all basically clockwise, indicating that the pitching moment lags the inlet angle, and becomes more open as the average

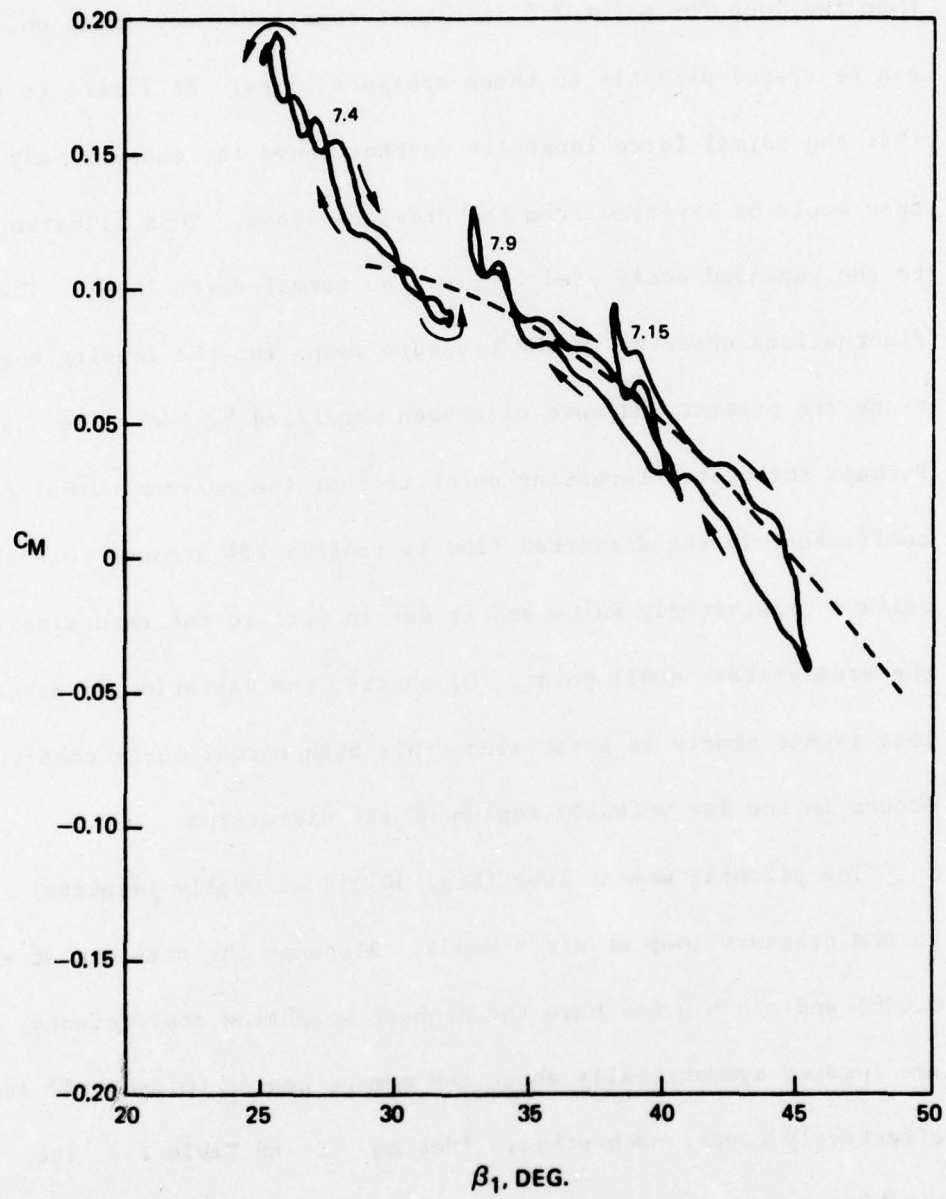


FIG. 30 PITCHING MOMENT COEFFICIENT AS A FUNCTION OF INLET ANGLE

inlet angle increases, indicating a greater lag for the lighter blade loading. This behavior was also evident in Fig. 25.

Comparison to Cascade Data

The aerodynamics of a rotor undergoing inlet distortion and a cascade oscillating in pitch are not identical. However, if one compares the phase plane diagrams of the Sears function for a convected sinusoidal gust (Ref. 34) and the Theodorsen function for a sinusoidally oscillating airfoil (Ref. 35), it is apparent that the convected gust problem and the oscillating airfoil problem do have similar solutions at low reduced frequencies. It is thus logical to expect the cascade tests of Ref. 36 to reproduce the basic trends observed in the inlet distortion experiment. This is indeed the case. The peaking of the suction near the leading edge and the concentration of the pressure variations near the leading edge observed in the present experiment are duplicated in the cascade experiment. At an equivalent reduced frequency and zero interblade phase angle, the normal force coefficient for the cascade generally leads the angle of attack. The pitching moment coefficient lags the angle of attack, although the amount of lag decreases as the blade loading increases. These trends are consistent with those observed in the present experimental study of the inlet distortion problem. The similarities exist despite the differences in blade profiles. (Although the blades in the cascade test have a similar thickness

distribution, they have only 10° of camber as opposed to 50° for the LSRR blades.) This is a strong indication that cascading effects far outweigh blade profile effects.

Transient Surface Flow Phenomena

Hot-film skin friction gages were mounted adjacent to the pressure transducers to detect surface flow phenomena such as separation and transition to turbulent flow. The interpretation of the skin friction coefficient derived from these measurements is impossible without some reference point. This reference point may take the form of a known flow condition at some point in time or may be based on the results from a pressure transducer near the skin friction gage or even the behavior of skin friction and/or pressure at some other point on the blade. For example, if the flow is known to be attached and laminar at some point in time and the skin friction coefficient subsequently increases and shows high frequency fluctuations, transition to turbulent flow is indicated. Conversely, if the skin friction drops abruptly and shows these fluctuations, separation of the boundary layer may be inferred. If the flow does separate, it may reattach downstream. If it does so, the flow downstream of the reattachment point must be turbulent and will be characterized by high frequency variations in the skin friction coefficient and a generally higher average value.

Most of the activity in the pressure coefficient and skin friction time histories is confined to the leading edge region; therefore, in this discussion the pressure coefficients for only the first two measuring stations will be considered, and only suction surface data are presented. Decreasing pressure coefficient indicates increasing normal force. Only the time-varying part of the signals are plotted. Figures 31 through 33 present the data from points 7.4, 7.9, and 7.15 respectively. Figure 31 represents the lowest average inlet angle tested. This results in the highest blade loading and results in separated flow during part of the cycle. First consider the skin friction trace for $x/c = 0.034$. At the point marked A, the flow is attached and probably laminar. The relatively rapid increase near point B may be taken to indicate transition to turbulent flow followed almost immediately by separation. Separation occurs slightly before minimum inlet angle. (Recall that minimum β_1 is associated with maximum load.) As the inlet angle increases from the minimum value, the flow reattaches (point C) and the cycle repeats itself. It is interesting to note that the separation pattern is different for each cycle plotted. For the first occurrence of separation at the extreme left-hand side of the figure, the flow at $x/c = 0.034$ is separated over a greater range of inlet angles than the second occurrence. The third time the flow separates (point D) it does not appear to reattach after minimum inlet angle has been passed. The

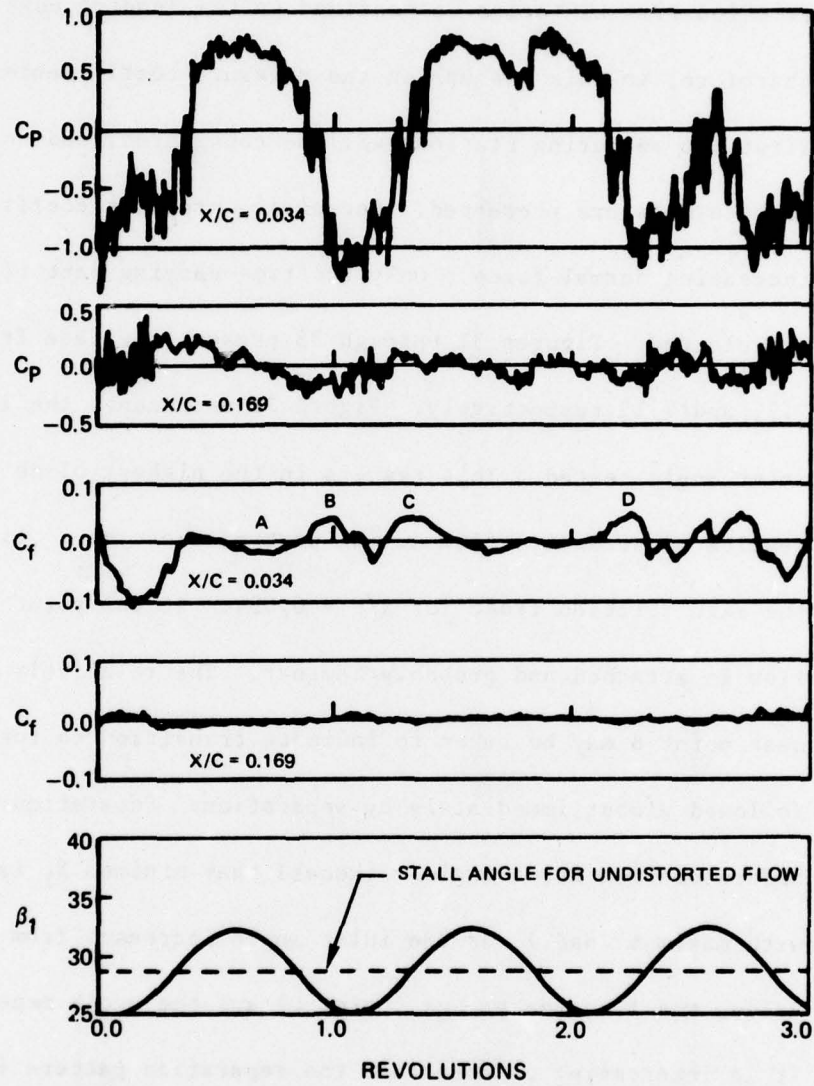


FIG. 31 PRESSURE AND SKIN FRICTION TIME HISTORIES FOR POINT 7.4

pressure transducer at this chordwise station does not show a significant decrease in suction during the time the flow is separated, but it does indicate an increase in the magnitude of the pressure fluctuations. The lack of a sharp drop in leading edge suction may be taken to indicate that the blade has made only a shallow penetration of the dynamic stall regime. That is, although the surface flow has become separated, the external potential flow is relatively unchanged. In steady flow, the blade stalls at an inlet angle of 28.5 degrees. Since the inlet angle in distortion drops as low as 25° it is evident that the blade has gone past the quasi-steady stall point by a significant amount. Very little boundary layer activity is indicated by the skin friction gage at $x/c = 0.169$. During the time that the flow at $x/c = 0.034$ is separated, there is slight increase in the average level of the signal and in the amplitude of the high frequency fluctuations. This may be due to the reattachment of the flow between $x/c = 0.034$ and $x/c = 0.169$. The flow downstream of a reattachment point is expected to be turbulent, and since there is no indication of transition, the flow must always be turbulent at this stations. The pressure transducer trace at $x/c = 0.169$ also exhibits an increase in the high frequency fluctuations. Taken together, all of these readings indicate that a separation bubble probably forms on the leading edge as the inlet angle approaches a minimum and grows until the minimum angle has been passed whereupon it shrinks and then

vanishes. During the experiment it was found that this flow condition results in the lowest average inlet angle that can be attained without inducing rotating stall. Thus, in the case of inlet distortion, the onset of rotating stall appears to be triggered by the occurrence of dynamic stall in the low velocity region of the distortion.

The flow condition for point 7.9 is such that separation does not occur. The variations in the skin friction trace for $x/c = 0.034$ shown in Fig. 32 are due to transition between laminar and turbulent flow. The regions of higher skin friction correspond to times during which the transition point is ahead of that station and the regions of lower skin friction correspond to times during which the transition point is behind it. When the flow is turbulent at $x/c = 0.034$, it must also be turbulent at $x/c = 0.169$. Since there is no indication of transition at $x/c = 0.169$, the flow must always be turbulent there. Thus, the transition point must always lie ahead of $x/c = 0.169$. At the lower values of instantaneous inlet angle, the transition point is ahead of $x/c = 0.034$. The data obtained from point 7.15 are shown in Fig. 33. The small humps in the skin friction trace for $x/c = 0.034$ indicate transition to turbulent flow only at the minimum inlet angle. By the same reasoning as before, the flow at $x/c = 0.169$ must always be turbulent.

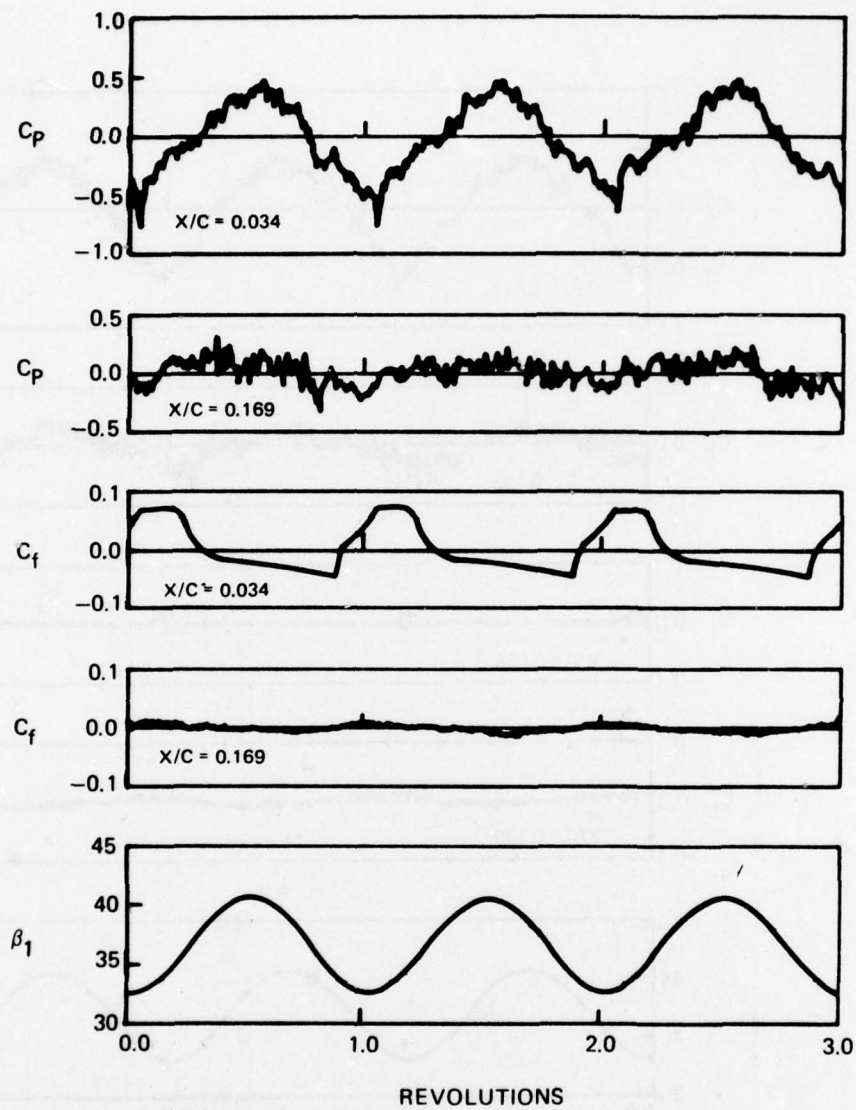


FIG. 32 PRESSURE AND SKIN FRICTION TIME HISTORIES FOR POINT 7.9

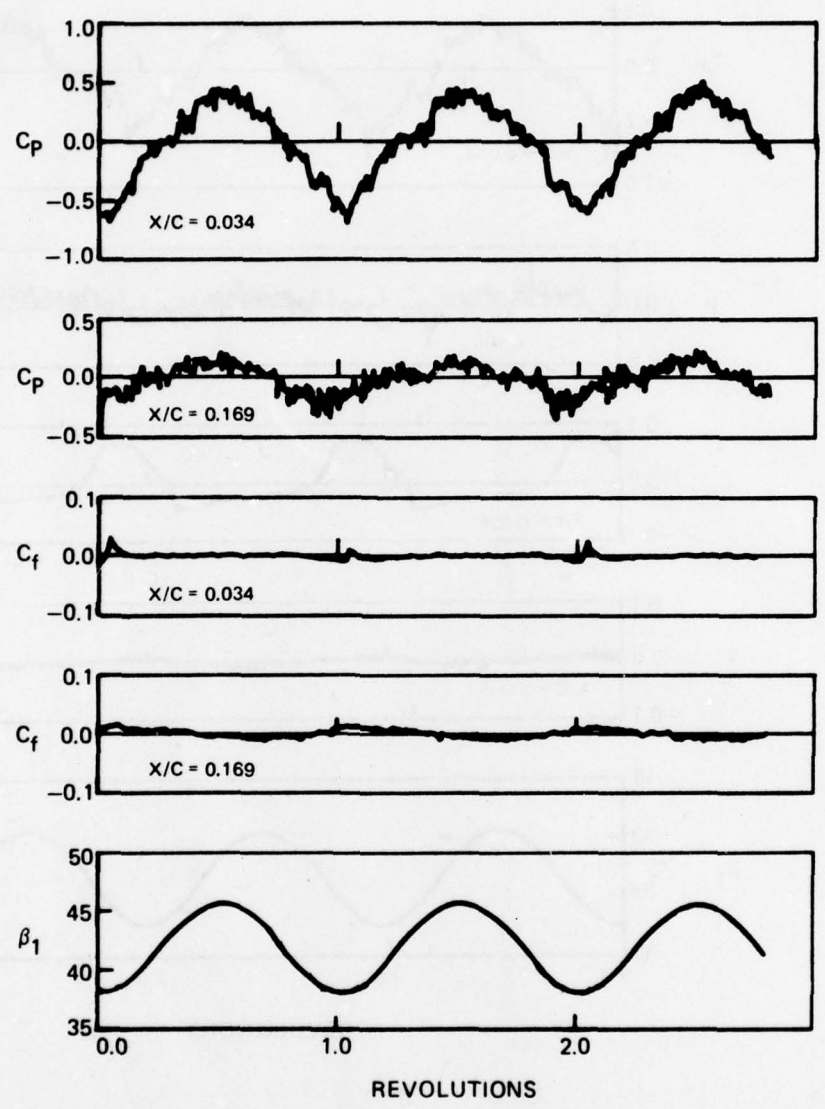


FIG. 33 PRESSURE AND SKIN FRICTION TIME HISTORIES FOR POINT 7.15

Unsteady Rotor Pressure Rise

As previously mentioned, the rotor in a distorted flow does not operate at one single inlet angle and pressure rise coefficient. Instead, the inlet angle and pressure rise coefficient vary around the circumference. The downstream static pressures were Fourier analyzed to smooth the data and the pressure rise coefficient was computed as a function of position in the distortion field. Plotting the pressure rise as a function of the instantaneous inlet angle produces the loops of Fig. 34.

These loops are for points 7.4, 7.9, and 7.15 and are similar in nature to the loops which were previously derived for the blade pressure, normal force and pitching moment coefficients. The loop for the highest average inlet angle shows good agreement with the undistorted characteristic and that the distorted pressure rise lags the inlet angle. The other two loops are much more open indicating a greater phase shift, and depart significantly from the undistorted characteristic. The sense of the loops at the lower inlet angles indicates that the pressure rise leads the inlet angle while the one at the high inlet angle indicates a lagging response. Referring to Table IV, one finds that the first harmonic of the pressure rise loop for point 7.4 does indeed lead the inlet angle as does that for point 7.9, although to a lesser degree. The first harmonic of the loop for point 7.15 shows a slight lag. This same trend was observed for the

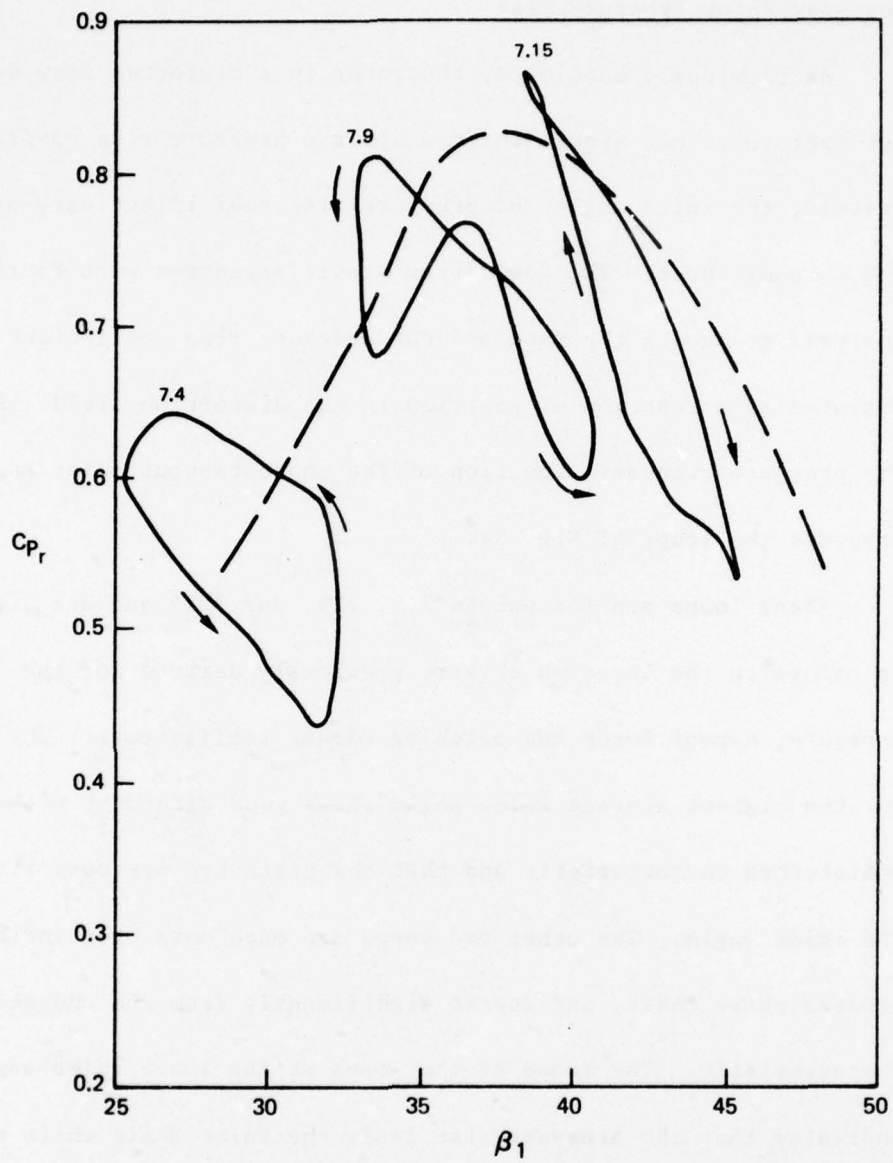


FIG. 34 UNSTEADY ROTOR PRESSURE RISE AS A FUNCTION OF INLET ANGLE

TABLE IV
HARMONIC CONTENT OF UNSTEADY ROTOR PRESSURE RISE COEFFICIENT

	a_0	a_1	ϕ_1	a_2	ϕ_2
Point 7.4	0.433	0.089	37.1	0.013	70.9
Point 7.9	0.459	0.090	11.9	0.017	335.6
Point 7.15	0.393	0.138	350.5	0.010	17.0
		a_3	ϕ_3	a_4	ϕ_4
Point 7.4		0.009	115.5	0.005	71.0
Point 7.9		0.025	98.1	0.012	40.1
Point 7.15		0.011	83.1	0.003	25.6

Note: Coefficients are for the form $C_{p_r} = a_0 + \sum a_n \cos(n\theta + \phi_n)$

pressure, normal force, and pitching moment coefficient loops. There is moderate second harmonic content in the loops for points 7.4 and 7.9. However, the loop for point 7.15, which is in the potential flow regime and also in the low loss region, is almost a pure first harmonic.

Velocities and Flow Angles at the Rotor Exit Plane

Three velocity components were measured approximately 0.07 chord lengths aft of the rotor exit plane using a triaxial hot-film probe. The parameters which will be employed to present the results of these measurements will be the exit velocity, W_2 , the circumferential flow angle, β_2 , and the radial flow angle, ψ . We will first consider measurements made in undistorted flow at an inlet angle of 42.3° . The variation in the exit velocity across the blade gap is plotted in Fig. 35. The point $y/g = 0.0$ corresponds to the downstream projection of the suction surface of one blade and $y/g = 1.0$ corresponds to the downstream projection of the pressure surface of its neighbor. The velocity profile is relatively flat showing a slight decrease as one approaches the pressure surface ($y/g = 1.0$). There is an abrupt drop in velocity near the blade trailing edges at $y/g = 0.0$ and $y/g = 1.0$. It must be pointed out that the sensor arrangement of this particular probe is such that it is not suitable for use in regions where strong velocity gradients exist. The blade wakes are obviously such regions; however, the exit velocity should be only

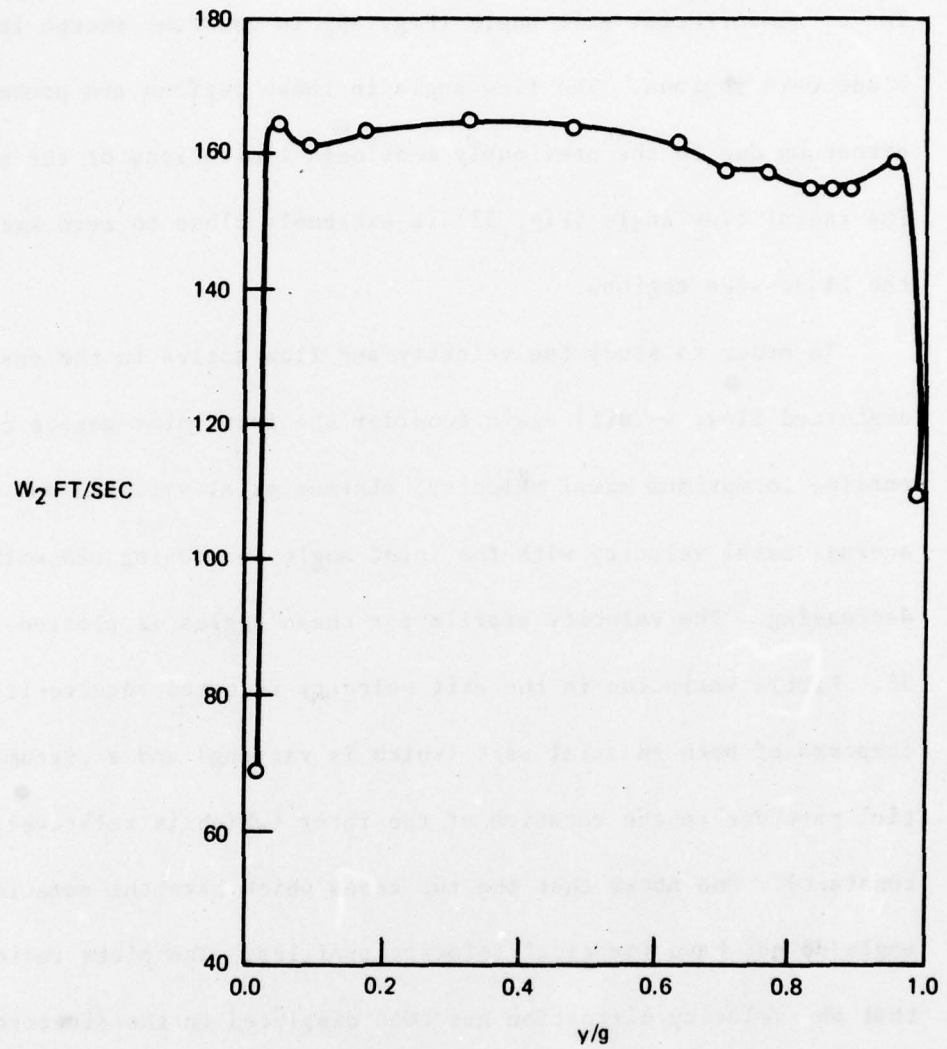


FIG. 35 VELOCITY AT ROTOR EXIT PLANE AS A FUNCTION OF GAPWISE POSITION IN UNDISTORTED FLOW

slightly affected. The radial flow angle will be affected somewhat more and the circumferential flow angle will be strongly affected. The circumferential exit angle (Fig. 36) is constant except in the blade wake regions. The flow angle in these regions are probably erroneous due to the previously mentioned limitations of the probe. The radial flow angle (Fig. 37) is extremely close to zero except in the blade wake regions.

In order to study the velocity and flow angles in the case of distorted flow, we will again consider the four inlet angles corresponding to maximum axial velocity, minimum axial velocity and the average axial velocity with the inlet angle increasing and with it decreasing. The velocity profile for these angles is plotted in Fig. 38. Little variation in the exit velocity is noted because it is composed of both an axial part (which is varying) and a circumferential part due to the rotation of the rotor (which is relatively constant). One notes that the two cases which have the same inlet angle do not have identical velocity profiles. The plots indicate that the velocity distortion has been displaced in the direction of rotation of the rotor. The variation in β_2 across the gap is shown in Fig. 39. This profile is relatively flat except for an inlet angle of 43.8° with the inlet angle decreasing. In this case, the exit angle exhibits rather pronounced fluctuations for which there is presently no explanation. It is apparent that the gap-averaged

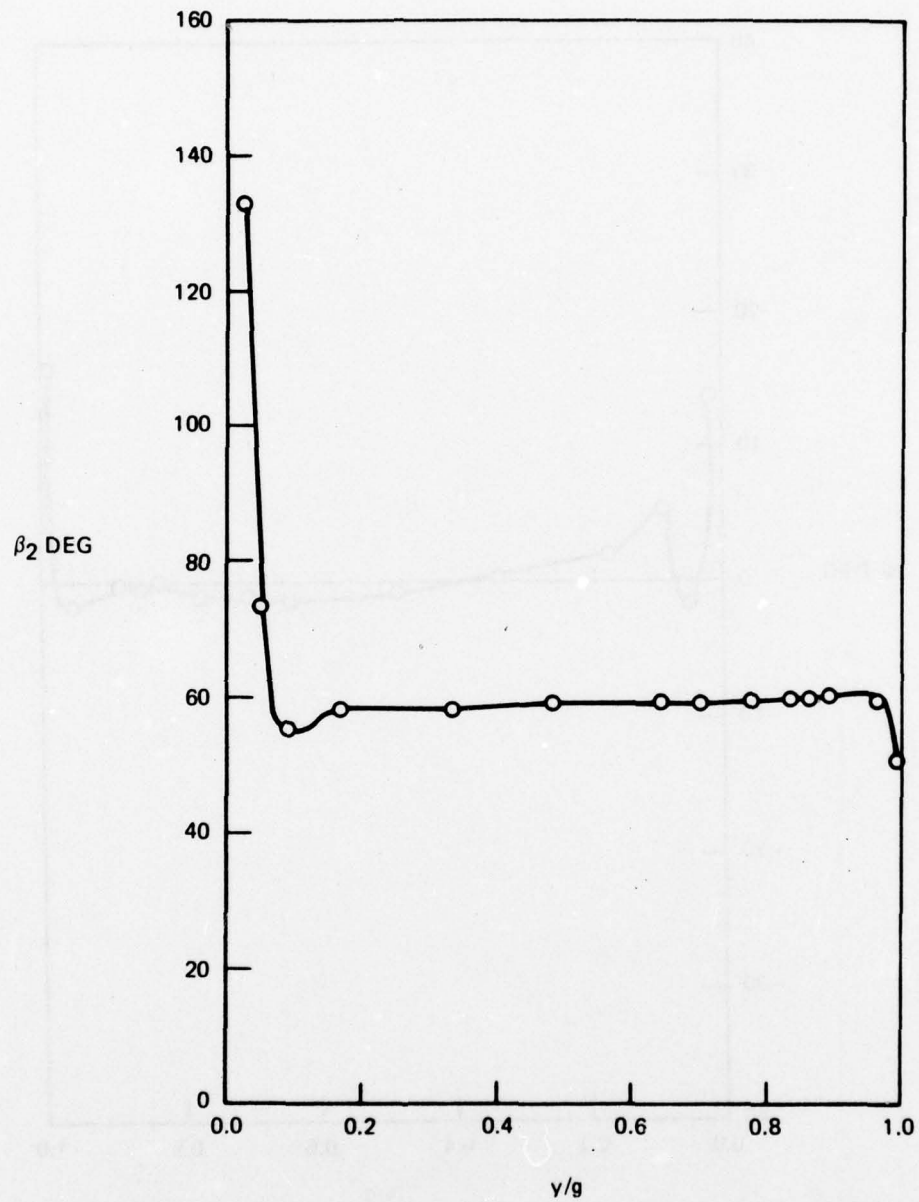


FIG. 36 CIRCUMFERENTIAL FLOW ANGLE OF EXIT PLANE AS A FUNCTION OF GAPWISE POSITION IN UNDISTORTED FLOW

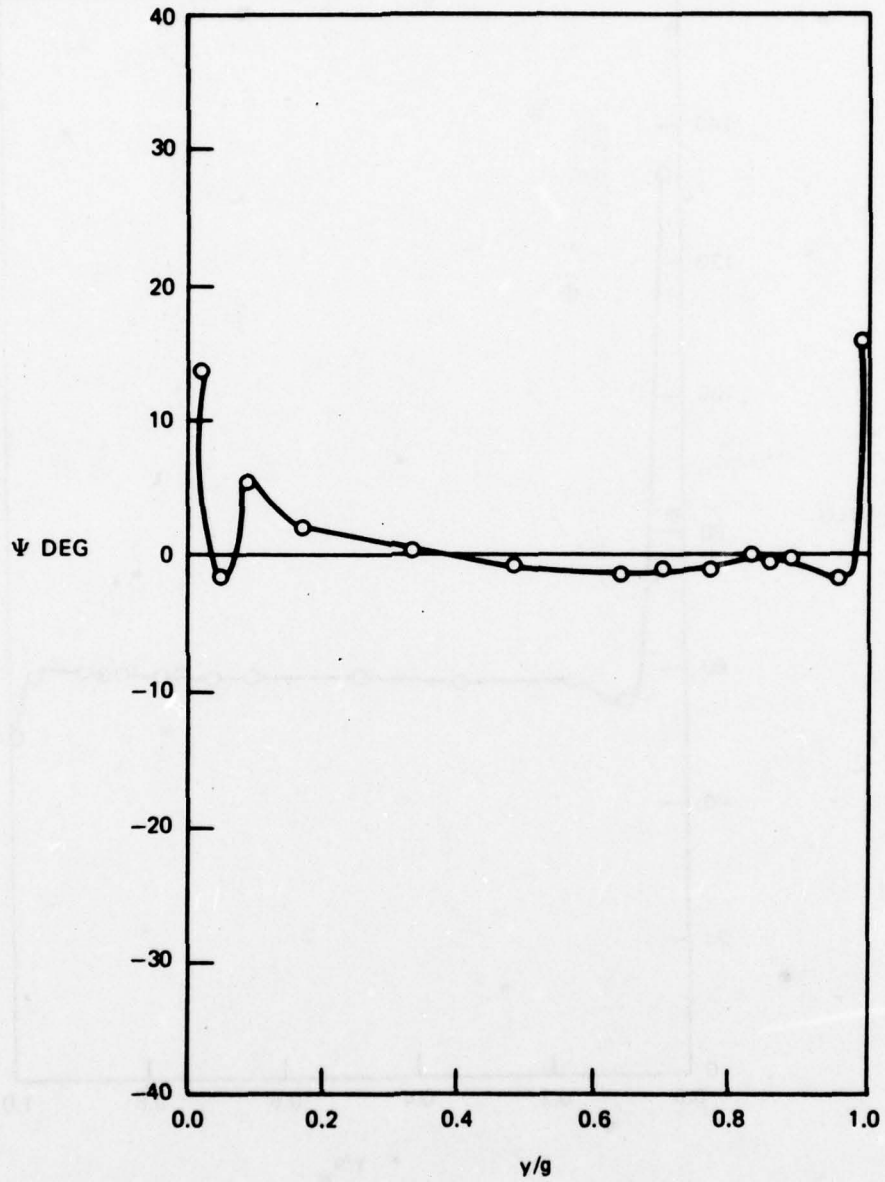


FIG. 37 RADIAL FLOW ANGLE AT EXIT PLANE AS A FUNCTION OF GAPWISE POSITION IN UNDISTORTED FLOW

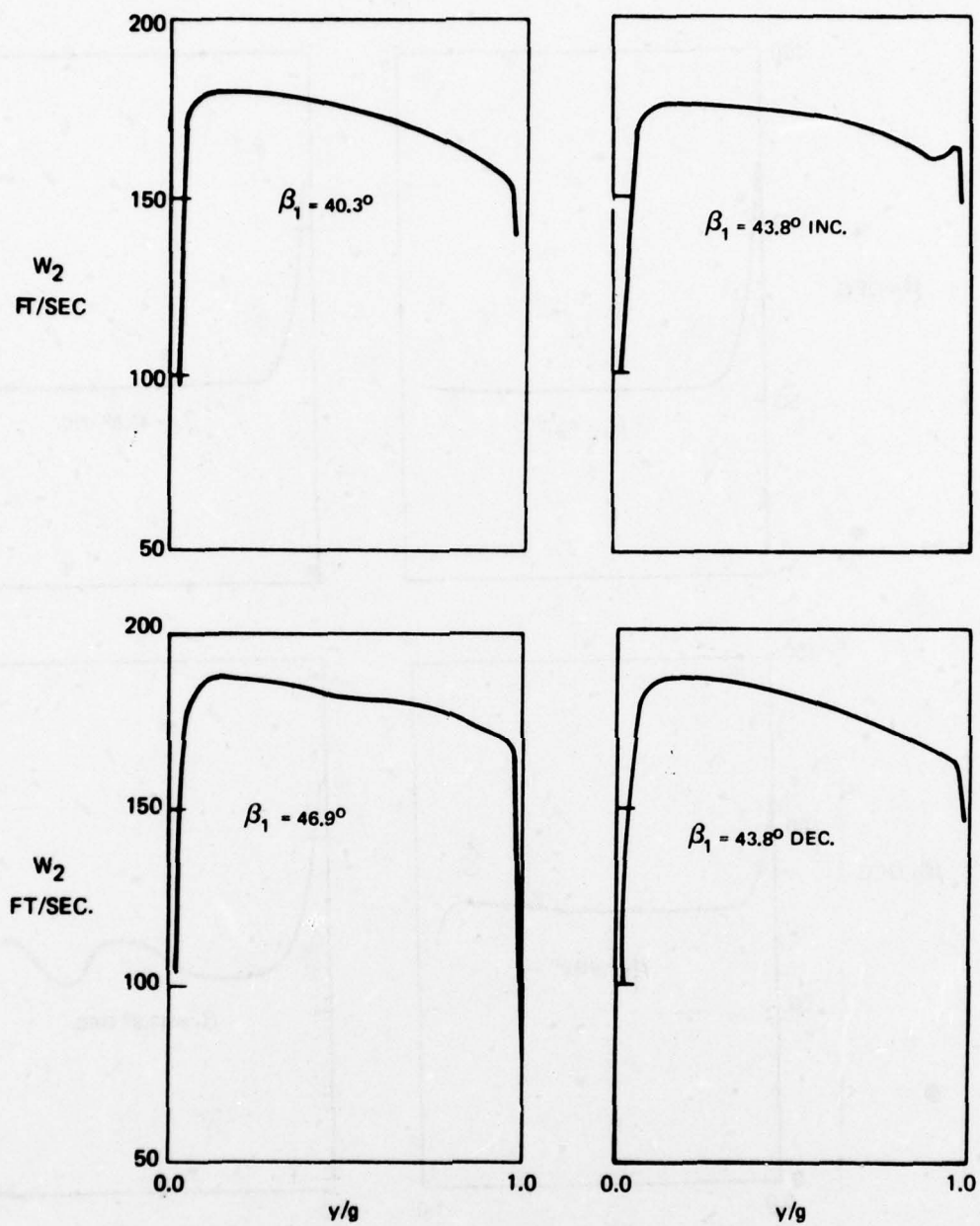


FIG. 38 VELOCITY AT ROTOR EXIT PLANE AS A FUNCTION OF GAPWISE POSITION IN DISTORTED FLOW

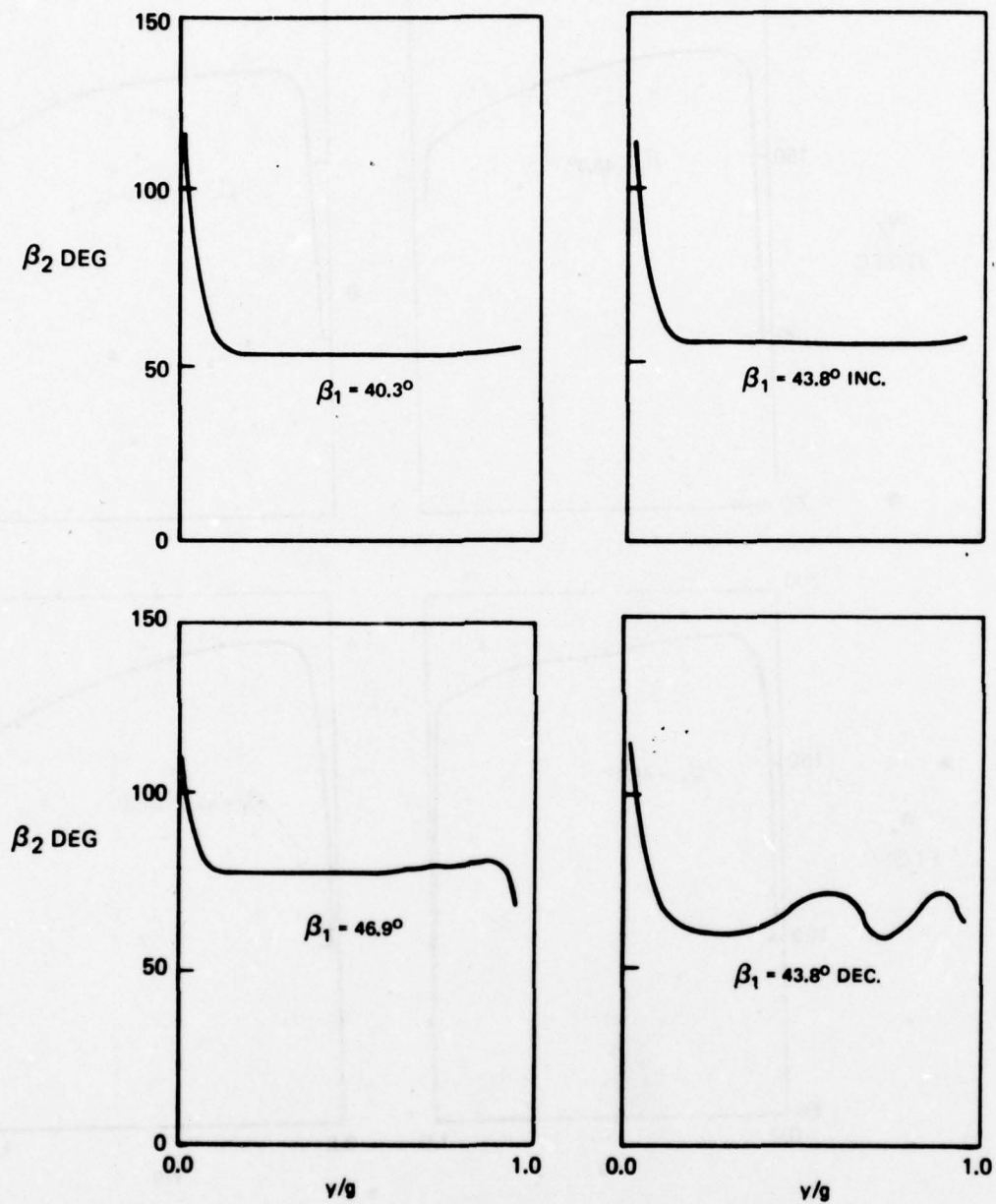


FIG. 39 CIRCUMFERENTIAL FLOW ANGLE AT ROTOR EXIT PLANE AS A FUNCTION OF GAPWISE POSITION IN DISTORTED FLOW

circumferential exit angle is undergoing significant changes as the distortion is traversed. By obtaining gap-averaged values of the exit angle at these and several additional locations in the distortion field and plotting them as a function of the instantaneous inlet angle (Fig. 40) one generates a loop similar to those produced from the pressure data. Comparing this loop to the undistorted exit angle behavior, one concludes that the unsteady exit angle is lagging the steady curve. The shape of the loop, however, is a very poor match to the shape of the steady state curve. Furthermore, the variations in exit angle measured by the probe appear to be excessive. Exit angles were also calculated by a momentum theory approach (similar to that of Appendix V) neglecting any unsteady effects not inherent in the normal force and rotor pressure rise loops. The results of these calculations (which are not presented here) tend to support the belief that the indicated exit angle variations in distorted flow are excessive. The radial flow angle (Fig. 41) is definitely not zero indicating that the distorted flow field has induced three-dimensional effects into the rotor wake. The lack of agreement between the exit angle, β_2 , measured in distorted flow and that in uniform inlet flow may be partly due to these three-dimensional effects.

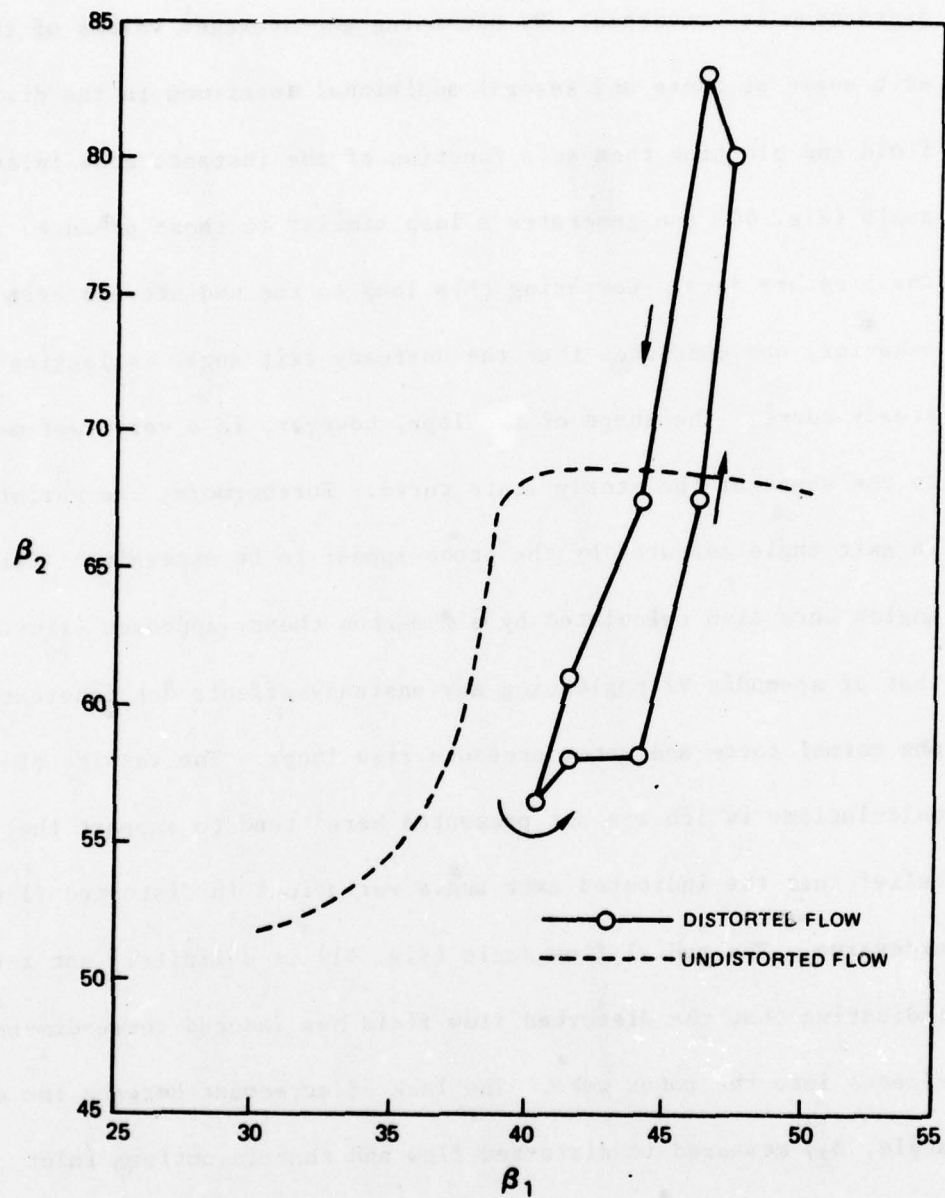


FIG. 40 GAP AVERAGED CIRCUMFERENTIAL EXIT ANGLE AS A FUNCTION OF INLET ANGLE

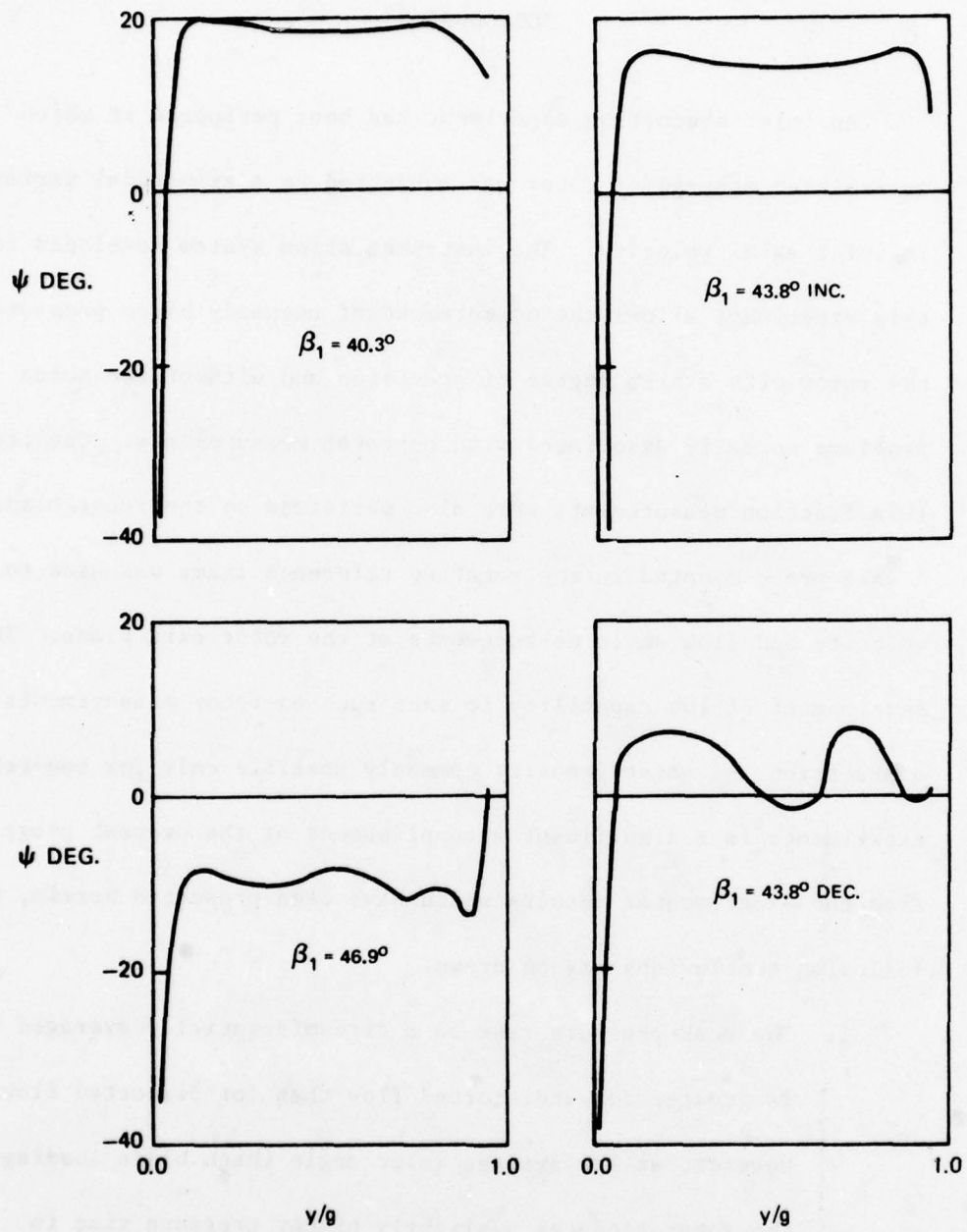


FIG. 41 RADIAL FLOW ANGLE AT ROTOR EXIT PLANE AS A FUNCTION OF GAPWISE POSITION IN DISTORTED FLOW

CONCLUSIONS

An inlet distortion experiment has been performed in which an isolated compressor rotor was subjected to a sinusoidal variation in inlet axial velocity. The instrumentation system developed for this experiment allows the measurement of unsteady blade pressures on the rotor with a high degree of precision and without the noise problems normally associated with on-rotor measurements. Qualitative skin friction measurements were also performed on the rotor blading. A wake probe mounted in the rotating reference frame was used to make velocity and flow angle measurements at the rotor exit plane. The development of the capability to make such on-rotor measurements with a precision and noise-immunity commonly possible only for non-rotating experiments is a significant accomplishment of the present program. From the experimental results which have been presented herein, the following conclusions may be drawn.

1. The peak pressure rise on a circumferentially averaged basis is greater for undistorted flow than for distorted flow. However, at low average inlet angle (high blade loading), the rotor produces a slightly higher pressure rise in distorted flow. This is attributed to the fact that the blade transiently operates beyond the steady state stall point at these average inlet angles and yet does not stall.

2. Under high blade loading, the blade pressure distribution exhibits a sharp negative peak on the suction surface near the leading edge. This peaking is more pronounced than is normally the case with an isolated airfoil.
3. As the inlet angle is increased, resulting in reduced blade loading, the pressures on the rear portion of the blade remain essentially unchanged. On the leading edge, however, the pressures undergo considerable change. At the very low blade loadings the pressures on the suction surface of the leading edge are greater than those on the pressure surface resulting in negative loading on the leading edge.
4. As the blade traverses the distortion, the greatest pressure variations occur at the most forward measuring station ($x/c = 0.034$). The response at this station consistently lags the inlet angle. The response at the second measuring station ($x/c = 0.169$) is much reduced in amplitude and leads the inlet angle at high blade loading, changing to a lagging response as the blade loading decreases. Pressures at the third and fourth measuring stations ($x/c = 0.381$ and $x/c = 0.619$, respectively) show very little variation for quasi-steady flow. However, under the influence of the unsteadiness created by the inlet distortion, a moderate response is observed. The pressures farther back on the blade essentially

follow the quasi-steady characteristic and exhibit very little change with varying inlet angle.

5. The normal force coefficient loops show a significant departure from the quasi-steady characteristic. The amplitude of the response is increased considerably and it generally leads the inlet angle. A significant penetration beyond the steady-state stall point is indicated.
6. The pitching moment coefficient loops are dominated by the pressure response at the leading edge. They show good agreement with the steady state curve at high inlet angles but depart somewhat from the steady state at low inlet angles.
7. For the lowest average inlet angle which could be attained without the occurrence of rotating stall, a separation bubble is observed to exist on the leading edge of the blade while it is in the low velocity (high loading) region. This may indicate that the inception of rotating stall is triggered by the occurrence dynamic stall in the low velocity region.
8. Velocity and flow angle measurements made at the rotor exit plane at blade midspan indicate that the flow is essentially two-dimensional in the undistorted case. The wake profiles are smooth and relatively constant except for

the regions immediately behind the blades where there is a velocity deficit and some flow angle variations. In distorted flow, however, significant radial flow is indicated. This radial velocity component changes direction (from inward to outward) as the distortion is traversed. It thus appears unreasonable to attempt to make quantitative measurements downstream of a rotor undergoing distortion without performing a radial survey of the flow parameters.

9. The circumferential exit angle variations measured in distorted flow appear to be excessive. It is possible that an interaction between the probe and the unsteady flow field behind the rotor is occurring.

The following additional statements may be made concerning the instrumentation system.

10. The use of on-board signal-conditioning and amplifying equipment produces signals which are not contaminated by slip-ring noise and reduces the number of slip-rings required for each channel of data.
11. The circuitry which was developed to perform these signal-conditioning and amplifying functions proved to be extremely reliable.
12. The triaxial hot-film probe used to measure flow angles in distorted flow was not satisfactory. The probe geometry (in

particular, the sensor placement) is believed to be at fault. In any case, a better technique for measuring these flow angles is needed.

APPENDIX I

POWER SUPPLIES

The unregulated D. C. supply for the rotating frame instrumentation was located outside the LSRR. Two 20 volt supplies capable of delivering a current of 3 amperes were connected as indicated in Fig. 42 to provide plus and minus twenty volts with

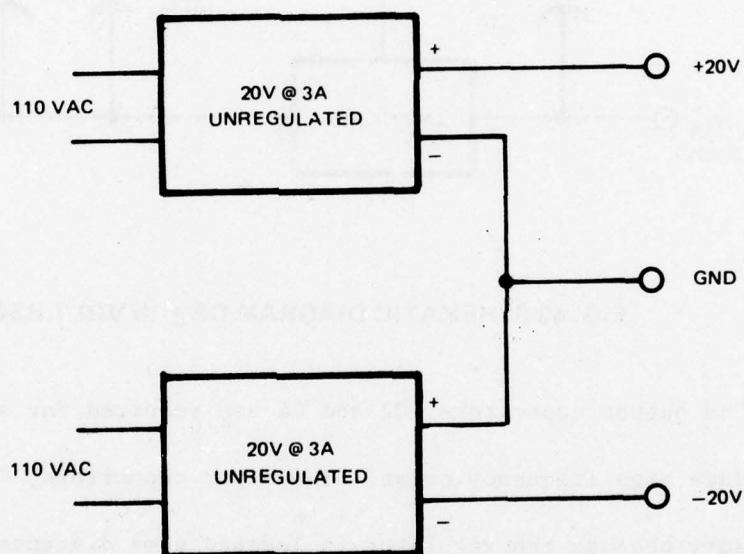


FIG. 42 UNREGULATED D.C. POWER SUPPLY

respect to a common ground. Two types of voltage regulators were used in the rotating frame instrumentation package. The first type was a dual regulator supplying ± 15 volts to the pressure transducer amplifiers and the constant temperature anemometers. Its schematic diagram is shown in Fig. 43. This circuit was taken directly from Ref. 37.

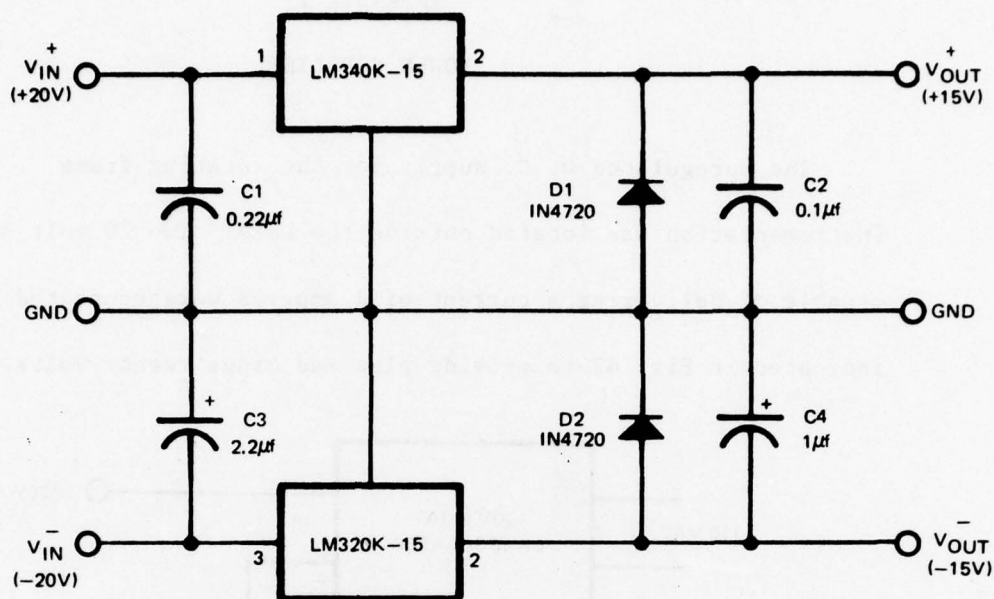


FIG. 43 SCHEMATIC DIAGRAM OF ± 15 VOLT REGULATOR

The output capacitors, C2 and C4 are required for stability and to reduce high frequency noise. The input capacitors, C1 and C3, are necessary because the regulator is located some distance from the filter capacitors in the unregulated supply. Capacitors C1 and C2 are ceramic disk types while C3 and C4 must be solid tantalum. The diodes D1 and D2 allow the regulators to start up under a common load (i.e., one between V_{out}^+ and V_{out}^-) when the unregulated supply is turned on.

The circuit for the pressure transducer excitation supply of -10 volts was also taken from Ref. 37. Its schematic diagram appears in Fig. 44.

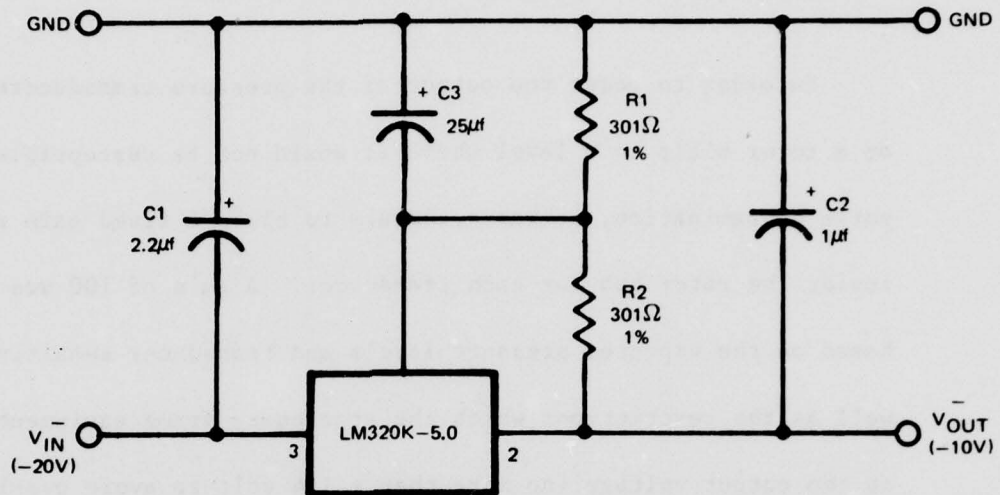


FIG. 44 SCHEMATIC DIAGRAM OF -10 VOLT REGULATOR

Capacitors $C1$ and $C2$ are solid tantalum with $C1$ being required because the regulator is remote from the unregulated supply and $C2$ being required for stability. The resistors $R1$ and $R2$ form a divider which causes the output to be twice the basic regulator output of -5 volts. The bypass capacitor $C3$ improves ripple rejection and transient response. It may be an aluminum electrolytic.

APPENDIX II

PRESSURE TRANSDUCER AMPLIFIERS

In order to boost the output of the pressure transducers mounted on a rotor blade to a level where it would not be susceptible to noise contamination, it was necessary to place a fixed gain amplifier inside the rotor hub for each transducer. A gain of 100 was chosen based on the expected pressure levels and transducer sensitivities as well as the restrictions which the stationary frame equipment placed on the output voltage (no more than ± 1.4 volt to avoid overloads). The circuit which was developed to serve this function is shown in Fig. 45. Capacitors C4 through C7 are merely filters used to minimize ripple on the operational amplifiers supply lines. Amplifiers A1 and A2 are connected as unity gain voltage followers whose sole purpose is to present a high input impedance to the transducer bridge. Amplifier A3 and resistors R1 through R6 form a differential amplifier with a gain of 100. The fixed resistors are 1 percent metal film types and the variable resistors are 22-turn cermet trimmers. These types were chosen for their stability with age and temperature. The output of the amplifier may be shifted by adjusting R6. Since each amplifier is always connected to the same transducer, this adjustment is done only once during the initial setup to account for any offset in the transducer. Trimmer R4 is adjusted to peak the D. C. common mode rejection. The offset adjustment (R6) and the D. C. common mode

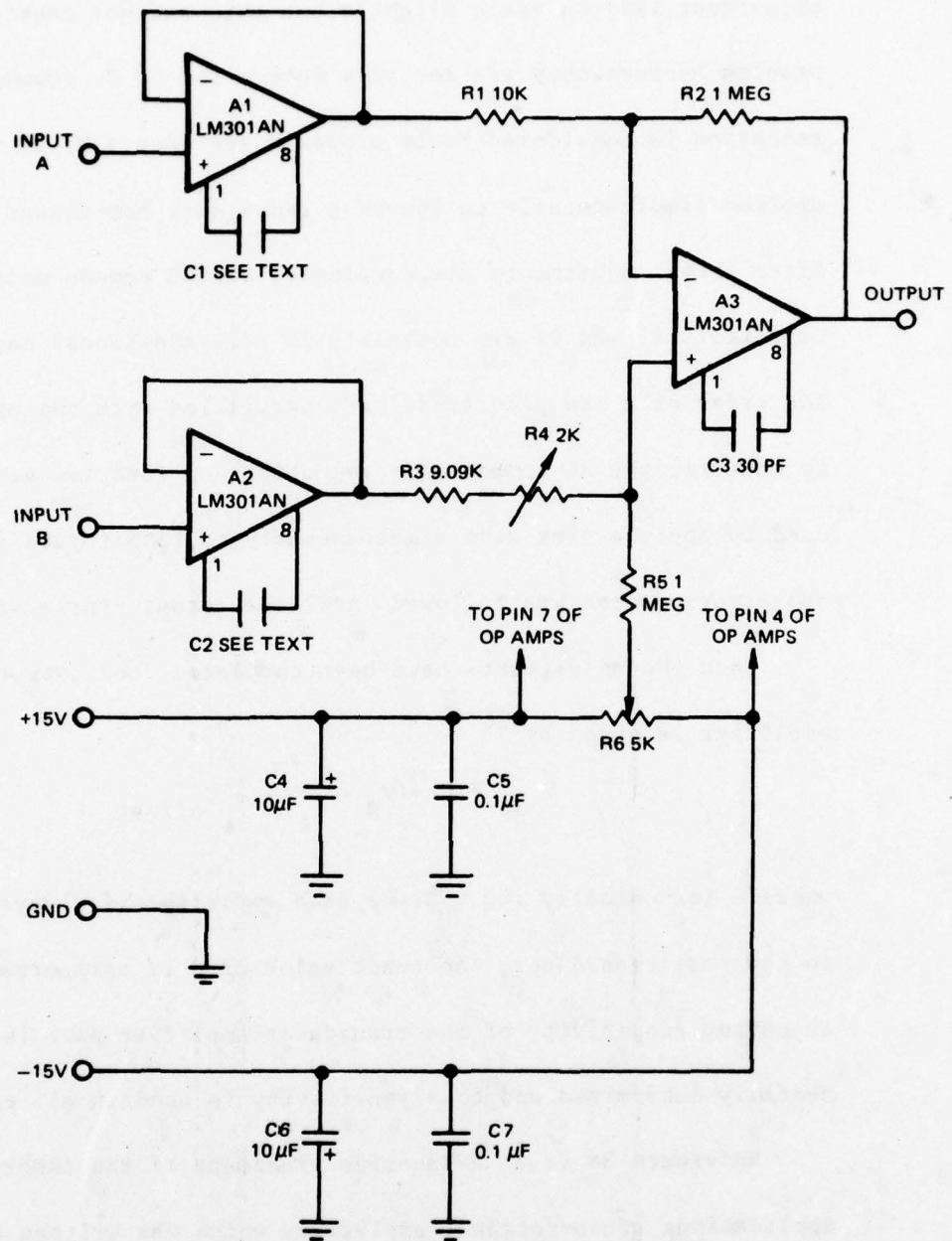


FIG. 45 SCHEMATIC DIAGRAM OF PRESSURE TRANSDUCER AMPLIFIER

adjustment (R4) interact slightly but this was not considered a problem because they are set only once. The D. C. common mode rejection is considered to be properly set when a D. C. voltage applied simultaneously to inputs A and B does not change the output. After these adjustments are completed, the AC common mode is peaked. Capacitors C1 and C2 are nominally 20 pf. Additional capacitors (on the order of a few picofarads) are paralleled with one or the other to maximize the AC common mode rejection. A function generator was used to apply a sine wave simultaneously to both inputs and a trial and error process was followed until the output ripple was minimized.

Once the adjustments have been completed, the output of the amplifier is given by

$$V_{out} = G (V_B - V_A) + V_{offset} \quad (34)$$

where G is nominally 100. Since each amplifier is always connected to the same transducer, the exact value of G is unimportant. Rather, an output sensitivity of the transducer-amplifier pair is experimentally determined and this sensitivity is used in all calculations.

Reference 38 is an exhaustive treatment of the theory and applications of operational amplifiers which was written for the layman. It is recommended reading for anyone contemplating a similar use of operational amplifiers.

APPENDIX III

CONSTANT TEMPERATURE ANEMOMETERS

The constant temperature anemometer units used in this experiment are an original design initially developed for use with the skin friction gages. After the commercial units which had been purchased to operate the triaxial hot-film probe failed under centrifugal acceleration loading, the in-house design was used for that application also. The units were designed to be inexpensive, rugged, and stable because their location inside the hub would subject them to centrifugal loads and would preclude easy adjustment once installed. These goals were easily met by the circuit of Fig. 46. First consider the bridge composed of R12 through R15. When the voltage at point A is the same as the voltage at point B the bridge is said to be balanced. The output of the error amplifier composed of A1, R6, R7, R16, and R17 will be zero. The output of A2 will be controlled by the setting of R1 which allows the circuit to have an output (at point C) with a zero error signal. If this feature were omitted, the anemometer would not start up properly when power was applied. The transistors Q1 and Q2 connected in a Darlington configuration boost the current output of A2 to meet the demands of the bridge. The Darlington pair is stabilized by resistor R11. Returning to the bridge, one finds that the condition for balance is that

- NOTES: 1. OP AMPS ARE LM301A WITH 30PF COMPENSATION CAPACITOR.
2. RESISTORS IN OHMS, 1/4 WATT 5% UNLESS NOTED.

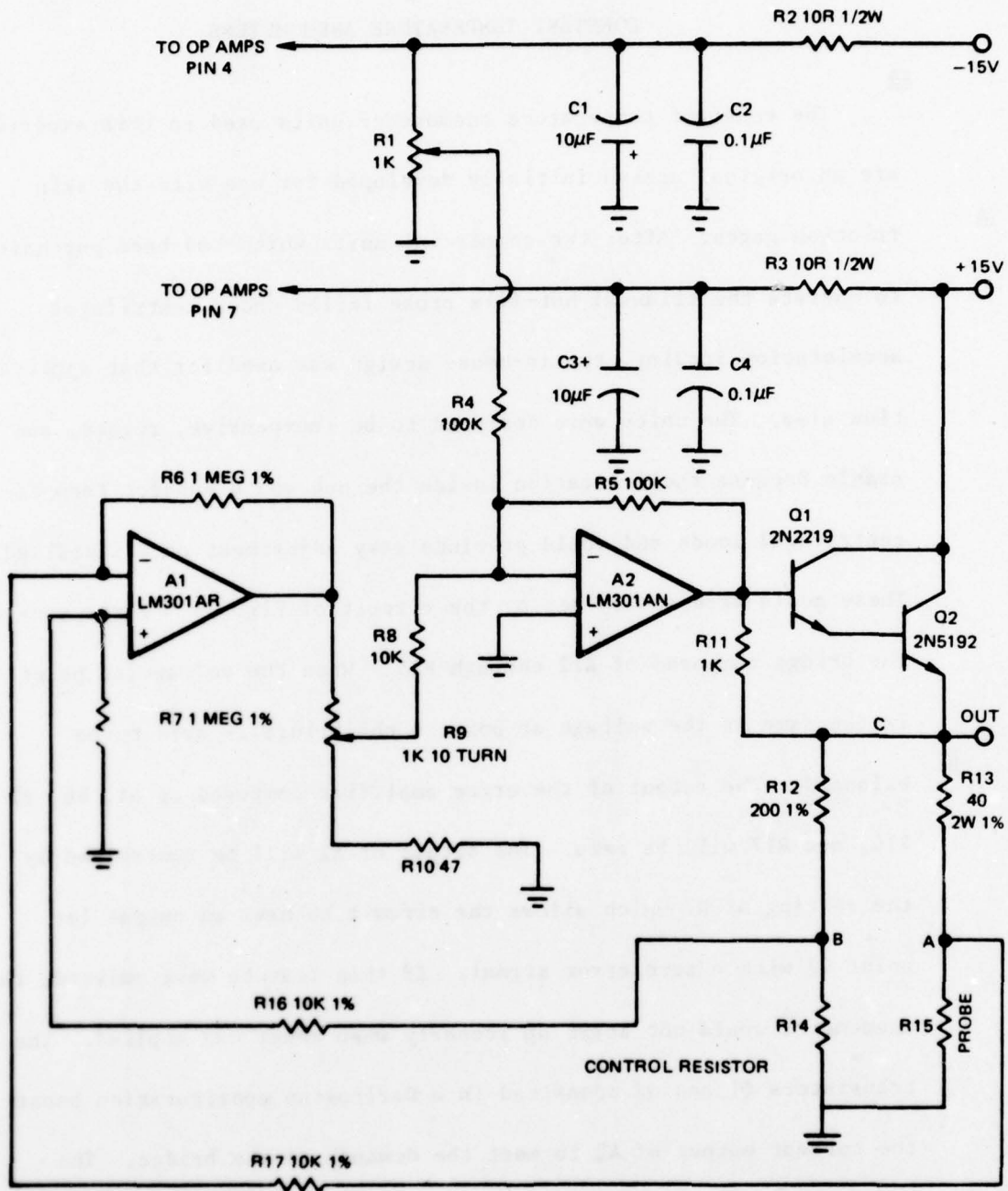


FIG. 46 SCHEMATIC DIAGRAM OF CONSTANT TEMPERATURE ANEMOMETER

$$\frac{R12}{R14} = \frac{R13}{R15} \quad (35)$$

or alternately

$$\frac{R15}{R14} = \frac{R13}{R12} = 0.2 \quad (36)$$

Thus it can be seen that the bridge is balanced when the probe resistance (R15) is one fifth that of the control resistor (R14). (This ratio is set by the chosen values of R13 and R12 and is what is commonly referred to as a 5:1 bridge.) The probe is being heated by the current through it and is operating at a resistance somewhat higher than its cold resistance. If for some reason it were to become cooler than the temperature at which the bridge balanced, its resistance would drop causing the voltage at point A to be lower than that at point B. The error amplifier would then develop a negative output which would be inverted and further amplified by A2 resulting in a higher voltage at point C. The increased current through the probe would heat it causing it to return to a balanced condition. Actually, the bridge will not always be perfectly balance; however, the imbalance will be inversely proportional to the system gain. This gain may be adjusted over a range of roughly 50 to 1000 by R8 so for all practical purposes the sensor will operate at the desired temperature. A more detailed description of the operation of constant temperature anemometers may be found in Ref. 39. A brief discussion

of some practical aspects of anemometry and an extensive bibliography of related articles may be found in Ref. 40.

APPENDIX IV

INSTRUMENTATION USED AND FLOW CONDITIONS RUN

Table V details the instrumentation available in configurations one and two. Note that the stationary frame instrumentation is the same for both configurations. Configuration one was used for runs six through eight and configuration two, for runs ten and eleven. The hot film probes behind the rotor were used to measure the number and velocity of stall cells when rotating stall was occurring. The thermocouple was intended to detect any rapid temperature variations which would not be sensed by the static data system so that the point could be repeated. Table VI is a listing of the flow conditions run in the present experimental program. The flow condition is labelled as undistorted (U) or distorted (D). Judgement as to the existence of rotating stall was based on observations of the unsteady instrumentation output on an oscilloscope.

TABLE V
INSTRUMENTATION CONFIGURATION FOR LSRR

(a) Rotating Frame Instrumentation

Channel	Conf. 1	Conf. 2
1	XD1	XD1
2	XD2	XD2
3	XD3	XD3
4	XD4	XD4
5	XD5	XD5
6	XD6	XD6
7	XD7	SF1
8	XD8	SF2
9	XD9	SF3
10	XD10	SF4
11	XD11	SF5
12	SF1	SF6
13	SF2	TX1
14	SF3	TX2
15	SF5	TX3
16	SF8	PT
17	SF11	XD12

(b) Stationary Frame Instrumentation

Channel	Data
1	HF1
2	HF2
3	HF3
4	OPR
5	TC

TABLE V (Cont'd)

INSTRUMENTATION CONFIGURATION FOR LSRR

Key:	XD	Pressure Transducer
	SF	Skin Friction Gage
	TX	Triax Probe Sensor
	PT	Total Pressure in Wake
	HF	Hot Film Probe Behind Rotor
	OPR	Once/Revolution
	TC	Thermocouple Behind Rotor

TABLE VI
 SUMMARY OF FLOW CONDITION USED IN
 LSRR INLET DISTORTION EXPERIMENT

Run	Point	β_1 (degrees)	α_{MCL} (degrees)	\bar{C}_x (ft/sec)	U (ft/sec)	W (ft/sec)	C_x/U	Flow Condition
6	6	28.5	1.5	78.5	144.7	164.6	0.543	U
6	7	33.2	-3.2	94.9	145.1	173.4	0.654	U
6	10	36.0	-6.0	105.3	144.9	179.1	0.727	U
6	11	36.6	-8.8	116.2	144.7	185.6	0.803	U
6	12	40.3	-10.3	122.8	145.0	190.0	0.847	U
6	13	43.1	-13.1	135.9	145.1	198.8	0.937	U
6	18	44.7	-14.7	143.1	144.8	203.6	0.986	U
6	21	47.9	-17.9	160.5	145.0	216.3	1.107	U
6	24	50.2	-20.2	173.8	144.8	226.2	1.200	U
7	4	28.9	1.1	78.1	141.7	161.8	0.551	D
7	6	33.5	-3.5	94.0	141.8	170.1	0.663	D
7	9	36.9	-6.9	106.6	141.8	177.4	0.752	D
7	12	40.4	-10.4	120.4	141.7	185.9	0.850	D
7	15	42.2	-12.2	128.3	141.7	191.1	0.905	D
7	16	43.7	-13.7	135.5	141.8	196.1	0.956	D
7	19	45.2	-15.2	142.5	141.7	201.0	1.006	D
7	22	28.7	1.3	77.5	141.7	161.5	0.547	D, Stalled
7	23	26.4	3.6	70.3	141.7	158.2	0.496	D, Stalled
7	24	30.7	-0.7	84.1	141.7	164.8	0.594	D, Stalled
8	3	28.8	1.2	79.3	144.0	164.4	0.551	U, Stalled ²
8	4	29.8	0.2	82.3	143.9	165.8	0.572	U, Stalled ²
8	5	30.6	-0.6	85.0	143.9	167.1	0.591	U, Stalled ²
10	3-14	43.8	-13.8	136.6	142.6	197.5	0.958	D ³
10	18-28	27.9	2.1	75.3	142.4	161.1	0.529	D, Stalled ³
11	3-16	42.3	-12.3	129.0	142.0	191.8	0.908	U ³
11	19-31	31.5	-1.5	87.1	141.9	166.5	0.614	U ³ , Stalled ³
11	34-38	32.0	-2.0	88.8	141.9	167.4	0.626	U ³

- Notes: (1) β_1 is based on \bar{C}_x for distorted flow
 (2) After completion of run it was discovered that a bearing had overheated and failed melting some of the plastic tubing running to the pneumatic blade
 (3) Wake probe traverses at a single flow condition

APPENDIX V

CALCULATION OF EXIT ANGLE USING MOMENTUM THEORY

One may derive an expression relating the exit angle to the normal force coefficient of the blades, the static pressure rise across the rotor, and the inlet angle through momentum considerations.

The control volume which will be used in the subsequent derivation is shown in Fig. 47. Note that the streamline contraction due to boundary layer growth is exaggerated. The continuity equation may be written in terms of axial velocities,

$$\rho_1 C_{x1} g b_1 = \rho_2 C_{x2} g b_2 \quad (37)$$

and for incompressible flow, $\rho_1 = \rho_2 = \rho$, and

$$C_{x1} b_1 = C_{x2} b_2 \quad (38)$$

The tangential momentum equation is

$$F_\theta = \rho g (C_{x1} C_{\theta 1} b_1 - C_{x2} C_{\theta 2} b_2) \quad (39)$$

which may be simplified using Eq. (38) to read

$$F_\theta = \rho g C_{x1} b_1 (C_{\theta 1} - C_{\theta 2}) \quad (40)$$

The axial momentum equation requires some assumption as to the variation in pressure through the rotor. If one assumes a linear variation, the axial momentum equation becomes

$$F_x = P_{s2} g b_2 - P_{s1} g b_1 + \frac{P_{s2} + P_{s1}}{2} g (b_1 - b_2) + \rho g b_2 C_{x2}^2 - \rho g b_1 C_{x1}^2 \quad (41)$$

The first term on the right side of the equality is due to pressure on the rear face of the control volume, the second is due to pressure on the front face, and the third is due to pressure on the sides. The last two terms represent the axial momentum change due to the velocity difference. Simplifying,

$$F_x = g \left(\frac{b_1 + b_2}{2} \right) (P_{S_2} - P_{S_1}) + \rho g b_1 C_{x_1} (C_{x_2} - C_{x_1}) \quad (42)$$

The axial and tangential forces may be combined to yield the normal force by using

$$F_N = F_\theta \sin \xi + F_x \cos \xi \quad (43)$$

where ξ is the chordal stagger angle. The normal force coefficient is defined as

$$C_N = \frac{F_N}{\frac{1}{2} \rho W_1^2 S} \quad (44)$$

Inserting Eqs. (40) and (42) into Eq. (43) and using the definition of C_N as given by Eq. (44) one obtains

$$C_N = \frac{4 \left(\frac{g}{c} \right) \sin^2 \beta_1 \sin \xi \cot \beta_1 - \cot \beta_2 \left(\frac{C_{x_1}}{C_{x_2}} \right)}{1 + \frac{C_{x_1}}{C_{x_2}}} + \left(\frac{g}{c} \right) C_{Pr} \cos^2 \beta_1 \cos \xi + \frac{4 \left(\frac{g}{c} \right) \sin^2 \beta_1 \left(\frac{C_{x_2}}{C_{x_1}} - 1 \right)}{\frac{C_{x_1}}{C_{x_2}} + 1} \cos \xi \quad (45)$$

This may be solved for β_2 as

$$\cot\beta_2 = \frac{C_{x2}}{C_{x1}} \cot\beta_1 - \frac{C_N \left(1 + \frac{C_{x2}}{C_{x1}}\right)}{4 \left(\frac{g}{c}\right) \sin^2\beta_1 \sin\xi} \quad (46)$$

$$+ \frac{C_{Pr} \left(1 + \frac{C_{x2}}{C_{x1}}\right)}{4 \tan^2\beta_1 \tan\xi} + \left(\frac{C_{x2}}{C_{x1}}\right) \left(\frac{C_{x2}}{C_{x1}} - 1\right) \cot\xi .$$

This equation was used to obtain the exit flow angle, β_2 , from measured values of inlet angle, normal force coefficient, and rotor pressure rise coefficient.

APPENDIX VI
TRIAxIAL PROBE CALIBRATION

The probe used in the LSRR inlet distortion experiment is a Thermo-Systems, Inc. 1296M triaxial hot-film probe. A total pressure transducer is attached to the support shaft. Two axis systems are used in calibrating the triaxial hot-film probe. One system is the axial-radial-circumferential axis system of the rotor while the other is chosen with the three axis parallel to the three mutually orthogonal velocity sensors which make up the probe. These two systems are shown in Fig. 48 omitting the total pressure probe for clarity.

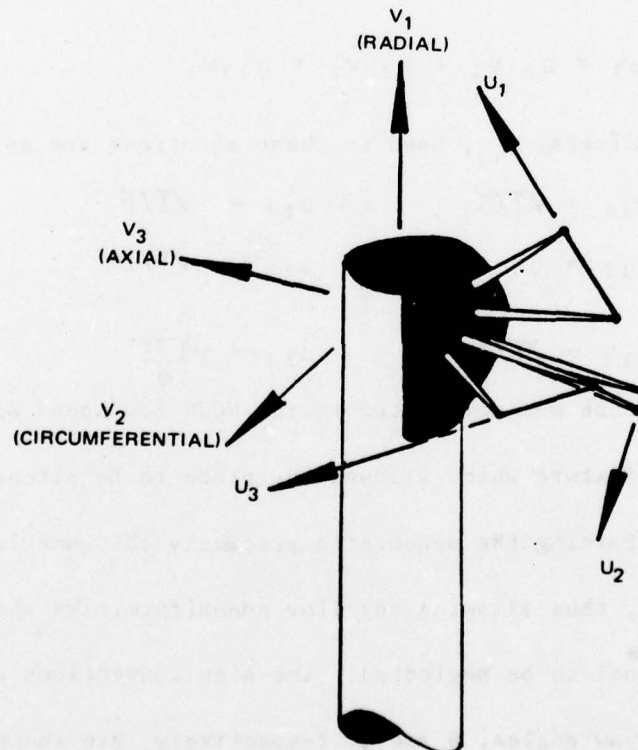


FIG. 48 AXIS SYSTEMS USED IN WAKE PROBE CALIBRATIONS

The velocity components in the two systems may be related by two systems may be related by two sets of transformation equations. The first set gives velocities in the rotor reference frame, v_i , in terms of the sensor frame velocities, u_i .

$$v_1 = a_{11}u_1 + a_{21}u_2 + a_{31}u_3 \quad (47)$$

$$v_2 = a_{12}u_1 + a_{22}u_2 + a_{32}u_3 \quad (48)$$

$$v_3 = a_{13}u_1 + a_{23}u_2 + a_{33}u_3 \quad (49)$$

The second set of equations is the reverse transformation

$$u_1 = a_{11}v_1 + a_{12}v_2 + a_{13}v_3 \quad , \quad (50)$$

$$u_2 = a_{21}v_1 + a_{22}v_2 + a_{23}v_3 \quad , \quad (51)$$

and

$$u_3 = a_{31}v_1 + a_{32}v_2 + a_{33}v_3 \quad , \quad (52)$$

The coefficients, a_{ij} , used in these equations are as follows.

$$a_{11} = \sqrt{2/3} \quad a_{21} = -\sqrt{1/6} \quad a_{31} = -\sqrt{1/6}$$

$$a_{12} = 0 \quad a_{22} = -\sqrt{1/2} \quad a_{32} = \sqrt{1/2}$$

$$a_{13} = \sqrt{1/3} \quad a_{23} = \sqrt{1/3} \quad a_{33} = \sqrt{1/3}$$

The probe was calibrated in the NCSU Low Speed Wind Tunnel using a support fixture which allowed the probe to be pitched and yawed while maintaining the sensors in precisely the same location within the tunnel, thus allowing any flow nonuniformities which might exist in the tunnel to be neglected. The sign conventions used for the pitch and yaw angles, θ and ϕ , respectively, are shown in Fig. 49.

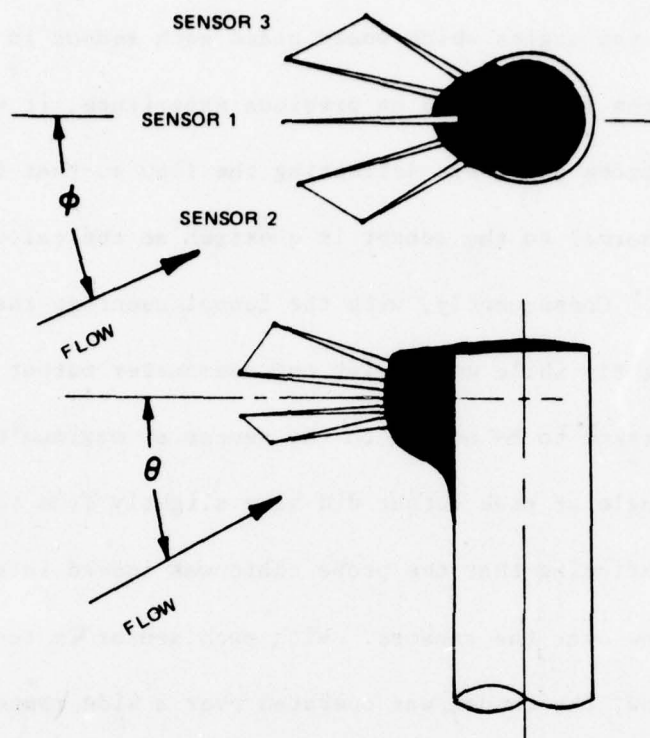


FIG. 49 SIGN CONVENTIONS FOR PITCH AND YAW ANGLES

These angles and the total velocity vector, V , may be used to calculate the velocities in the rotor reference frame.

$$v_1 = V \sin\theta \quad (53)$$

$$v_2 = V \cos\theta \sin\phi \quad (54)$$

$$v_3 = V \cos\theta \cos\phi \quad (55)$$

The direction cosines of the sensors were used to calculate pitch and yaw angles which would place each sensor in turn perpendicular to the flow. Based on previous experience, it was suspected that the probe shaft was deflecting the flow so that the flow was not actually normal to the sensor in question at the calculated pitch and yaw angle. Consequently, with the tunnel running, the probe was yawed slightly while monitoring the anemometer output voltage. The flow was taken to be normal to the sensor at maximum output voltage. The yaw angle at peak output did vary slightly from the calculated values confirming that the probe shaft was indeed interfering with the airflow over the sensors. With each sensor in turn placed normal to the flow, the tunnel was operated over a wide range of velocities and the various flow properties and the output voltage of the appropriate anemometer were recorded. It was desired to fit these data to the form of Eq. (56).

$$E^2 - E_0^2 = K\sqrt{\rho}V (T_s - T_\infty) \quad , \quad (56)$$

where E is the anemometer output voltage, ρ is the density, and T_s and T_∞ are the sensor and free stream temperature, respectively. The constants E_0 and K are determined from the calibration data. This relation between the fluid properties and the anemometer voltage was first suggested by King (Ref. 41) and bears the name King's Law. This type of relation and some of its limitations are discussed in

Refs. 40 and 42. Once such limitation is that no single set of values for E_0 and K is valid over the entire velocity range; consequently, a least squares procedure was used to obtain two curve fits of the form of Eq. (56), one of which was for the higher velocities and the other, for the lower velocities. The anemometer voltage at the intersection of these two curves was calculated. During the remainder of the calibration procedure, if the output voltage of an anemometer was higher than the crossover voltage the high velocity fit for that sensor was used, and if it was lower, the low velocity fit was used. Typical data obtained for one of the sensors and the two curve fits used are presented in Fig. 50.

After determining the response of the probe sensors to normal flow, it was necessary to investigate the behavior of the sensors in non-perpendicular flows. One expression which is commonly used to describe the response of a sensor to transverse flow is:

$$q_{\text{eff}}^2 = u_n^2 + K^2 u_t^2 \quad , \quad (57)$$

where q_{eff} is the effective velocity measured by the sensor, u_n and u_t are the normal and transverse velocity components, respectively, and K is a constant which is empirically determined. Unfortunately, this expression does not lend itself to situations where the flow may be blocked by the probe shaft and the behavior of the probe indicated that there were serious blockage effects. (See Ref. 43

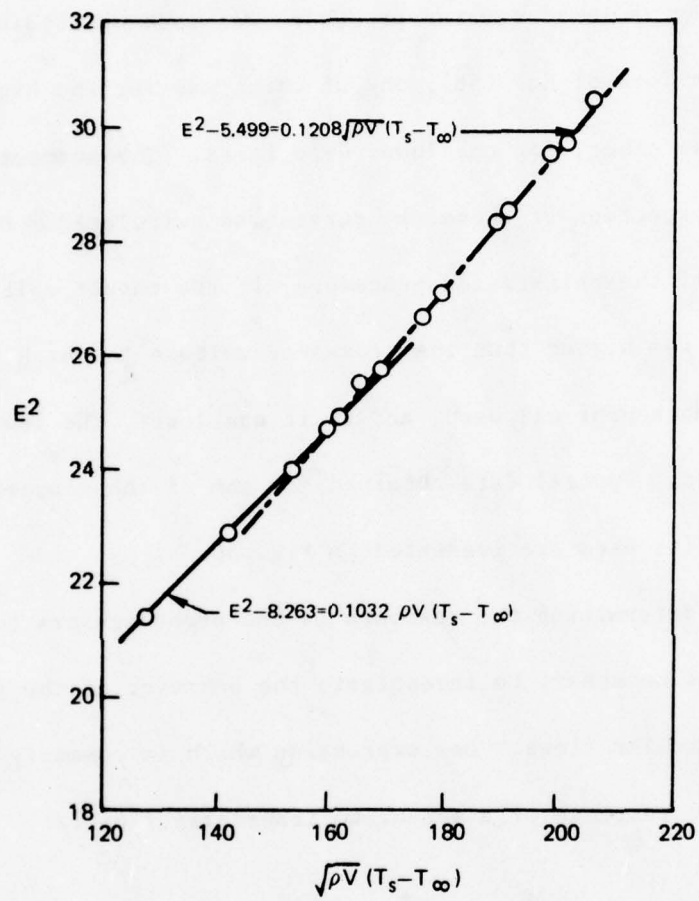


FIG. 50 TYPICAL RESULTS OF NORMAL VELOCITY CALIBRATION

for a discussion of probe shaft interference effects.) The formulation of Eq. (58) was developed to include these blockage effects as well as sensitivity to transverse flow.

$$q_{eff}^2 = u_n^2 f(\theta, \phi) \quad , \quad (58)$$

where q_{eff} and u_n are as before and $f(\theta, \phi)$ is a weighting factor of order unity which is a function of the pitch and yaw angles. The wind tunnel was operated at a constant velocity of 116 ft/sec while the probe was pitched and yawed and the data obtained used to calculate the value of this function for each sensor at each combination of pitch and yaw angles.

The values of the function at each value of θ were fitted using a least-squares method, to a fifth order polynomial in ϕ . The coefficients of each term in this polynomial were then fitted by least squares to a fifth order polynomial in θ resulting in a 5 x 5 matrix of coefficients for each sensor from which the value of the function, $f(\theta, \phi)$, at any intermediate value of θ and ϕ may be computed. The computer codes used to reduce the tabulated function to the matrix of coefficients and to subsequently reconstruct the function at arbitrary θ and ϕ are given in Appendix VIII. The function $f(\theta, \phi)$ itself was found to be velocity dependent. This was a totally unexpected development. The tunnel was therefore operated at its maximum continuous velocity (159 ft/sec) and values of $f(\theta, \phi)$ were obtained. The data were reduced to polynomial coefficients as

before. For given values of θ and ϕ a linear interpolation was applied so that

$$f(\theta, \phi) = f_L(\theta, \phi) + \frac{V - V_L}{V_H - V_L} [f_H(\theta, \phi) - f_L(\theta, \phi)] \quad (59)$$

where f_L and f_H are the values of the function as determined from the low velocity and the high velocity calibrations, respectively, and V_L and V_H are the velocities at which those calibrations were done.

The velocity V was determined from the previous iteration. Use of this procedure resulted in satisfactory performance in test cases.

In order to use the calibration data to obtain the velocity and flow angles from the three anemometer output voltages, one first must calculate an effective normal velocity for each wire by

$$q = \frac{(E^2 - E_0^2)^2}{K^2 \rho (T_s - T_\infty)^2} \quad (60)$$

where quantities on the right hand side of the equation are the same for Eq. (56). Equation (58) may be written for each sensor as follows.

$$\frac{q_1^2}{f_1} = u_2^2 + u_3^2 \quad (61)$$

$$\frac{q_2^2}{f_2} = u_1^2 + u_3^2 \quad (62)$$

$$\frac{q_3^2}{f_3} = u_1^2 + u_2^2 \quad (63)$$

In these equations, f_i is the value of the function $f(\theta, \phi)$ for the i^{th} sensor which is evaluated at the value of θ and ϕ from the previous iteration. These equations may be solved for the squared velocity components, u_i^2 . Since there is no way to know whether u_i is positive or negative from these equations, the proper sign must be known from some other source. In the present experiment, the orientation of the probe was such that the velocity components may always be assumed to be positive. Using the transformation Eqs. (47) through (49), the velocity components in the rotor reference frame, v_i , are computed. The total velocity, V , and the resultant flow angles, θ_r and ϕ_r , are calculated by Eqs. (64) through (66).

$$V = \sqrt{v_1^2 + v_2^2 + v_3^2} \quad (64)$$

$$\theta_r = \sin^{-1}(v_1/V) \quad (65)$$

$$\phi_r = \sin^{-1}(v_2/V \cos \theta) \quad (66)$$

In all cases tested, the method overcorrects. That is, if the value of ϕ used to evaluate the functions $f(\theta, \phi)$ is correct but θ is lower than the correct value, θ_r will be greater than the correct value of θ . If the value of θ is not greatly in error, ϕ_r will be essentially the same as the assumed value of ϕ . For this reason, the iterations were uncoupled and under-relaxed. Thus, with θ being held constant, ϕ is iterated upon using

$$\phi^{n+1} = 0.8\phi^n + 0.2\phi_r^n \quad (67)$$

where the superscripts denote the iteration level. When ϕ^n and ϕ_r^n have converged within the desired tolerance (normally 2.5°), the value of ϕ^{n+1} is set by Eq. (67) and θ is updated by Eq. (68).

$$\theta^{n+1} = 0.8\theta^n + 0.2\theta_r^n \quad (68)$$

When θ has also converged, the process is terminated. Note that when the iteration has been terminated, the correct value of θ is between θ^n and θ_r^n which are in error by the tolerance, ϵ . Thus choosing the computed value of θ to be the average of θ^n and θ_r^n guarantees accuracy within $\epsilon/2$. However, due to the overshoot which appears to be inherent in the method, allowing the computed value of θ to be defined by Eq. (68) gives a lower average error. (The maximum possible error for any single calculation is 0.8ϵ when using this method but the average error appears to be on the order of 0.2ϵ .) A similar argument may be made for the evaluation of ϕ .

APPENDIX VII

CORRECTION OF LEADING EDGE PRESSURES

The static pressure measuring equipment consists of a low drift pressure transducer connected to a scanivalve, a signal conditioner, and an amplifier with an internal low pass filter. The average pressures at each station as determined by this system is added to the pressures measured by the unsteady instrumentation system to reconstruct the complete pressure time histories. When the pressure coefficient difference for the leading edge was plotted (Fig. 51), it became obvious that something was wrong. The reduced frequency of the distortion is not high enough to account for so great a shift in the data. The problem was finally traced to the amplifier in the static data system. The transducer signal is first amplified by the selected gain factor and then filtered. The gain of the amplifier is linear only over a range of ± 10 volts after which it begins to clip the signal. Although the output of the filter never exceeded the clipping level, it is now known that the input to the filter did exceed this limit and was consequently distorted. Thus, the filtered output represents the average value of the clipped signal. The clipping occurred for the leading edge station on the suction surface. Since this signal has a relatively large negative value with the variations superimposed on it, the negative peaks were clipped

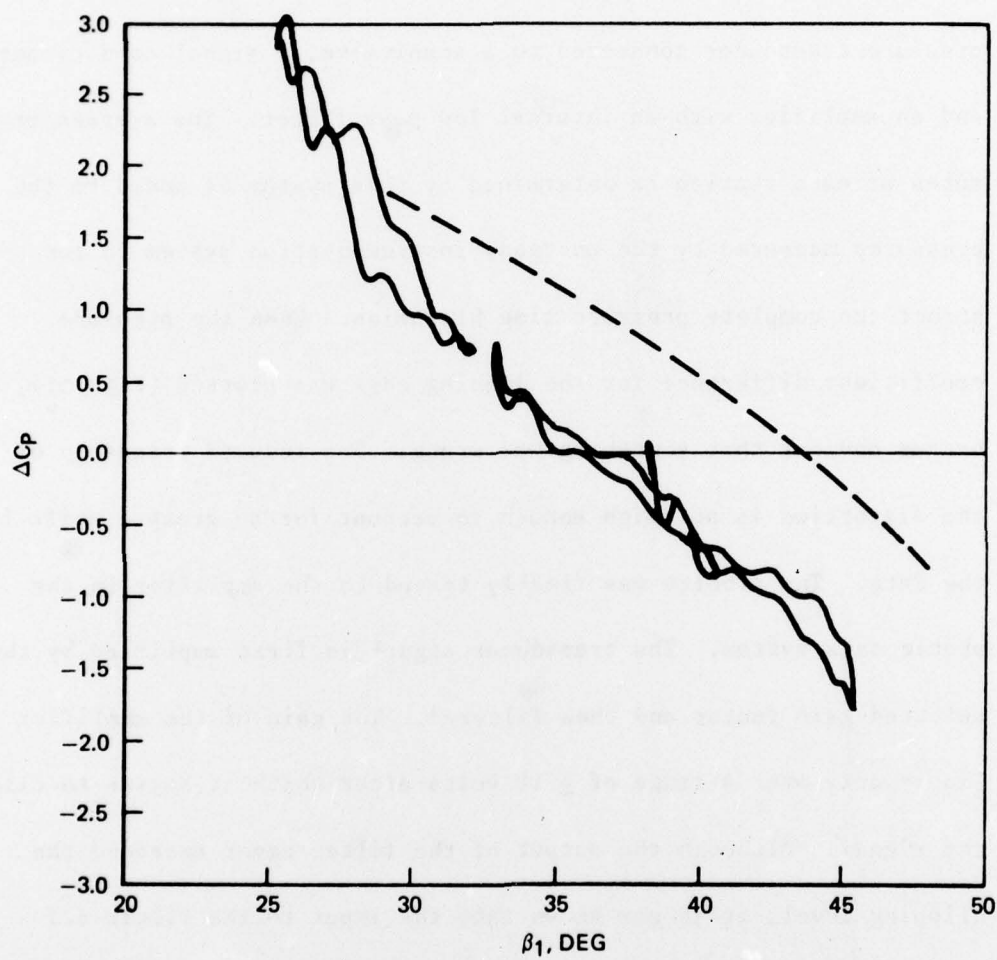


FIG. 51 PRESSURE COEFFICIENT LOOPS FROM LEADING
EDGE STATION BEFORE CORRECTION

resulting in a slightly more positive average value of the pressure being indicated than is actually the case. The result is to shift the pressure coefficient difference downward as shown in Fig. 51. No other station had an output of sufficient magnitude to experience the clipping problem.

One expects a pressure coefficient loop at such a low reduced frequency to be centered around the quasi-steady curve. The loops at the other stations confirm this assumption. Therefore, the loops at the two higher average angles are plotted with their centers on the quasi-steady line. For the loop resulting from the lowest inlet angle, a significant excursion beyond the static stall point is indicated. In this case, the portion of the loop below the static stall point is centered on the quasi-steady line. The corrected loops are shown in Fig. 24.

Now that the problem has been recognized, it is a simple matter to monitor the signal at the input of the filter to detect the onset of clipping. If this occurs, the gain may be reduced with only a slight loss in resolution. This monitoring will be necessary with tests involving higher reduced frequencies because the procedure used to correct this data may not be applicable.

APPENDIX VIII

COMPUTER CODES USED WITH TRIAXIAL HOT-FILM PROBE

The following pages are a listing of a program which converts the data in a table to a polynomial curve fit in two variables. A least-squares technique is employed to achieve a certain degree of smoothing of the data. The subroutine referred to as SIMQ is a system library routine for solving simultaneous equations of the form

$$\vec{A} \vec{x} = \vec{B}.$$

The solution vector is returned in \vec{B} and the coefficient vector \vec{A} is destroyed. Any system routine which performs the same function could be substituted. In the event that one is not available, a listing of SIMQ is included.

```

C PROGRAM FOR GENERATING LEAST SQUARES FIT TO DIRECTIONAL CALIBRATION 00000010
  DIMENSION F(3,9,9),THETA(20),PHI(20),A(3,9,5),YDUM(20),COEF(20) 00000020
  RTD=57.29578 00000030
C READ IN F(NWIRE,ITHETA,JPHI) AND THE THETA AND PHI ARRAYS 00000040
  READ(1,900)((THETA(I),PHI(J),(F(N,I,J),N=1,3),J=1,9),I=1,9) 00000050
  DO 100 I,J=1,9 00000060
  THETA(I,J)=THETA(I,J)/RTD 00000070
  PHI(I,J)=PHI(I,J)/RTD 00000080
100 C THE FOLLOWING SUBSCRIPT NOTATION WILL BE USED 00000090
C N WIRE NUMBER 00000100
C I THETA SUBSCRIPT 00000110
C J PHI SUBSCRIPT 00000120
C KI K-TH HARMONIC IN THETA 00000130
C KJ K-TH HARMONIC IN PHI 00000140
C ALL OTHERS ARE DUMMY SUBSCRIPTS 00000150
C 00000160
C FIT F AS A FUNCTION OF PHI FOR EACH WIRE (N) AND THETA (I) 00000170
  DO 300 N=1,3 00000180
  DO 300 I=1,9 00000190
C PUT F INTO A DUMMY VECTOR 00000200
  DO 200 J=1,9 00000210
200 YDUM(J)=F(N,I,J) 00000220
C COMPUTE POLYNOMIAL LEAST SQUARES FIT 00000230
  CALL POLYSQ(PHI,YDUM,COEF,9,5,KRET) 00000240
C STORE THESE COEFFICIENTS 00000250
  DO 300 K,J=1,5 00000260
300 A(N,I,KJ)=COEF(KJ) 00000270
C CURVE FIT THESE COEFFICIENTS AS FUNCTIONS OF THETA 00000280
  DO 500 N=1,3 00000290
  DO 500 KJ=1,5 00000300
  DO 400 I=1,9 00000310
400 YDUM(I)=A(N,I,KJ) 00000320
  CALL POLYSQ(THETA,YDUM,COEF,9,5,KRET) 00000330
C STORE FIT 00000340
  DO 500 KI=1,5 00000350
500 A(N,KI,KJ)=COEF(KI) 00000360
C COEFFICIENTS ARE NOW CALCULATED... WRITE INTO DATASET. 00000370
  DO 600 N=1,3 00000380
600 WRITE(4,901)((A(N,I,J),J=1,5),N,I,I=1,5) 00000390
  STOP 00000400
900 FORMAT(5F13.7) 00000410
901 FORMAT(5E14.7,2I5) 00000420
  END 00000430
  SUBROUTINE POLYSQ(X,Y,B,NPTS,NTERMS,KRET) 00000440
C POLYNOMIAL LEAST SQUARES FIT 00000450
C X INDEPENDENT VARIABLE 00000460
C Y DEPENDENT VARIABLE 00000470
C B COEFFICIENT VECTOR FOR POLYNOMIAL 00000480
C NPTS NUMBER OF POINTS TO BE FIT 00000490
C NTERMS NUMBER OF TERMS TO BE IN POLYNOMIAL 00000500
C KRET 0 INDICATES GOOD FIT...1 INDICATES FIT FAILED 00000510
  DIMENSION X(20),Y(20),B(20),A(20,20) 00000520
C CHECK FOR AN APPROPRIATE ORDER OF EQUATION 00000530
  IF(NTERMS.GE.NPTS)NTERMS=NPTS-1 00000540
C FORM MATRIX OF COEFFICIENTS 00000550
  DO 200 I=1,NTERMS 00000560
  DO 200 J=1,NTERMS 00000570
  IF(I+J.NE.2)GO TO 100 00000580
  A(I,J)=FLOAT(NPTS) 00000590
  GO TO 200 00000600
100 A(I,J)=0.0 00000610
  IEXP=I+J-2 00000620
  DO 199 K=1,NPTS 00000630
199 A(I,J)=A(I,J)+X(K)**IEXP 00000640
200 CONTINUE 00000650

```


The polynomial coefficients may be used to reconstruct the function, f , at any arbitrary value of θ and ϕ by the algorithm listed below. Since this algorithm will return a result for values of the angles far outside the range of the original data (and this result may well be in error because the polynomial fit is not a good means of extrapolation), one must be careful in applying it.

```
FUNCTION FPT (PHI, THETA, N)
COMMON/DCOF/A(3,5,5)
FPT=0.0
DO 200 I=1,5
C=A(N,5,6-I)
DO 100 J=2,5
100 C=C*THETA+A(N,6-J,6-I)
200 FPT=FPT*PHI+C
RETURN
END
```

```

SUBROUTINE SIMQ (A,B,ND,N,KS)

DIMENSION A(ND,ND),B(ND)
LOGICAL*1 BIGEXP,DIVEXP
EQUIVALENCE (DIV,DIVEXP),(BIGA,BIGEXP)
REAL DIV/Z00100000/,TOL/Z3C800000/
DO 300 I=1,N
  BIGA=0.
  DO 100 J=1,N
    100  BIGA=AMAX1(BIGA,ABS(A(I,J)))
    DIVEXP=BIGEXP
    DO 200 J=1,N
      200  A(I,J)=A(I,J)/DIV
      300  B(I)=B(I)/DIV
    KS=0
    JJ=-N
    DO 9 J=1,N
      JF1=J+1
      BIGA=0.0
      DO 2 I=J,N
        IF(ABS(BIGA)-ABS(A(I,J)))1,2,2
          1  BIGA=A(I,J)
          IMAX=I
          2  CONTINUE
          IF(ABS(BIGA)-TOL)3,3,4
          3  KS=1
          IF(BIGA.EQ.0.)RETURN
          4  DO 6 K=J,N
            IF(IMAX-J)5,6,5
            5  SAVE=A(IMAX,K)
            A(IMAX,K)=A(J,K)
            A(J,K)=SAVE
            6  A(J,K)=A(J,K)/BIGA
            SAVE=B(IMAX)
            B(IMAX)=B(J)
            B(J)=SAVE/BIGA
            IF(J-N)7,10,7
            7  DO 9 IX=JF1,N
              DO 8 JX=JF1,N
                8  A(IX,JX)=A(IX,JX)-A(IX,J)*A(J,JX)
                9  B(IX)=B(IX)-B(J)*A(IX,J)
            10  NY=N-1
            DO 11 J=1,NY
              IB=N-J
              IC=N
              DO 11 K=1,J
                11  B(IB)=B(IB)-A(IB,IC)*B(IC)
              IC=IC-1
            RETURN
          END

```

REFERENCES

1. Emmons, H. W., C. E. Pearson, and H. P. Grant: Compressor Surge and Stall Propagation. Trans. ASME, Vol. 77, April 1955, pp. 455-469.
2. Grietzer, E. M.: Surge and Rotating Stall in Axial Flow Compressors, Part I: Theoretical Compression System Model and Part II: Experimental Results and Comparison with Theory. ASME Journal Engineering for Power, Vol. 98, April 1976, pp. 190-217.
3. Carta, F. O. (editor): Unsteady Flows in Jet Engines. Proceedings of a Workshop Held at United Aircraft Research Laboratories, Project SQUID Report UARL-3-PU, (1974).
4. Mokolke, H.: Prediction Techniques. Article in Distortion Induced Engine Instability, AGARD Lecture Series No. 72, (1974).
5. Williams, D. D., and R. G. Hercock: Aerodynamic Response. Article in Distortion Induced Engine Instability, AGARD Lecture Series No. 72, (1974).
6. Mazzawy, R. S.: Multiple Segment Parallel Compressor Model for Circumferential Flow Distortion. Article in Unsteady Phenomena in Turbomachinery, AGARD-CP-177, (1976). (Also ASME Journal of Engineering for Power, April 1977, pp. 288-296.
7. Adamczyk, J. J.: Unsteady Fluid Dynamic Response of an Isolated Rotor with Distorted Inflow. AIAA Paper 74-49, (1974).
8. Colpin, J.: Propagation of Inlet Flow Distortions Through an Axial Compressor Stage. ASME Paper 78-T-34, (1978).
9. Hawthorne, W. R., N. A. Mitchell, J. E. McCune, and C. S. Tan: Nonaxisymmetric Flow Through Annular Actuator Disks: Inlet Distortion Problem. ASME Paper 78-GT-80, (1978).
10. Greitzer, E. M., and T. Strand: Asymmetric Swirling Flows in Turbomachine Annuli. ASME Paper 78-GT-109, (1978).
11. Bruce, E. P., and R. E. Henderson: Axial Flow Rotor Unsteady Response to Circumferential Inlet Distortion. Article in Unsteady Phenomena in Turbomachinery, AGARD CP-177, (1976).

REFERENCES (Cont'd)

12. Peacock, R.: Dynamic Internal Flows in Compressors with Pressure Maldistributed Inlet Conditions. Article in Unsteady Phenomena in Turbomachinery, AGARD-CP-177, (1976).
13. Mokolke, H.: The Unsteady Response of an Axial Flow Compressor with a Distorted Inlet Flow. ARC CP-1203, (1972).
14. Satyanarayana, B., J. P. Gostelow, and R. E. Henderson: A Comparison Between Experimental and Theoretical Fluctuating Lift on Cascades at Low Frequency Parameters. ASME Paper 74-GT-78. (1974).
15. Kool, P., J. DeRuyck, C. H. Hirsch: The Three-Dimensional Flow and Blade Wake in an Axial Plane Downstream of an Axial Compressor Rotor. ASME Paper 78-GT-66, (1978).
16. Colpin, J., and P. Kool: Experimental Study of an Axial Compressor Rotor Transfer Function with Non-Uniform Inlet Flow. ASME Paper 78-GT-69, (1978).
17. Day, I. J., E. M. Greitzer, and N. A. Cumpsty: Prediction of Compressor Performance in Rotating Stall. ASME Paper 77-GT-10, (1977).
18. Zinn, B. T. (editor): Experimental Diagnostics in Gas Phase Combustion Systems. AIAA Progress in Astronautics and Aeronautics, Vol. 53, New York, (1977), pp. 71-82.
19. Sexton, M. R., W. F. O'Brien, Jr., and H. L. Moses: An On-Rotor Investigation of Rotating Stall in an Axial Flow Compressor. Article in Unsteady Phenomena in Turbomachinery, AGARD CP-177, (1976).
20. Bruce, E. P.: Design and Evaluation of Screens to Provide Multi-Cycle 20% Amplitude Sinusoidal Variations in AFRF Rotor Inlet Axial Velocity Component. AIAA Paper 74-623, (1974).
21. Milne, W. E.: Numerical Calculus, Princeton University Press, 1949, pp. 285-290.
22. Davis, E. L., Jr.: The Measurement of Unsteady Pressures in Wind Tunnels. AGARD Report No. 169, (1958).

REFERENCES (Cont'd)

23. Carta, F. O., G. L. Commerford, R. G. Carlson, and R. H. Blackwell: Investigation of Airfoil Dynamic Stall and Its Influence on Helicopter Control Loads. USAAMRDL Technical Report 72-51, U.S. Army Air Mobility Research and Development Laboratory, Fort Eustis, Virginia, (1972).
24. Horlock, J. H.: Axial Flow Compressors. Butterworths, London, (1958).
25. Rhoden, H. G.: Effects of Reynolds Number on the Flow of Air Through a Cascade of Compressor Blades. ARC R&M 2919, (1956).
26. Oliver, B. M., and J. M. Cage (editors): Electronic Measurements and Instrumentation. McGraw-Hill Book Company, Inc., New York, (1971), pp. 116-118.
27. Anders, E. B., et al: Digital Filters. NASA Contractor Report, CR-136, (1964).
28. McCroskey, W. J., and E. J. Durbin: Flow Angle and Shear Stress Measurements Using Heated Films and Wires, ASME Journal of Basic Engineering, Vol. 94, (March 1972), pp. 46-51.
29. Hill, P. G., and C. R. Peterson: Mechanics and Thermodynamics of Propulsion. Addison-Wesley Publishing Company, Reading, Massachusetts, (1965).
30. Horlock, J. H., E. M. Greitzer, and R. E. Henderson: The Response of Turbomachine Blades to Low Frequency Inlet Distortions. ASME Journal of Engineering for Power, April 1977.
31. Oates, G. C. (editor): The Aerothermodynamics of Aircraft Gas Turbine Engines. Air Force Aero Propulsion Laboratory Report AFAPL-TR-78-52, (1978), Chapter 22.
32. Carta, F. O.: Effect of Unsteady Pressure Gradient Reduction on Dynamic Stall Delay. AIAA Journal of Aircraft, Vol. 8, No. 10, October 1971, pp. 839-841.
33. Carta, F. O., G. L. Commerford, R. G. Carlson, and R. H. Blackwell: Investigation of Airfoil Dynamic Stall and Its Influence on Helicopter Control Loads-USAAMRDL Technical Report 72-51, (1972).

REFERENCES (Cont'd)

34. Sears, W. R.: Some Aspects of Non-stationary Airfoil Theory and Its Practical Application. *Journal of the Aeronautical Sciences*, Vol. 8, (1941), pp. 104-108.
35. Theodorsen, T. H.: General Theory of Aerodynamic Instability and the Mechanism of Flutter. NACA Report 496 (1934).
36. Carta, F. O., and A. O. St. Hilaire: An Experimental Study on the Aerodynamic Response of a Subsonic Cascade Oscillating Near Stall. Project SQUID Technical Report UTRC-2-PU, (1976).
37. Voltage Regulator Handbook. National Semiconductor Corporation, Santa Clara, California (1975).
38. Jung, W. G.: I. C. Op-Amp Cookbook. Howard W. Sans Publications, Indianapolis, Indiana, (1974).
39. Davies, P. O. A. L., M. R. Davis, and I. Wold: Operation of the Constant Resistance Hot-Wire Anemometer-I.S.A.V. Report No. 189, University of Southampton.
40. Hot Wire-Hot Film - Ion Anemometer Systems. Thermo Systems, Inc. Catalog No. 6560375, St. Paul, Minnesota, (1975).
41. King, L. V.: On the Convection of Heat from Small Cylinders in a Stream of Fluid: Determination of the Convective Constants of Small Platinum Wires with Applications to Hot-Wire Anemometry. *Phil. Trans.* Vol. 214A, No. 14, p. 373, (1914).
42. Davies, P. O. A. L., and M. J. Fisher: Heat Transfer from Electrically Heated Cylinders. *Proc. Royal Society.* A280, pp. 486-526, (1964).
43. Comte-Bellot, G., A. Strohl, and E. Alcaras: On Aerodynamic Disturbances Caused by Single Hot-Wire Probes. ASME Paper 71-APM-T, (1971).